# University of New Mexico UNM Digital Repository

Physics & Astronomy ETDs

**Electronic Theses and Dissertations** 

9-1-2015

# Loading an Equidistant Ion Chain in a Ring Shaped Surface Trap and Anomalous Heating Studies with a High Optical Access Trap

Boyan Tabakov

Follow this and additional works at: https://digitalrepository.unm.edu/phyc etds

#### Recommended Citation

Tabakov, Boyan. "Loading an Equidistant Ion Chain in a Ring Shaped Surface Trap and Anomalous Heating Studies with a High Optical Access Trap." (2015). https://digitalrepository.unm.edu/phyc\_etds/67

This Dissertation is brought to you for free and open access by the Electronic Theses and Dissertations at UNM Digital Repository. It has been accepted for inclusion in Physics & Astronomy ETDs by an authorized administrator of UNM Digital Repository. For more information, please contact disc@unm.edu.

Boyan Tabakov		
Candidate		
Physics and Astronomy		
Department		
This dissertation is approved, and it is acceptable in quality	and form for publication:	
Approved by the Dissertation Committee:		
De Ivon Doutoch		
Dr. Ivan Deutsch	, Chairperson	
Dr. Daniel Stick		
Dr. Francisco Elohim Becerra-Chavez		
Dr. Peter Maunz		
DI. Fetel Mauliz		

### Loading an Equidistant Ion Chain in a Ring Shaped Surface Trap and Anomalous Heating Studies with a High Optical Access Trap

by

#### Boyan Tabakov

B.A., Physics and Applied Mathematics, University of California - Berkeley, 2008

M.S., Physics, The University of New Mexico, 2013

#### DISSERTATION

Submitted in Partial Fulfillment of the Requirements for the Degree of

> Doctor of Philosophy Physics

The University of New Mexico

Albuquerque, New Mexico

July, 2015

# Dedication

To my children – the inexhaustible source of my inspiration, to my spouse – my pillar of reality, and to the country that lets me live my very own American Dream.

# Acknowledgments

As is sometimes the case with first generation immigrants, I've enjoyed a life rich in events, extremes, and challenges. Yet, it is likely that getting a doctorate in experimental physics from a school producing quantum information theorists, while partaking in frontier research at a National Laboratory and raising inexhaustible children, all within five years, is going make my "top ten things to be smug and humble about" list for a while. Over the last five years, I mostly felt exactly as the previous sentence reads: elated but overloaded. Fortunately, I was surrounded by many exceptional individuals whose professional and personal help made this accomplishment possible. Because I don't think I show this often enough in person, below I'll try to extend my sincere gratitude and appreciation to as many of those individuals as I can name, for eternity.

An astute scientist, Dr. Daniel Stick, my Research Adviser at SNL, has guided me through many an experimental hurdle, sharing his experience and insight in a manner that promoted learning and exploration, instead of handing me answers. Dr. Stick's dedication to my success extended well beyond teaching me the craft of ion trapping. I have looked forward to his candid and valuable viewpoint on many occasions, sad and fun, professional and personal.

Another individual at SNL whose technical expertise has been a deep well to tap into is Dr. Peter Maunz. Considered by many to be the resident wizard, interaction with Dr. Maunz has revealed to me a new level of perfection to strive for. From math, through coding, physics, electronics, and all the way to experimental strategies, there was hardly a topic that did not get the deep and critical treatment I looked for.

Also at SNL, Dr. Matthew Blain has been an invaluable resource on surface science and microfabrication, and someone that would listen to my ideas. I've learned a fair bit of all that I know about manipulating <sup>40</sup>Ca<sup>+</sup> in the long sessions of weekend experimentation with Dr. Craig R. Clark. For five years, Raymond Haltli has shared fantastic pictures of the devices that he packaged and I studied (ahem, destroyed?). Recently, he has been generating all the awesome plasma for my experiments.

When I got to UNM's Physics and Astronomy Department five years ago, I knew that my craving for aluminum foil, dangling wires, and lasers (a.k.a. experimental work) would not leave me with enough time to properly appreciate the wealth of a program focusing on the rigors of physics theory. Yet, capitalizing on the opportunity,

I took no less than six classes containing a substantial amount of "quantum" from Dr. Ivan Deutsch and Dr. Carlton Caves, who helped me connect the dots and kept me afloat. In particular, the commitment of Dr. Deutsch, who endured my exhausted self in five classes and later became my Dissertation Adviser, has been instrumental in resolving the consequences of the intersection (life)  $\cap$  (lab)  $\cap$  (school) that I concocted as I learned that I too have limits. Likewise, I suspect that I would not have made UNM's Class of 2015 without the personal support of Dr. Caves, of Dr. David Moehring (at IARPA at the time), and of Dr. Stick. The help of my Faculty Adviser, Dr. Gregory Taylor, and of the Graduate Program Coordinator, Alisa Gibson, was invaluable when navigating the rough straits of the system. Dr. Francisco Elohim Becerra-Chavez has graciously agreed to serve on the Dissertation Committee.

At SNL, I often enjoyed Tom Hamilton's, Andrew Hollowell's, Dr. Jonathan Sterk's, and Dr. Kevin Fortier's wit (Kevin gets extra credit for the initial design of the transfer cavity lock and for the design of the helical resonator supporting block), while benefiting from their expertise. Discussions with Dr. Chris Tigges, Todd Barrick, Dr. Susan Clark, and Dr. Jonathan Mizrahi (now at JQI), have helped me gain critical insight in more than one instance. Dr. Michael Descour has been the likable kind of manager - never to be seen in the lab, but always helping in the background.

I will remember my office mate Francisco Benito as the definitive resource on where to find stuff in the lab - he kept the title despite my being around for five years. My other office mate, Akash Rakholia, I will remember with his passion for coding and as the one person at SNL that I could talk to about computer games.

My interest in ion trapping started almost eight years ago with a class in Quantum Computing given by Dr. Birgitta Whaley, while I was an undergraduate student at the University of California at Berkeley. If I had to point at a mind opening experience that lead to my career choice, it would be this class and the interaction with Dr. Whaley while battling the homework. After graduating a year later, my resolve was further solidified when I was fortunate to get hired by Dr. Hartmut Häffner to help him set up a lab at Berkeley. The hours of discussions with him, his post-docs Dr. Nikos Daniilidis and Dr. Axel Kreuter, and his (at the time) graduate students Thaned Pruttivarasin, Michael Ramm, Sönke Möller, and Sankara Narayanan, helped me understand that I really, really want to focus on microfabricated surface ion traps and learn more about all things "quantum". That is how I ended up benefiting from Sandia National Laboratories' collaboration with The University of New Mexico.

On a more personal note, I've been lucky to have Dr. Todor Karaulanov as the kind of friend that is never bored by a physics discussion on a Sunday, with babies running around and all. I cherish the friendship of Todor's and Dan's families, as

well as of Peter, Craig, Ray, Francisco, Hartmut, and Nikos.

By virtue of being themselves, my loving children have been my source of inspiration for much of what I've done in the last five years. When exhausted, I found in them the epitome of solace. For having them and raising them under the duress of having a husband that often spent too much time in the lab, their mom – my spouse, will forever be my super-heroine.

This work was supported through the Multi-Qubit Coherent Operations (MQCO) program by the Intelligence Advanced Research Projects Activity (IARPA).

Sandia National Laboratories is a multi-program laboratory managed and operated by Sandia Corporation, a wholly owned subsidiary of Lockheed Martin Corporation, for the US Department of Energy's National Nuclear Security Administration under contract DE-AC04-94AL85000.

### Loading an Equidistant Ion Chain in a Ring Shaped Surface Trap and Anomalous Heating Studies with a High Optical Access Trap

by

#### Boyan Tabakov

B.A., Physics and Applied Mathematics, University of California - Berkeley, 2008

M.S., Physics, The University of New Mexico, 2013

Ph.D., Physics, The University of New Mexico, 2015

#### Abstract

Microfabricated segmented surface ion traps are one viable avenue to scalable quantum information processing. At Sandia National Laboratories we design, fabricate, and characterize such traps. Our unique fabrication capabilities allow us to design traps that facilitate tasks beyond quantum information processing. The design and performance of a trap with a target capability of storing hundreds of equally spaced ions on a ring is described. Such a device could aid experimental studies of phenomena as diverse as Hawking radiation, quantum phase transitions, and the Aharonov - Bohm effect. The fabricated device is demonstrated to hold a  $\sim 400$  ion circular crystal, with 9  $\mu$ m average spacing between ions. The task is accomplished by first characterizing undesired electric fields in the trapping volume and then designing and applying an electric field that substantially reduces the undesired fields. In addition, experimental efforts are described to reduce the motional heating rates in a surface

trap by low energy in situ argon plasma treatment that reduces the amount of surface contaminants. The experiment explores the premise that carbonaceous compounds present on the surface contribute to the anomalous heating of secular motion modes in surface traps. This is a research area of fundamental interest to the ion trapping community, as heating adversely affects coherence and thus gate fidelity. The device used provides high optical laser access, substantially reducing scatter from the surface, and thus charging that may lead to excess micromotion. Heating rates for different axial mode frequencies are compared before and after plasma treatment. The presence of a carbon source near the plasma prevents making a conclusion on the observed absence of change in heating rates.

# Contents

Li	st of	Figur	es	xiv
Li	st of	Table	S	xix
$\mathbf{G}$	lossa	ry		xx
1	Intr	oduct	ion	1
2	Ion	Trapp	ing Theory	4
	2.1	Ion Tr	raping Devices	. 4
		2.1.1	The Hyperbolic Paul Trap	. 5
		2.1.2	The Linear rf 3D Trap	. 5
		2.1.3	Surface rf Traps	. 6
	2.2	Ion Co	ooling	. 8
		2.2.1	Cooling to the Doppler Limit	. 8
		2.2.2	Cooling to the Motional Ground State	. 9
	2.3	Detrin	nental Effects on Trapped Ions	. 10

Contents

		2.3.1	Background collisions	10
		2.3.2	Excess Micromotion	11
	2.4	Stray	Field Detection	12
		2.4.1	Radial Stray Fields	13
		2.4.2	Axial Stray Field	14
	2.5	Summ	ary	15
3	Ion	Trapp	ing With Microfabricated Paul Traps	17
	3.1	Device	es Microfabricated at Sandia National Laboratories	18
	3.2	Ultra	High Vacuum	22
	3.3	rf Volt	tage Generation and Delivery	27
	3.4	Contro	ol Electrode Voltages	33
		3.4.1	Generation	34
		3.4.2	Filtering Outside the Experimental Chamber	34
		3.4.3	Filtering and Package Support in Vacuum	35
	3.5	Ion Pr	roduction	41
		3.5.1	The Atomic Ovens	41
		3.5.2	Relevant atomic structure of ${}^{40}\mathrm{Ca}$ and ${}^{40}\mathrm{Ca}^+$	47
		3.5.3	Photoionization Light	49
	3.6	Ion Co	poling, Detection, and Imaging	51
		3.6.1	Doppler Cooling and Detection	51

xi

		3.6.2 Sideband Cooling	51
	3.7	Summary	53
4	Rin	g Trap Design	54
	4.1	Purpose	54
	4.2	Layout	55
	4.3	Field Calculation	59
	4.4	Mesh Generation	61
	4.5	Field Manipulation	65
	4.6	Model Optimization	68
	4.7	Summary and Outlook	70
5	Rin	g Trap Experiments	71
	5.1	Fabricated Devices	71
	5.2	Experimental Setup	74
	5.3	Preliminary Studies	76
	5.4	Stray Field Measurement	82
	5.5	Stray Field Correction	88
	5.6	The Equidistant Chain	91
	5.7	Summary and Outlook	95

97

6 Treating Surface Traps with Argon Plasma

xii

	6.1	Anomalous Heating	98
	6.2	Study Premise	98
	6.3	HOA2 Device Details	99
	6.4	Chamber Modifications and Setup	101
	6.5	Capacitive Plasma Discharge	104
	6.6	Inductive Plasma Discharge	107
	6.7	Heating Rates Before Treatment	109
	6.8	Heating Rates After Treatment	110
	6.9	Summary and outlook	113
7	Sun	nmary and Outlook	115
A	ppen	dices	117
A	Tra	nsfer Cavity Lock	118
В	<b>72</b> 9	nm Light Lock	121
C	Ligl	nt Collection With Diffractive Optic Elements	124
D	Exp	periment Control Software	130
	D.1	Laser Locks	132
	D.2	Control Voltages	132
	D.3	Cooling and Imaging	133

Contents			xiii
	D.4	Successor	134
	D.5	Cost Estimate	134
${f E}$	Pro	cedures and Algorithms	137
	E.1	Preparation of UHV Components	137
	E.2	Bakeout of UHV Vessels	138
	E.3	Heating Rate Measurement Procedure	141

# List of Figures

2.1	Axial field detection principle	14
3.1	Unprecedented freedom in layout design	19
3.2	Devices are scalable	20
3.3	Trench capacitor cross-section	20
3.4	Cross-section on four metal layer trapping device	21
3.5	Low profile wirebonds reduce scatter	22
3.6	Custom bottom flange	25
3.7	UHV bakeout station	26
3.8	rf delivery schematic	28
3.9	Helical resonator implementations	29
3.10	Helical resonator details, side view	29
3.11	Helical resonator details along the axis	30
3.12	Helical resonator, connected and secured	31
3 13	Helical resonator tuning	32

List of Figures	777
List of Figures	XV

3.14	Loaded resonator response	33
3.15	In vacuum filter board and ZIF socket before assembly	37
3.16	ZIF socket re-assembly after cleaning	37
3.17	Populated in-vacuum filter board	38
3.18	Soldering the connector to a populated filter board with ZIF socket.	38
3.19	In-vacuum filter board testing	39
3.20	Calcium oxidation	42
3.21	Modular atomic ovens	43
3.22	Electrode shorting due to oven firing	44
3.23	Calcium oven aligned	45
3.24	Calcium contamination of a device	45
3.25	EDS analysis of contamination	46
3.26	Evaporated calcium on a microscope slide	47
3.27	Neutral <sup>40</sup> Ca relevant structure	47
3.28	Singly ionized <sup>40</sup> Ca relevant structure	48
4.1	Ring trap layout	57
4.2	Ring trap dimensions	58
4.3	Examples of generated meshes	62
4.4	Ring trap mesh currently in use	64
4.5	The modeled pseudopotential cross-section for the ring trap	66

List of Figures	xvi

4.6	Effect of rf lead proximity on top level metal on trap parameters	69
5.1	Ring trap nomenclature.	72
5.2	SEM Images of the ring trap	73
5.3	Ring trap experiment chamber	75
5.4	Ring trap experiment chamber detail	76
5.5	Installed device with the screening mesh on the re-entrant viewport.	76
5.6	Ring trap experiment laser setup	77
5.7	Doppler beam profile for cooling the ring of ions	77
5.8	The first long chain demonstrated	78
5.9	Multiple long chains in potential pockets	79
5.10	Chain in the ring trap before correction	79
5.11	Clear evidence of loading hole potential bump	80
5.12	Locating particulate contaminants on the surface	81
5.13	Radial fields for the measurement locations	83
5.14	Secular frequencies around the ring	84
5.15	Tangential displacement extraction	85
5.16	Measured stray fields in the plane of the device	86
5.17	Tangential field change over time	87
5.18	Displacement upon scaling at intermediate locations	89
5.19	Scaling the corrective field in the ring trap	90

List of Figures	xvii
List of Figures	AVII

5.20	The ring trap filled with ions	
5.21	Tangential field for the measurement locations before and after correction	
5.22	Ion separation after applying the correction	
6.1	The HOA2 device used for most of the experiments 100	
6.2	Achieving high optical access with a microfabricated device 101	
6.3	Functional changes to the chamber	
6.4	Functional changes inside the chamber	
6.5	The imaging stack, referenced to the chamber	
6.6	The gas manifold	
6.7	Laser setup, optimized for loading at multiple locations 106	
6.8	The ring trap device used for the capacitive discharge effort 106	
6.9	Mesh screen damage during plasma generation	
6.10	Inductive discharge plasma in a test chamber	
6.11	Heating rates before Ar plasma treatment	
6.12	Localized plasma in the experimental chamber	
6.13	Heating rates after Ar plasma treatment	
6.14	Third HOA2 device with three top metals, currently in the chamber. 113	
A.1	780 nm source schematic	
B.1	Functional schematic for the 729 nm source	

List of I	7 igures	xviii
B.2	729 nm ULE cavity drift	. 123
E.1	Knife-edge damage.	. 138
E 2	Heating rate calculation.	143

# List of Tables

4.1	Mesh effects on trap parameters.	•	•	•	•	•	•	•	•	•	•	•	•	•	•	63
4.2	Ring trap geometry optimization.															68

# Glossary

degassing the process of conditioning components in vacuum after exposure to air during which trapped gas in the component is released

rf radio frequency

rf null the locus of points where the averaged electric field in a Paul trap vanishes (or the pseudopotential is a minimum)

dark time measured time for which an ion occupies the trap without cooling

trap depth—a measure of the pseudopotential depth that translates into the kinetic energy with which an ion will escape the trap

QIP quantum information processing

PI photoionization: the process of detaching an electron by irradiation

BEM boundary element method

FEM finite element method

 $\Omega$  rf drive frequency (angular)

 $\omega_r$  secular frequency (angular)

 $\lambda$  wavelength

q elementary charge

Glossary xxi

- $k_B$  Boltzmann constant
- $\hbar$  Planck constant
- T temperature
- $\epsilon_0$  electric constant

# Chapter 1

### Introduction

The field of quantum computation and simulation has been rapidly developing since the late 20-th century, in part due to the realization that a quantum-mechanical system of even a few tens of constituents is not practically calculable with classical computer technology [1, 2]. In addition, some mathematical problems of practical importance would benefit tremendously from a quantum computer. The most important of these is Shor's algorithm [3] for fast prime factorization, since the difficulty of factorizing large composite numbers with classical computers is nowadays the basis of the most widely used encryption schemes. Another applicable example of speedup with a quantum computer is Grover's unsorted database search algorithm [4]. Finally, although of little practical interest currently, there are problems that are designed to be difficult for classical computers but easy for quantum computers, such as the Deutsch–Jozsa problem [5].

One of the physical systems available for carrying out quantum computation is that of ensembles of trapped atomic ions. The idea, contributed in 1995 by Ignacio Cirac and Peter Zoller [6], along with its prompt partial experimental realization by Chris Monroe and David Wineland [7], is often considered to be the "birth" of experimental quantum computation, a field experiencing tremendous growth ever

since. The appeal of the trapped ion system is today evident in light of what became part of the DiVincenzo criteria [8] in 2000. Qubits can be encoded in parts of quadrupole (optical), Zeeman (rf), or hyperfine (microwave) energy levels in individual ions. These well defined qubits can be initialized by optical pumping techniques with fidelities exceeding 0.999 [9, 10] and high fidelity readout is routinely carried out with electron shelving techniques [11, 10]. Coherence times of systems well exceeding those needed for quantum computation have been demonstrated [12, 13, 10]. Microfabricated segmented surface ion trapping devices [14] can be used to store and manipulate large numbers of individually addressable ions forming quantum registers in complex architectures [15]. Such architectures mitigate the difficulties arising from the motional mode structure of a single large ion chain by allowing splitting, shuttling, and recombination of chains. In microfabricated devices, single qubit gates have been demonstrated with fidelity of 0.999999 [10], sequences of gates with low error have been demonstrated [16], and recently, a two qubit entangling gate has been demonstrated with a fidelity exceeding 0.97 [17].

These and further advances in the field require a formidable engineering effort. Sandia National Laboratories (SNL), with its MESA fabrication facility, has emerged as a leader in the art and science of microfabricated segmented surface ion trap development. This work details my contribution to two experiments conducted at SNL. Chapter 2 is a concise summary of the fundamentals of ion trapping and cooling from a theoretical perspective, and also contains a description of the methods behind essential tools for trap characterization. The application of ion trapping theory to microfabricated surface traps, with emphasis on elements that are common to the two experiments to be detailed later, is the focus of Chapter 3. Chapters 4 and 5 describe respectively the design and experiments with the ring trap, a device targeting the assembly of a long crystal of equidistant ions, with possible applications outside the scope of QIP. Chapter 6 details an experiment exploring the conjecture that adsorbates contribute to the electric field noise above surface electrodes – a

phenomenon with direct implications for QIP. The possibility of reducing the noise by treating the trapping device surface with low energy argon ion plasma is examined.

Throughout this work, an effort has been made to distinguish between the physical implementation (the device) and the physical phenomena (the trap) allowing constraining ions. The distinction is motivated by the ever - growing amount of features on devices that, in principle, provide the same trap. However, the term "trap" has been traditionally used to indicate both, with meaning depending on the context, as is occasionally the case in this work.

# Chapter 2

# Ion Trapping Theory

Ion trapping is a research field that has been growing for more than 60 years, and its principles have been exhaustively detailed from different viewpoints. In this chapter, central results are stated with minimal elaboration, and interpretation of historical facts is given to build a perspective. The selected topics reflect only what is relevant in the scope of the experiments detailed later. Pertinent ion trapping fundamentals are outlined in the last part of Sec. 2.1, and relevant ion cooling concepts are discussed in Sec. 2.2. Sections 2.3 and 2.4 address undesirable phenomena in ion trapping.

### 2.1 Ion Traping Devices

Even when disregarding the large body of work written on mass spectroscopy, the originally intended and main field of application for ion traps until the 1990s, the ever - increasing amount of literature on ion trapping is a testament to its potential to advance physics. Further narrowing the focus to Paul traps, with QIP in mind [18, 19, 20, 21, 22, 23, 1, 24, 25], allows the differentiation of the remainder of the section in a way emphasizing the evolution of ion trapping devices with the potential for practical QIP.

#### 2.1.1 The Hyperbolic Paul Trap

The device proposed by Wolfgang Paul in 1953 [26] and demonstrated in 1954 (originally described in the hard to access references of [27]) is sometimes referred to as the hyperbolic Paul trap. The device consists of an annulus with a hyperbolic inner cross-section, symmetric about an axis, and hyperbolic endcaps along the axis. An rf voltage is applied to the endcaps and annulus, creating an rf null in the device centroid. In addition to its historical significance, this device offers the advantage that it can be solved analytically and can thus offer insight and means of verification for newer mathematical approaches. The potential minimum generated by this type of device is a point, such that only one ion can be at the rf null. Because of Coulomb repulsion, multiple ions are pushed away from the rf null, and are thus subject to excess micromotion (Sec. 2.3.2) and the associated Doppler shifts (relevant for frequency standard applications and cooling). In the scope of QIP, where thousands of ions may be needed for a useful calculation, the practicality of a single point trapping device and its many demonstrated variants is limited.

### 2.1.2 The Linear rf 3D Trap

Although linear rf device designs [28, 29, 30, 31, 32] are considered by some to be an obvious development [33] of the hyperbolic Paul trap, they were only proposed nearly four decades later, in 1989, by Prestage [28]. The prototypical device has four electrodes, symmetric about a central axis, which is the locus of the rf null, created by applying rf voltage to a pair of non-neighboring electrodes, while the other pair is grounded. Static potentials applied to endcaps ensure that ions do not escape along the axis. Since the rf null is now a line, multiple ions can be trapped in a string. The ions in such a chain do not experience excess micromotion in an ideal device.

Variants of this device deform the rods into hyperbolic electrodes and blades, and

segment the electrodes to allow selective application of potentials along the rf null. A time-evolving potential can be used to move ions (e.g. ion chain shuttling, splitting, and recombination), and a static potential can be used to counter electric field imperfections that push the ions away from the rf null. There are also some successful implementations of junctions, allowing reordering of ion chains, in 3D structures. In addition, there are several working implementations of ring structures based on the four rod trap. Presently, linear 3D devices are still prevalent in experiments studying atomic physics, quantum mechanics, QIP, and quantum networking concepts [7, 34, 35, 9, 12, 36, 37, 38, 39, 40, 41, 42, 43, 44, 45], because of their large trap depth and low heating rates. The rigorous mathematical description of the device (that can be found in, for example, [33, 21, 22, 23, 24, 25]) is not unlike that given by Paul [26] in 1953.

In the scope of practical QIP, however, 3D devices are a dead end. One reason for this is that they are notoriously difficult to put together. With that comes a lack of repeatability, meaning that it is unlikely that any two devices of identical build will exhibit comparable performance or have comparable parameters. Finally, with the current available technology, 3D devices are hardly scalable in any of the senses discussed in Sec. 3.1, putting a limit on any application beyond a proof of concept. Segmented multi-layer traps, as the one proposed by Madsen [46] in 2004, and the first microfabricated device, demonstrated by Stick [47] in 2006 can be thought of as hybrid precursors to the next class of devices.

### 2.1.3 Surface rf Traps

The latest class of devices, microfabricated segmented surface ion trapping devices, were proposed by Chiaverini [48] in 2005 and in 2006 Siedelin [14] demonstrated them successfully. Surface devices offer a number of advantages (Sec. 3.1) over traditional bulk traps, such as freedom of design, superior optical access on the surface

side, and a full hemisphere available for ion imaging. These devices usually have segmented electrodes, as do some linear 3D traps, and often feature junctions. The fields produced by surface devices are often not analytically tractable, and despite some recent advances in that direction (described in Chapter 4), the prevalent way of assessing device parameters is numerical estimation with BEM/FEM models. A critical result that warrants parameter extraction is the concept of a pseudopotential, introduced to the ion-trapping community in 1967 by Dehmelt, but generally derived in the 1950s by a number of theorists [49]. The central idea of the result is that, in an inhomogeneous rf electric field of sufficiently high frequency, a charged particle in the vicinity of the rf null experiences a weak time-averaged net force towards the rf null. This conservative force is proportional to the gradient of the pseudopotential

$$\psi(\mathbf{x}) = \frac{q}{4m\Omega^2} E^2(\mathbf{x}),\tag{2.1}$$

where q is the particle charge, m is the particle mass,  $\Omega/2\pi$  is the rf drive frequency, and  $E^2$  is the electric field magnitude at location  $\mathbf{x}$ .

Assuming small amplitude harmonic motion about the rf null in the pseudopotential [23],

$$\psi_i = \frac{m}{2q} \omega_i^2 x_i^2 \tag{2.2}$$

and a 1/r electric field magnitude dependence

$$E \propto x^{-1},\tag{2.3}$$

the secular motion frequencies  $\omega_i$  are found[20, 46] to be

$$\omega_i = \frac{q}{m} \frac{1}{2\Omega} \sqrt{\partial_i^2 E^2(\mathbf{x})}.$$
 (2.4)

The stability parameter, defined for a hyperbolic trap as

$$q_s = \frac{\omega_i}{\Omega},\tag{2.5}$$

is a figure of merit for the stability of ion trajectories in a trap. A stable orbit is characterized by  $q_s \ll 1$ , in which case an ion starting its motion near the rf null with sufficiently low initial kinetic energy stays in the trap.

### 2.2 Ion Cooling

Once trapped, ions experience heating due to the incoherent acquisition of energy from fluctuating electric fields. Ultimately, heating leads to ion loss as the kinetic energy of the ion becomes comparable to the trap depth. To mitigate heating, ions are laser cooled [50] (an elegant modern treatment can be found in [51]). While a number of cooling schemes exist, the focus here is on the two used in this work.

In Fourier space, the spectrum for an irradiated ion with excited  $|e\rangle$  and ground  $|g\rangle$  atomic states separated by  $\omega$ , consists of the laser carrier frequency  $\omega_L \sim \omega$  and sidebands spaced by linear combinations of the secular frequencies for ion motion with a component along the radiation  $\mathbf{k}$  vector. Let the frequency of one such linear combination be  $\omega_r$ , the linewidth of the transition be  $\gamma$ , and the linewidth of the laser be  $\gamma_L$ .

#### 2.2.1 Cooling to the Doppler Limit

For a relatively broad transition, the condition  $\gamma \gg \omega_r$  means that multiple ion – light interaction events are likely to occur during a single cycle of secular motion. Assuming  $\gamma_L \ll \gamma$ , red detuned incident light is preferentially absorbed because of the Doppler shift for ion motion in the direction  $-\mathbf{k}$ , only if the ion is in  $|g\rangle$ . Upon an absorption event, the ion recoils along  $\mathbf{k}$ . Because of the short lifetime of  $|e\rangle$ , light is spontaneously emitted in a random direction, and the ion recoils in a direction opposite to the emission. In a secular motion cycle, many such events occur, and on average, the momentum gained from random emission (heating) balances the momentum lost to directed absorption (cooling). The steady state temperature in this regime is the Doppler temperature [52]

$$T_D = \frac{\hbar \gamma}{2k_B}. (2.6)$$

At  $T_D$ , the average amount of motional quanta  $n_D$  in a given motional mode can be estimated [53, 54, 51] as

$$n_D = \frac{1}{2} \frac{\gamma}{\omega_r},\tag{2.7}$$

and the size  $r_D$  of the wave packet of an ion of mass m can be estimated as

$$T_D k_B = \frac{1}{2} \hbar \gamma = m \omega_r^2 r_D^2$$

$$\Rightarrow r_D = \sqrt{\frac{\hbar \gamma}{m \omega_r^2}}.$$
(2.8)

The process described above, originally called sideband cooling [50, 55, 56], has been termed Doppler cooling over the last years, and it leaves the ion in the Lamb-Dicke regime as the ion wavepacket size is much smaller than the wavelength of the incident light [51]. The size  $r_0$  of the wave packet of an ion in the motional ground state can be estimated as

$$\frac{1}{2}\hbar\omega_r = m\omega_r^2 r_0^2$$

$$\Rightarrow r_0 = \sqrt{\frac{\hbar}{2m\omega_r}},$$
(2.9)

a factor of  $\sqrt{2\gamma/\omega_r}$  smaller than  $r_D$ .

### 2.2.2 Cooling to the Motional Ground State

An ion in the Lamb-Dicke regime can be cooled below  $T_D$  with resolved sideband cooling [57, 58, 53, 54, 51, 32, 59, 60], given that  $\omega_r \gg \gamma$  &  $\omega_r \gg \gamma_L$ . In that case, the full spectrum of sidebands is resolved. In this limit, the state of an ion can be represented as the tensor product of its two-level system state and a number state with eigenvalue corresponding to the amount of motional quanta. If the laser is tuned to the q-th red sideband so that  $\omega_L = \omega - q\omega_r$ ,  $q \in \{1, 2, 3 ...\}$ , after a  $\pi$  pulse, an ion in  $|g\rangle \otimes |n\rangle$  is excited to  $|e\rangle \otimes |n-q\rangle$ . Since the ion is in the Lamb-Dicke regime,

subsequent spontaneous emission will be predominantly at  $\omega$ , leaving the ion in  $|g\rangle \otimes |n-q\rangle$ . Repeating the excitation / emission process multiple times eventually leaves the ion close to  $|g\rangle \otimes |0\rangle$ , the motional ground state. The theoretical limit for the average number of quanta in the thermal state resulting from this scheme is [23, 51]

$$\bar{n}_{min} = (\gamma/\omega_r)^2. \tag{2.10}$$

Ion temperature in the thermal state can be inferred from the ratio  $R_q$  of the red q-th sideband to the blue q-th sideband population [59]

$$\bar{n} = \frac{R_q^{1/q}}{1 - R_q^{1/q}},\tag{2.11}$$

and maximum sensitivity is reached for  $q \sim \bar{n}$ . Experimental data relying on this approach is shown in Chapter 6 and Appendix E.3.

### 2.3 Detrimental Effects on Trapped Ions

Multiple conditions can affect stable trapping. The focus here is on two that are inherent to ion trapping and occur regardless of the atomic structure of the species being trapped.

#### 2.3.1 Background collisions

Ion traps are typically operated at low pressures (Sec. 3.2) to increase ion lifetime. While controlled numbers of collisions with a background gas are beneficial for ion lifetime when an ion cloud and a lighter buffer gas are considered [61, 62], collisions are disadvantageous in experiments relying on selectively manipulating individual ions, such as the ones in this work. A background gas atom or molecule at lab

temperature will have a kinetic energy on the order of

$$\frac{3}{2}k_B T \approx 38 \,\text{meV} \tag{2.12}$$

which is comparable to the trap depth expected from surface traps. Even if the energy an ion acquires from a collision is alone not sufficient for the ion to escape, a collision could change the phase of the ion motion and thus cause ion loss.

Another reason collisions are detrimental is that, even if they do not cause ion loss, they are likely to alter the quantum state of the trapped ion [63, 64], artificially reducing meta-stable state lifetimes, coherence times, and thus leading to loss of information. It becomes then relevant to know what is a collision rate that could be expected. Such a rate is estimated in [65] (Eq. 2.6) to be

$$\gamma = \frac{pq}{k_B T} \sqrt{\frac{\pi P}{2\epsilon_0 \mu}} \tag{2.13}$$

where p is the system pressure, P is the polarizability of the buffer gas, and  $\mu$  is the reduced mass of a gas molecule – trapped ion pair. For a buffer gas of  $H_2$  and Yb<sup>+</sup> ions at  $10^{-11}$  Torr, one collision per hour is expected. For the lighter  $^{40}$ Ca<sup>+</sup> ions used in this work, the estimate drops to one collision per two hours under the same conditions.

#### 2.3.2 Excess Micromotion

A rigorous approach to analyzing the motion of an ion experiencing an external field **E** in a linear Paul trap yields the approximate solution to its equation of motion [66] (Eq. 15 reduced to one radial dimension)

$$r(t) \approx (r_0 + r_1 \cos(\omega_r t + \phi)) \left(1 + \frac{q_s}{2} \cos(\Omega t)\right)$$
(2.14)

where  $r_1$  is the secular motion amplitude,  $\phi$  is a phase depending on the initial conditions, and  $q_s$  is the stability parameter relevant for that derivation. The unavoidable

motion at  $\Omega \pm \omega_r$  is termed micromotion, with amplitude  $q_s r_1/2$  inherent to the solution. The component of amplitude

$$q_s r_0 / 2 \approx \frac{q_s q \mathbf{E} \cdot \hat{\mathbf{r}}}{2m\omega_r^2}$$
 (2.15)

describes excess micromotion [66] at  $\Omega$  due to the external field.

While micromotion is in general reduced as secular motion is reduced by cooling, excess micromotion is unaffected by the cooling process and becomes a significant contributor to ion temperature. Excess micromotion can also be caused by a phase shift in the signal delivered to rf electrodes or by rf pickup in control electrodes. Means of detecting excess micromotion are given in the next section.

### 2.4 Stray Field Detection

Stray electric fields – fields that are not present by design – may severely hurt the performance of a device. Particulate contamination, device imperfections, and charge accumulation in dielectrics near the device can all be sources of stray fields. Any discrepancy between a trapping device and the model used to calculate needed potentials to keep an ion at the null will also manifest itself as a stray field. Unless stated otherwise, in this section, it will be assumed that such a discrepancy does not exist. Stray fields are best analyzed in the context of ideal linear traps, although the methods developed can be used with any geometry. A stray field with component normal to a linear trap axis pushes the ions off the rf null, causing excess micromotion, and thus inhibiting cooling. If the field acts in the axial direction, it modifies the axial potential, which may be important when working with ion chains or when shuttling ions.

#### 2.4.1 Radial Stray Fields

A number of techniques used in this work, all relying on excess micromotion detection, were drawn from the standard arsenal for field detection at the position of the ion in the radial directions. In all methods below, a quantitative statement about the undesired electric field magnitude and direction is made from a modeled field estimate.

Detecting changes in the ion position [66] is a technique relying on the balance between the static potential provided by control electrodes and the rf pseudopotential. Scaling the rf voltage does not change the balance at the rf null, so an ion residing at the null does not change its average position. The ion position change is inferred from ion imaging or from cooling laser position changes. Electric fields are adjusted so that rf voltage scaling does not move the ion.

Another common technique is the use of the line shape of a broad transition [66] as a gauge. When scanning (for example) the red detuned cooling transition laser frequency, excess micromotion enhances the fluorescence at the sidebands determined by the rf drive frequency, yielding bumps in the otherwise Lorentzian profile. The transition is also broadened. Electric fields are adjusted so that the bumps are eliminated and the linewidth is narrowest.

When the motional spectrum is resolvable, as is the case with a narrow transition [66], the ratio of the first sideband population and the carrier population is a minimum if there is no excess micromotion. Since the carrier population does not vary appreciably for a small undesirable field, a good approximation is the minimization of the sideband population as a function of the applied corrective fields.

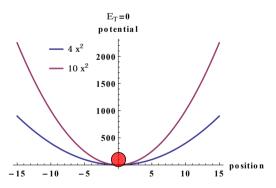
One of the most popular techniques is the fluorescence rate cross - correlation [66] with the phase of the rf drive. For an ion experiencing excess micromotion, the first order Doppler shift modulates the fluorescence rate at  $\Omega$ , as is evident from a

histogram of the number of fluorescence photons arriving at a given time during an rf cycle. Electric fields are adjusted so that the correlation is minimized.

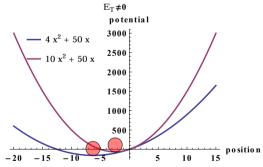
The last technique used is the detection of parametric resonance [34, 67]. In the presence of excess micromotion, secular motion amplitude is increased by parametric resonance as the rf pseudopotential is modulated. The amplitude increase manifests as a fluorescence feature (a dip for close detuned light, and a peak for far detuned light). Fields are adjusted to minimize the feature. This is also one method to determine the radial secular frequencies.

#### 2.4.2 Axial Stray Field

The technique used for axial field detection relies on imaging a single trapped ion. Assuming a stray field that lacks curvature at the ion location (relative to the extent over which the ion is expected to move), the axial component of the field is assessed by scaling the control voltages and measuring the shift of the ion position (Fig. 2.1). The axial secular frequency  $\omega_a$  of the ion is related to the axial potential  $U_a$  via [23]



(a) Scaling the harmonic potential for an ion in the absence of a stray field does not displace the ion.



(b) Scaling the harmonic potential for an ion in the presence of a stray field displaces the ion.

Figure 2.1: Axial field detection principle. In each plot, the two curves represent the axial potential for a different scaling of the control voltages that yield the harmonic axial trap.

$$\omega_a^2 = \sqrt{\frac{2kqU_a}{m}},\tag{2.16}$$

where k is a geometric factor, and so scaling  $U_a$  by a factor  $\alpha$  means that

$$\omega_a^2 \propto \alpha.$$
 (2.17)

In the presence of a constant stray field  $E_T$ , the axial potential can be also written as

$$\phi_a = \frac{m}{2a}\omega_a^2 a^2 - E_T a,\tag{2.18}$$

At equilibrium,  $\partial_a \phi_a = 0$  and the displacement a is a function of  $E_T$ , but also of  $\alpha$ 

$$E_{T} = \frac{m}{q} \omega_{a}^{2} a$$

$$\Rightarrow a = \frac{q}{m} \frac{E_{T}}{\omega_{a}^{2}}$$

$$\Rightarrow a \propto \frac{q}{m} \frac{E_{T}}{\alpha}.$$
(2.19)

Hence, although the nominal position of the ion is not known, measuring a for different values of  $\alpha$ , along with a single measurement of  $\omega_a$  for a particular  $\alpha$ , allows calculating  $E_T$ . This calculation is the basis for the results presented in Chapter 5.

# 2.5 Summary

Being a powerful tool for studies in many fields, rf ion trapping devices have evolved for over sixty years. Yet, since the devices rely on the same principles, a common mathematical description can be used to gain insight into device operation. In particular, the concept of pseudopotential allows estimating the parameters of devices that have no analytically tractable description, as is the case with many surface devices. When trapped, ions are laser cooled to prevent them from acquiring sufficient energy to escape the trap. Initially, ions are Doppler cooled, ideally to the Doppler

temperature  $T_D$ . At that time, resolved sideband cooling may be employed to cool an ion close to its motional ground state. Undesired electric fields in the trap may inhibit cooling. Such stray fields may be detected by different means and eliminated at the ion location by adjusting the trapping potential. Background collisions affect ion retention and trap operation. The collision rate is reduced by maintaining UHV.

# Chapter 3

# Ion Trapping With Microfabricated Paul Traps

There are often multiple means of overcoming a given experimental obstacle. It remains a challenge, however, to choose the solution that best fits experimental, budget, and workforce requirements or constraints. The purpose of this chapter is to lay out a set of established experimental solutions common to the experiments described in Chapter 5 and Chapter 6.

An experiment involving ion trapping, in general, starts with the design of a trapping device, perhaps with a specific task in mind, followed by the device fabrication (Sec. 3.1). Next, the device is put in an Ultra High Vacuum (UHV) vessel and UHV pressure is attained (Sec. 3.2). A trapping volume is generated by the device when rf (Sec. 3.3) and (usually) control (Sec. 3.4) voltages are applied to the respective device electrodes. Ions are produced in the trapping volume (Sec. 3.5) and the ions are Doppler cooled while being detected (Sec. 3.6). Finally, an experiment beyond trapping is attempted. The discussion of the control software developed to facilitate experiments is deferred to Appendix D.

# 3.1 Devices Microfabricated at Sandia National Laboratories

The potential of microfabrication for trapping ions was recognized and demonstrated thoroughly in the last decade [48, 14, 47, 68, 69, 70, 71, 72, 73, 20]. Microfabricated devices have become increasingly useful for QIP experiments [74, 17], particularly as the design process for surface segmented electrode ion trapping devices evolved with technology growth. Over only ten years, the objective for microfabricated traps has grown from designing a contraption that is capable of trapping ions to designing a device for a tailored purpose beyond trapping and with expectations of performance competitive with that of bulk traps. Two such tailored devices are detailed in Sec. 5.1 and Sec. 6.3. Fabrication details on SNL devices can be found in [69, 75, 76]. Here, selected desirable features that are not necessarily obvious are emphasized.

- Surface segmented electrode ion trapping devices allow shuttling, formation, and dismantling of ion chains, and may employ junctions that allow reordering the chain. Such features may be essential for implementing scalable QIP algorithms.
- Because photolitographic microfabrication is so well studied in the semiconductor industry, the fabrication techniques produce highly repeatable results.
   Devices fabricated with a given procedure perform quite similarly, making the knowledge of using a given device model transferable to multiple locations, even in different labs.
- Exquisite electric field control (Sec. 5.5) is achievable by providing suitable voltages to the control electrodes.
- Multiple metal layer devices offer unprecedented freedom in design. Because signals are routed below the surface, virtually any conceivable planar design

(e.g., one that is topologically advantageous for a task) can be implemented (Fig. 3.1).

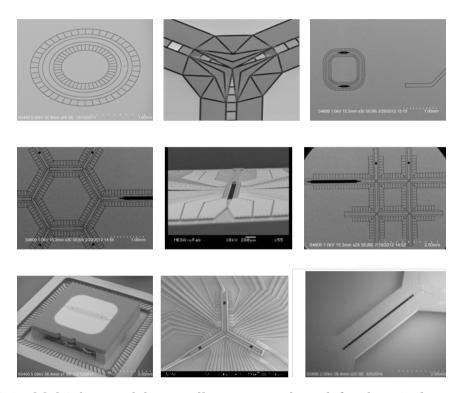


Figure 3.1: Multiple metal layers allow unprecedented freedom in layout design. Some examples of devices which have been fabricated at SNL are shown.

- Devices are scalable through modularity. When effort has been spent on understanding how, for example, a junction and a linear section work, these can be combined to yield a much more complex structure (Fig. 3.2). While knowing that the smaller blocks perform well is not a substitute for a full scale simulation of the device, the likelihood of designing a successful device is high.
- The dimensions of a well performing device can be easily scaled if miniaturization is beneficial.
- Microfabricated devices can be augmented for improved [77] or scalable [78] light collection.

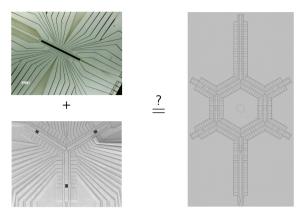
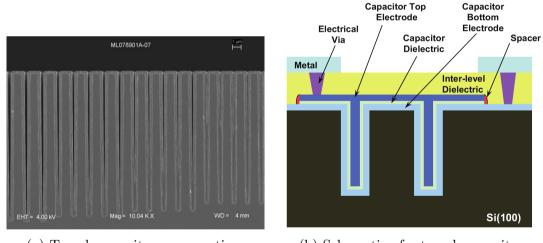


Figure 3.2: Devices are scalable through being modular. A slot and a Y-junction are parts of a much larger hexagonal design.

• Control electrode pickup filtering and shunting can be implemented on die with trench capacitors (Fig. 3.3) and meandering resistors.



(a) Trench capacitor cross-section.

(b) Schematic of a trench capacitor.

Figure 3.3: Capacitance to ground of 1 nF with 20 V breakdown voltage is standard in the current generation devices.

• Loading holes and slots allow the atomic source to never be in the surface lineof-sight (back-loading), vastly reducing device surface contamination and the probability of shorting electrodes. • The characteristic "overhang" (Fig. 3.4) feature found in many SNL devices allows different metals to be sputtered on the device surface without the possibility of electrode shorting, thus paving the way to using ions for material science studies (Sec. 6).

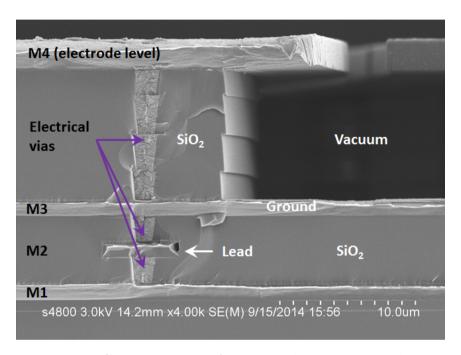


Figure 3.4: Cross-section on four metal layer trapping device.

- Low profile wirebonds (Fig. 3.5) reduce scatter for optical access in the plane of the device surface and improve optical access.
- Each device is electrically tested to ensure none of the electrodes are disconnected or shorted and thus the device is fully functional.

Given that a number of features in the list above were developed within the duration of this work, it is likely that the list of desirable features will continue to grow.

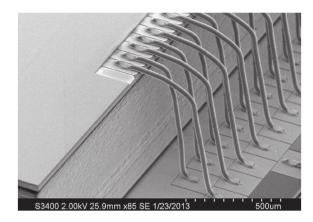


Figure 3.5: Low profile wirebonds reduce scatter.

# 3.2 Ultra High Vacuum

Attaining and maintaining Ultra High Vacuum (UHV) is one of the less forgiving aspects of ion trapping. The need for UHV is best seen from the importance of collisions of background gas with the trapped ion. Background collisions (Sec. 2.3.1) impart momentum that may lead to ion loss through different mechanisms, or destroy the coherence of the motional ionic state and thus destroy encoded information. Ion loss is further exacerbated because surface traps tend to have low trap depths (as low as 10 meV, as compared to 10 eV in 3D traps). A pressure of 10<sup>-11</sup> Torr at room temperature reduces the estimated collision rate to about one per hundred minutes, which is adequate for a number of ion manipulation tasks. To attain that pressure, materials that will be in the vacuum vessel must be carefully chosen (e.g. device, wiring, and insulation makeup). The vessel design must provide adequate optical (via viewports) and electrical (via feedthroughs) access to the device inside. Electrical filtering in vacuum (Sec. 3.4.3), as close to the device as possible, and in addition to on-chip filtering, is often desirable. This is achieved with UHV compatible components that present unique handling challenges. An atomic oven (Sec. 3.5.1) in the vacuum vessel delivers the neutral species to the trapping volume.

Once a vessel is assembled, a manifold of monitors/getters (a Bayard - Alpert

type gauge, a titanium sublimation pump, an ion pump, and sometimes, a non-evaporative getter) is added to the assembly, and a device is installed. A bakeout of the complete assembly is needed to attain UHV. Elevated temperature contributes to the kinetic energy of molecules in the vessel, making it less likely for molecules to stick to surfaces. While molecular motion is random throughout most of the bakeout, molecules that find their way to the turbomolecular pump, temporarily attached to the vessel during bakeout, are removed from the vessel. Those molecules that find a getter are retained, with very high binding energy. The net effect is "pumping out" undesired species and a reduction of the system pressure.

When aiming for UHV, following a rigid set of procedures developed by the ion trapping/particle accelerator/atomic physics communities and the semiconductor industry is a precursor to success. Attention to detail when assembling the UHV vessel is assumed, as vessel assembly and bakeouts take weeks, and contamination is often irreversible. It is desirable that a vacuum vessel that is not in active use be kept under vacuum – this facilitates outgassing (usually  $H_2$  and CO) from the bulk of the vessel walls and prevents build-up of mono-layers of atmospheric contents (e.g.  $H_2O$ ,  $N_2$ ,  $O_2$ ) on the vacuum side of the vessel walls. To reduce the probability for contamination, it is desirable that all work on the UHV side of the vessel is performed in a clean room, and the vessel is never vented outside a clean room. None of the experimental vessels in this work were assembled entirely in a clean room environment, and the consequences of that are detailed with the corresponding experiments.

The Con-Flat (CF) system is the *de-facto* standard for building UHV manifolds. CF components are typically made of 304 or 316L austenitic steel and are equipped with flanges with a sharp, polished edge (knife-edge). A seal between any two components is realized by compressing an ultra-high purity, oxygen-free copper gasket between the knife-edges of the components. All common components (elbows, nipples, reducers, etc.) are prepared for use according to the procedure outlined in

Appendix E.1. The procedure is modified as needed for sensitive (e.g. coated view-ports) and custom components.

One custom-designed vessel component used in both experiments here is the bottom 6" CF flange (Fig. 3.6). A relevant caveat in UHV design is that the design must be checked for virtual leaks – constrained pockets of matter that will outgas substantially over a long period. The flange is designed to support and register the in-vacuum filter board and ZIF socket structure (Sec. 3.4.3) via four posts, register the atomic oven (Sec. 3.5.1), and provide electrical connectivity to the device control electrodes. For the latter task, a 100 pin Micro-D connector is chosen for its high density<sup>1</sup>. The flange assembly is designed so that the trapping device is in the centroid of the experimental chamber<sup>2</sup> to within a few mm. Another custom component is the 6" re-entrant viewport designed for the short working distance of the ion imaging optics (Sec. 3.6). Nominally, the viewport should be about 1 cm away from the trapping device, however, measuring a number of viewports yielded differences of up to a few mm in depth and some tilting. While such discrepancies are perhaps due to the brazing procedure used for glass-to-metal contact and can not be avoided, it is important that explicit measurements are made for tight fits (as in the experiments here) before components are used and thus damaged.

When assembling the components, it is imperative to ensure that the gasket is clean and well seated and the flanges are parallel before applying any pressure to the gasket, as uneven gasket compression may result in a leak. Knife edges must also be inspected as any damage (Fig. E.1) or contamination (e.g. a dust particle, a copper strand), may result in a leak. Once bolts are hand-tight, any rotation of the components must be avoided as knife edges may cut strands of copper from the gasket, resulting in contamination or a leak. To avoid undesired gasket deformation, tightening all bolts consecutively in 30-45 degree increments works well, although

<sup>&</sup>lt;sup>1</sup>Flange machined and TIG welded at SRI Hermetics.

<sup>&</sup>lt;sup>2</sup>6" spherical octagon from Kimball Physics

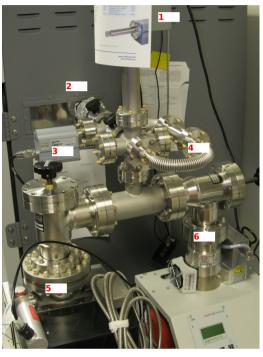


Figure 3.6: Custom 6" CF bottom flange with attached support posts, vacuum side. The 100 pin Micro-D connector is on the left, the cut-outs are for standard 1.33" flanges (for the atomic oven in the center, and a spare) on air side.

other schemes for bolt tightening exist. It is desirable to use a torque wrench to gauge bolt tightness – it is possible to tear or strip an over-torqued bolt, which in turn may not be repairable and require rebuilding of a substantial part of the manifold (e.g. tearing a bolt into a spherical octagon). To avoid micro-fusion between the clean surfaces of metal alloys of comparable composition (e.g. washers, nuts, and flanges), the most cost-effective solution that avoids using grease (because of its very high potential for contamination) is to use silver-plated stainless steel bolts. All bolts and nuts are checked for seamless threading and replaced as needed. All hardware that enters a clean room is adequately cleaned in advance. Additional details on the experimental vessels construction are given in Sec. 5.2 and Sec. 6.4.

Once an assembly is put together, it is put in a bakeout oven and attached to a pumping manifold outside the oven (Fig. 3.7). The bakeout oven is a convection





(a) Bakeout oven.

(b) Pumping manifold.

Figure 3.7: UHV bakeout station. Labels (explanation in text): 1 - RGA, 2 - oven, 3 - gauge, 4 - alternative pumping path, <math>5 - ion pump with valve, 6 - TMP with valve.

oven with about 1 m<sup>3</sup> working volume. The stock oven electronics are augmented with a programmable proportional - integral - differential (PID) controller and solid state relays, allowing for controlled ramping of temperature. The oven is equipped with two openings on opposing side walls, one for instrumentation cables and one for the bellows between the vacuum vessel and the external pumping manifold. The air circulation inside the oven ensures reasonably uniform heating of the entire vessel. To ensure good temperature control, care must be taken that the air flow around bellows and cables between the oven and environment is minimized, and the PID loop is then tuned with a suitable thermal load inside the oven. The external pumping

manifold comprises a residual gas analyzer<sup>3</sup> (RGA), a wide range vacuum gauge<sup>4</sup>, butterfly and angle valves, a turbomolecular pumping station with a diaphragm roughing pump<sup>5</sup>, and an ion pump<sup>6</sup>. The manifold provides an alternative path for initial pump-down and venting through a choke. The orifice on the choke limits the flow at high pressure so that laminar and turbulent flows are reduced, decreasing the probability of moving particle contaminants inside the chamber.

Many components in the experimental vessel assemblies have thermal gradient limits and/or thermal limits/budgets. In this work, the thermal limit of 205 °C is set by the melting point ( $\sim 217$  °C) of the solder used in crafting the in-vacuum filter board (Sec. 3.4.3). The conservative choice is warranted by the expected change in plasticity of the solder. The thermal gradient limit in this work is set by the viewports  $\sim 30$  °C/h, with a conservative choice of  $\sim 12$  °C/h. The thermal budget for each experiment is found in the relevant section. The bakeout procedure is outlined in Appendix E.2. Other relevant UHV details are given in Sec. 3.5.1, Sec. 3.4.3, Sec. 5.2, and Sec. 6.4. A comprehensive treatment of how a vacuum system functions can be found in [79]. Also, UHV equipment manufacturers' websites are becoming increasingly useful in vacuum science education by providing relevant information at a glance.

# 3.3 rf Voltage Generation and Delivery

Ion traps are typically driven by low noise sources at tens of MHz, with hundreds of volts needed at the device rf electrodes, which have a capacitive load that may be as high as a few tens of pF. Currently, there are no solid state solutions that combine all the desired properties at room temperature, particularly high Q filtering, for a

<sup>&</sup>lt;sup>3</sup>Stanford Research Systems.

<sup>&</sup>lt;sup>4</sup>MKS Instruments.

<sup>&</sup>lt;sup>5</sup>Pfeiffer Vacuum.

<sup>&</sup>lt;sup>6</sup>Varian.

direct voltage source that can be simply attached to the chamber feedthrough. The challenge is often circumvented with the following scheme (Fig. 3.8): a signal is

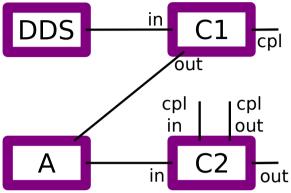


Figure 3.8: rf delivery schematic. A DDS<sup>a</sup> signal is connected through a coupler<sup>b</sup>(C1) to 1 W amplifier<sup>c</sup>(A). The amplified signal passes through a bi-directional coupler<sup>d</sup>(C2) and is delivered to the helical resonator. The purpose of C1 is to allow mixing for parametric excitation (Sec. 2.4.1). The purpose of C2 is monitoring the forward and reflected signals.

generated with a direct digital synthesis signal generator (DDS), then amplified to a few Watts with a low noise solid state amplifier, and fed into a resonator that provides voltage step-up while acting as high quality factor filter. Finally, the resonator is mounted on the chamber rf feedthrough, as close as possible to the device. Half wave resonators provide exceptional filtering, but are bulky at the desired frequencies (a 50 MHz resonator would require accommodating a 3 meter half-wave). Because of their smaller size, quarter wave helical resonators[80, 81, 82, 83, 84, 85] (Fig. 3.9) are a staple in many ion trapping labs and are also used in all experiments described here. A helical resonator is carefully designed for some desired operating parameters and then built and tested. In the design stage, attention is paid to the intended load as it will be a major factor in the resulting resonance frequency. As an example, a resonator designed to resonate at 150 MHz unloaded can in theory resonate at 49

<sup>&</sup>lt;sup>a</sup>Novatech Model 408A 100MHz DDS Signal Generator.

<sup>&</sup>lt;sup>b</sup>Mini-Circuits ZDC-20-3 Directional Coupler

<sup>&</sup>lt;sup>c</sup>Mini-Circuits ZHL-3A-S Amplifier

<sup>&</sup>lt;sup>d</sup>Mini-Circuits ZFBDC20-62HP-S+ Bi-Directional Coupler



Figure 3.9: Typical implementations of quarter wave helical resonators at SNL.

MHz and 39 MHz for 18 pF and 30 pF load, respectively.

At SNL, we build resonator shields from standard plumbing copper pipes and fittings, and resonator helical coils and antennae from solid copper wire; thus the cost of a resonator is dominated by labor expenses. In the example of a relatively recent build shown on figures 3.10 and 3.11, the shield is made of a tubular section and two



Figure 3.10: Helical resonator details, side view. The antenna (cap on the right) and endcap (on the left) slide onto the shield around the helix (middle).

caps. One cap is drilled and a BNC connector is attached, ensuring the connector ground is in good contact with the cap. A few turns of copper wire are soldered to the BNC connector. This comprises the antenna to which the amplified rf signal is fed. The details of the antenna do not seem to affect the resonator performance much, provided that the antenna does not touch the helical coil while it can slide



Figure 3.11: Helical resonator details along the axis. The helix is supported by the shield via Teflon slabs (top). A shield extension and ground wire are soldered to the endcap (bottom left). The antenna is equipped with a BNC connector (bottom right).

into the helix as the cap is moved. The helix itself is soldered inside the tubular section of the shield. The helix is made of thick copper wire without coating of prescribed thickness, wound around a tube of prescribed diameter, with a prescribed pitch and number of turns. The free end of the helix is terminated with a barrel connector, to be connected to the rf-live terminal of the chamber feedthrough. Three supports (from machined Teflon or printed thermal plastic) are used to enhance the mechanical stability of the coil. While in theory the presence of supports with high loss tangent should impede resonator performance, the experimental evidence of that is anecdotal (in one instance, a few percent increase in the resonant frequency and quality factor was observed when the supports were removed). The shield is closed with an endcap: a drilled cap, to which a shield extension and a wire with a barrel are soldered. The wire is connected to the chamber feedthrough rf-ground terminal. The shield extension is complemented with another tube section (not shown) that can

slide inside or outside the extension and is used to connect the shield to the chamber (which is at ground potential) after the feedthrough connections are made and the complete resonator is secured (Fig. 3.12). Provisions are made in case it is necessary

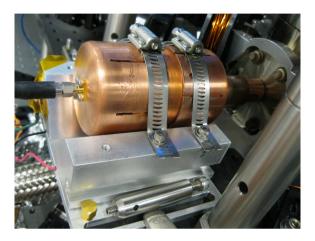


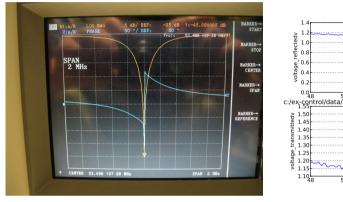
Figure 3.12: This resonator's terminals are connected to the chamber and the shield extension is slid over to provide good shielding and contact to the chamber. The whole assembly is secured to a machined V-groove, which sits on a large Peltier element with a thermistor nearby. The Peltier element is heat-sinked to a machined block secured to an optical breadboard, in turn secured to the table.

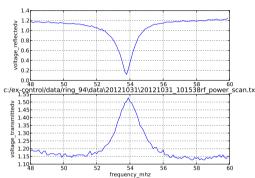
to thermally stabilize the resonator to meet performance goals. Findings are that thermal stabilization of the amplifier yields more performance stability improvement than resonator or DDS thermal stabilization.

In the ion trapping community, a lot of effort has gone into replacing "craft" with "science" when building a resonator, and yet not all failures are predictable or well understood. Commonsense rules for working with copper seem to help with the build: to make soldering easier, oxide free surfaces are desirable, and leaded solder works better (because of its lower melting point and better wetting property), in particular in view of the high thermal mass of the components to be soldered. Since heating copper increases the oxidation rate, another treatment may be needed to remove the oxide layer after soldering as some experiences suggest the oxide layer inside the shielded volume decreases resonator performance. This conjecture is not

explored in the experiments here.

A complete resonator is usually studied after attaching the load. Using a network analyzer<sup>7</sup> with a bi-directional coupler or the trap driving setup (Fig. 3.8), the resonator is tuned by sliding the antenna along the helix (using the cap), until back-reflection is minimized (Fig. 3.13). At that time, resonance frequency and





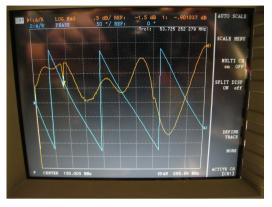
- (a) Using a network analyzer.
- (b) Using the rf driving setup.

Figure 3.13: Helical resonator tuning. Using the driving setup has the advantages that impedance matching may be improved (by changing cables and looking for frequency matching in the transmission peak and the reflection dip), and that measurements may be made at relevant input powers (so that the amplifier response is accounted for), but has the disadvantage that even a coarse frequency scan takes minutes because of instrument response latency. "Walking" the parameter space spanned by the cap position and rf drive frequency until the minimum is found and then taking a full frequency scan seems to work best.

quality factor are determined. Although the quality factor may be used to estimate the resonator step-up and thus the voltage on the trap electrodes, the estimate can be easily off and must be calibrated by comparing measured secular frequencies to the model (Chapter 5, Chapter 6), which may defeat the purpose of the estimate. Hence, the quality factor is best regarded solely as a measure of the filtering capacity of the resonator. An abrupt change in the loaded resonator response usually indicates that irreversible trap damage occurred. Yet, care should be taken when interpreting

<sup>&</sup>lt;sup>7</sup>HP E5100B

loaded resonator response (Fig. 3.14), as trap damage may be impossible to detect.





- (a) Response with well behaving device.
- (b) Response with rf-shorted device.

Figure 3.14: The resonator in (a) is attached to a device with well performing rf electrodes, and the circuit exhibits a resonance at  $\sim 54$  MHz (the first dip on the left). The resonator (newly designed for very high frequency, expected near the sharp dip in the middle) in (b) is attached to a device that turned out to have developed 1.3  $\Omega$  rf lead short to ground. When the resonator was initially unloaded, the picture was not much different (several MHz shift up), hence, the erroneous interpretation over a prolonged period was that the device had somewhat lower capacitance than estimated (as it was known not to be shorted before attaching the resonator).

# 3.4 Control Electrode Voltages

Control electrode voltages are applied to modify the trapping potential, particularly to provide confinement in the axial direction. It may be desirable to modify the potential for other reasons, for example for offsetting undesired electric fields, principal axes tilting, ion shuttling, and anharmonic trap generation. In the setup used to drive the experiments here, voltages are generated by digital to analog converters (DAC) (Sec. 3.4.1). Because achieving experimental goals may be impeded by rf pickup that will manifest itself as trapping potential modulation, a great deal of effort goes into minimizing pickup. Some researchers use five stage active and passive filtering, and others have gone as far as putting their voltage generation solution in

vacuum, under the trapping device. Here we use active and passive filtering outside vacuum (Sec. 3.4.2) and passive filtering and rf shunting in vacuum (Sec. 3.4.3).

#### 3.4.1 Generation

While several (similar) implementations of voltage generation systems were used, only the most recent is described in detail. The National Instruments-based system is a NI PXI-1045 chassis equipped with twelve NI PXI-6733 high speed analog output cards (8 channels each), a NI PXI-6281 multi-function card, a NI PXI-6653 timing module, and a NI PXI-PCI8360 remote control card. The high speed analog output cards generate the (up to) 96 control voltages used, and are capable of outputting 750 kilosamples per second when all channels are updated simultaneously. The multi-function card was used for photon counting and digital output until an FPGA based solution (Appendix D.4) took over these functions. The timing module provides the capability to synchronize all cards, although the need for that did not arise during the course of the experiments here and is, therefore, not implemented in software (Sec. D.2). The remote control module transfer the chassis control from embedded NI modules to external PCs that can be easily upgraded as computing needs increase.

## 3.4.2 Filtering Outside the Experimental Chamber

The high speed analog output cards are equipped with a standard 68 pin SCSI connector. To eliminate the need to route 12 cables, the cards are instead plugged into a distribution box that re-routes the signals into three custom cable assemblies. These assemblies carry the voltages to a custom active<sup>8</sup> filter box, intended to be in proximity to the experimental chamber, that also re-distributes signals into two 68 pin SCSI connectors. Two NI-SH68-68-EPM SCSI connector cables take the signals

<sup>8</sup>Implemented with AD8221ARZ Precision Instrumentation Amplifiers from Analog Devices.

to a filter box attached directly to the chamber 100 pin Micro-D connector. The current implementation of the box features 5-pole low pass filters with a 3.6 kHz cutoff. The filter box allows measuring the signal at the 100 pin Micro-D connector, and there is no intentional resistive path from channels to ground. A side benefit of this design that has been useful is that it allows the control voltage source to be replaced (e.g. by a battery pack) while ions are still trapped by virtue of holding the charge in the board capacitors.

#### 3.4.3 Filtering and Package Support in Vacuum

The next filtering stage is carried out in vacuum. The idea stems from the successful fabrication of printed circuit board (PCB) ion traps [86, 87] and some research identifying UHV (non-) compatible materials that was carried out at the University of California at Berkeley. Over a number of discussions with Hartmut Häffner in 2009/2010, it became clear that it would be nice to have a UHV compatible solution for filtering control electrode channels as close to the trapping device as possible. That solution would also address the issue of brittleness of ceramic pin grid arrays (CPGA) used for packaging surface trapping devices (Sec. 3.1): at the time, in vacuum sockets were often custom solutions equipped with a number of pin receptacles<sup>9</sup> that relied on a snug fit of each pin to ensure electrical contact. In aggregate, considerable force was needed for a multi-pin package to be inserted or removed. Even for a skilled operator, the change of device was a challenge, as a slight force imbalance could result in package breakage likely to ruin the device. Because of their thermal and outgassing properties, CPGAs were and are still the preferred choice for device packaging. A solution for a similar problem in the electronics industry is the Zero Insertion Force (ZIF) socket, and that idea was adopted. The final formulation of the problem was to find a UHV compatible solution involving a ZIF socket and a filter board that minimizes local outgassing. RGA cracking patterns analysis was

<sup>&</sup>lt;sup>9</sup>e.g. Precision Machined Pin Receptacles from Mill-Max

used to study the spectra of candidate materials, including at elevated temperatures and over long periods of time.

The substrate used is Rogers 4350 B. Only two side cladding was considered as the adhesives used in producing multi-layer boards were not studied. A board was designed with 94 low pass filter channels on one side, with through vias to a ground plane on the other side. Control electrode ground and rf ground are common on the PCB and not connected to the chamber (that connection is implemented via the rf resonator connection outside vacuum). In addition to its electrical shielding function, the ground plane is exposed to the trapping device, thus reducing outgassing and the amount of exposed dielectric from the substrate. All soldering was done on the bottom side of the board to minimize the amount of solder exposed to the trap. The area of the board is minimized to reduce the amount of material in vacuum while leaving room for trace routing. The board (60 mil substrate thickness, 1.5 oz/ft<sup>2</sup> copper cladding) was produced with standard etching, no silk screening and no solder mask, and finished with Electroless Nickel / Electroless Palladium / Immersion Gold (ENEPIG, final composition 3-6  $\mu$ m Ni, 76-200 nm Pd, and 25-50 nm Au). After cleaning, trace amounts of mass/charge ratio 81 and 82 were observed with an RGA, possibly HBr from the etching process, and the unpopulated board (Fig. 3.15) was deemed fit for UHV.

The custom ZIF socket<sup>10</sup> bulk plastic is polyether ether ketone (PEEK), bakeable to 250 °C, and the beryllium copper contacts are gold plated over nickel, with an operational temperature rating of 150 °C. This lower temperature limit was overlooked until recently and may explain the reduced socket performance after a number of bakeouts at 200 °C. The socket was disassembled for UHV grade cleaning and then reassembled (Fig. 3.16) before soldering.

The 94 board channels are populated (Fig. 3.17) with 0603 surface mount capac-

<sup>&</sup>lt;sup>10</sup>Designed and fabricated for SNL by Tactic Electronics, part number 100-4680-001A.

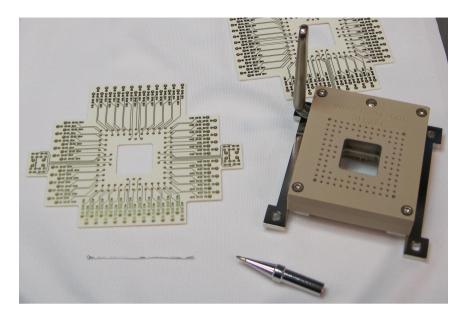


Figure 3.15: In vacuum filter board and ZIF socket before assembly. The component side of the board is shown, to face the bottom flange once populated. On the bottom of the ZIF socket, the supporting slabs for installing onto the bottom flange posts (Fig. 3.6) are shown attached.

itors<sup>11</sup> and resistors<sup>12</sup> that did not outgas when studied after UHV-grade cleaning. The solder used has composition Sn96.5Ag3.0Cu0.5 (SAC), melting at  $\sim 217$  °C, and Kester 275 no clean core. The thinnest wire with the highest amount of flux should

 $<sup>^{12}\</sup>mathrm{CRCW060333R0FKEAHP}$  from Vishay-Dale, 0.25 W, 1%



Figure 3.16: ZIF socket re-assembly after cleaning. The cam shaft, screws, pins, and PEEK body parts are processed as regular UHV parts.

 $<sup>^{11}{\</sup>rm C}1608{\rm X}8{\rm R}1{\rm H}473{\rm K}080{\rm AA}$  from TDK, X8R, 50 V, 10%

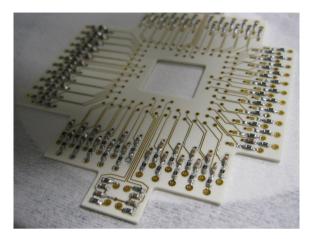


Figure 3.17: The side of the center cut-out is about 1.5 cm. The brown elements are the capacitors, and the black elements are the resistors. Common ground is implemented with through vias to the ground plane on the other side of the board.

be preferred. The ZIF socket was soldered to the ground plane side of the populated board in an open position, followed by the in-vacuum PEEK 100 pin Micro-D connector<sup>13</sup> with polyimide<sup>14</sup> insulated wires (Fig. 3.18), with due attention paid to which wire goes where. Two wires are soldered directly to the ZIF socket pins cor-

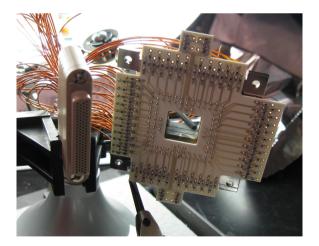


Figure 3.18: Soldering the connector to a populated filter board with ZIF socket.

responding to rf electrodes on the package. All soldering was done with virtual leak

<sup>&</sup>lt;sup>13</sup>SRIMD204-100-1 from SRI Hermetics

<sup>&</sup>lt;sup>14</sup>Kapton from DuPont

reduction in mind, although the design can be improved in that regard. All joints were made and inspected with an optical microscope, and using a dedicated clean soldering iron tip. It should be noted that trace amounts of lead in a SAC joint lead to joint brittleness and premature failure. Because of its low vapor pressure, lead is avoided in UHV.

The soldered board was cleaned again to remove any contamination accumulated during the build, and mounted on the bottom flange posts. Kapton coated wires were organized to ensure optical access is preserved. To verify proper operation, a blank package was installed in the ZIF socket (Fig. 3.19), and each filter component and

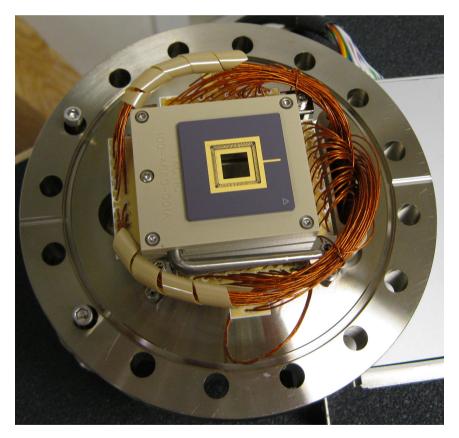


Figure 3.19: In-vacuum filter board testing. Connections were verified between pads (golden stripes near cutout) on the blank package (brown square with cutout on top of ZIF socket).

channel was tested: capacitance from each package pad to ground was measured,

and resistance from each pad to the corresponding Micro-D connector pin on the air side of the flange was measured. The cleaning/testing cycle was repeated when repairs were needed. The point of cleaning before testing is that it is unlikely that components and solder joints will experience mechanical disturbance greater than the ultrasonic bath, hence if they survive cleaning, they are likely to survive slow thermal cycling and years of use.

A relevant UHV performance issue is the degradation of the wire insulation (Kapton) over time, producing a number of easy to charge and displace small flakes that may find their way on the device. Furthermore, degraded ZIF socket performance (relatively difficult package insertion/removal) was noted after thermal cycling. The latter was attributed tentatively to the board design concept: the package is supported by the ZIF socket, in turn supported by horizontal slabs underneath, in turn supported by poles on the bottom CF flange; the board is not referenced to the assembly and is supported solely by the 100 solder joints on the ZIF socket. The speculation was that, despite the large difference between the solder melting point (217 °C) and the bakeout temperature (less then 205 °C), increased solder plasticity and stress due to the combined push of the 100 Kapton coated wires (the wires are very springy, making them relatively hard to work with) somehow tilted the pins, thus reducing performance. In view of the overlooked temperature limit (150 °C) of the ZIF socket pins, however, it is far more likely that pin elasticity was lost during thermal cycling and pins became more malleable, thus hurting socket performance.

As a final stage of filtering, most recent devices have a 1 nF capacitor (Sec. 3.1) per control electrode on die, facilitating shunting of rf pickup by the electrodes. Details for each device used are given in the corresponding section.

#### 3.5 Ion Production

In the experiments described, the scheme used for ion production is photoionization – a process in which one or more electrons from the outermost shell of a neutral atom are detached by irradiation with suitable light. Neutral calcium atoms are effused by the atomic oven (Sec. 3.5.1) under the trapping device and directed at a loading hole/slot in the device. Photoionizing light (Sec. 3.5.3) is focused above the device surface, at a location in which the expected neutral atom flux penetrates the expected trapping volume of the device – the ion loading zone. Atoms that pass through the loading zone may be stripped of an electron and thus ionized.

#### 3.5.1 The Atomic Ovens

A fair amount of downtime in the second experiment described here was due to issues related to the source of neutral atoms – the atomic oven. Alignment and thermal issues are universal to generating all neutral species, and in addition, there may be challenges because of the chemical reactivity of the species, as is the case with calcium and barium. High purity metallic calcium with natural isotope abundance ( $\sim 97\%$   $^{40}$ Ca [88]) is available as a mix of powder and pellets in inert atmosphere. Because of the large surface area and small volume of the mixture, once exposed to air, calcium reacts vigorously with water and oxidizes rapidly (Fig. 3.20). A rule of thumb is that calcium that has been exposed to atmosphere for two continuous hours has oxidized to the extent of being unusable for the purpose of making an atomic oven compatible with the goal of ion trapping. Multiple exposures to air totaling many hours seem to not impede neutral atom effusion, provided that between exposures, calcium is sufficiently heated in high vacuum to break the oxide layer.

With that in mind, a good oven should be relatively easy to make, align, test, and repair quickly. The solution used here (Fig. 3.21) utilizes pre-made components



Figure 3.20: Calcium oxidation. The can on the left hand side has been stored opened in a dry box that turned out to not provide enough oxygen displacement, hence almost all calcium inside has oxidized (CaO is off-white in appearance). The can on the right hand side is freshly opened (less than 5 minutes exposure to air), but oxidation is already seen from the color of the finest particles.

exclusively. An electrical feedthrough on a 1.33" CF flange <sup>15</sup>, capable of sustaining several amperes of current, is used as a base. The base comes with a threaded hole on the vacuum side. A thread with a venting slot is cut on one side of a 2" C-size steel rod <sup>16</sup> and the rod is screwed to the base. Clamps <sup>16</sup> (and possibly shorter rods) are used to attach a 1" C-size alumina tube <sup>16</sup> that will contain the neutral atom source. In advance, one end of the tube is closed with cement <sup>17</sup>, and is threaded into a snug filament made of W wire <sup>18</sup> (7 mil diameter wire is used). Alumina spacers and tubes <sup>16</sup> are threaded on the tube and wire for electrical and thermal insulation, as needed. Beryllium - copper, gold coated pins <sup>19</sup> are attached to the vacuum side of the base. Spot-welding <sup>20</sup> is used to connect the filament to the pins. Because of the vastly different conductivity of the Au plating and W wire and the sub-optimal (cylindrical) shape for clamping together, direct spot-welding is not preferred. Instead, a small

<sup>&</sup>lt;sup>15</sup>Accu-Glass Products.

<sup>&</sup>lt;sup>16</sup> eV Parts from Kimball Physics.

<sup>&</sup>lt;sup>17</sup>Sauereisen Electrotemp Ceramic, http://www.sisweb.com/part/SCC8.

<sup>&</sup>lt;sup>18</sup>http://www.sisweb.com/products.htm?q=W95.

<sup>&</sup>lt;sup>19</sup>Mill-Max, Digi-Key part ID ED90091-ND.

<sup>&</sup>lt;sup>20</sup>Tool of choice is Miyachi 125 ADP power supply.



(a) Atomic oven with an extra joint for precise barrel alignment. The spread-limiting tube on top is not in place yet.



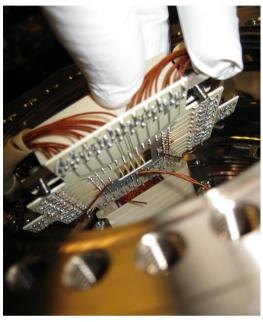
(b) Atomic oven for two species, Yb and Ca, after  $\sim 3$  years of use. Spread-limiting tubes on top are in place.

Figure 3.21: Modular atomic ovens.

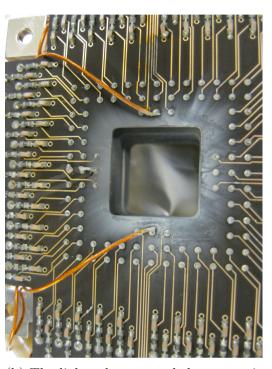
strip of 1 mil thick tantalum foil<sup>21</sup> is used as an intermediate conductor. Two to three dual, short, alternating polarity,  $\sim 8$  W·s pulses with 150 ms squeeze and 50 ms hold work well. Weld quality is verified by pulling on the filament and measuring resistance on the air side of the feedthrough. Finally, the alumina barrel(s) is(are) filled with the desired species and a spread-limiting B-size alumina tube<sup>16</sup> is cemented on top. All work is done with UHV cleanliness in mind. The oven assembly is either cured in a dry box or installed in a vacuum vessel for immediate evacuation.

Once the oven assembly is installed in a vessel, it may be desirable to adjust the <sup>21</sup>ESPI Metals Knc1744.

alignment of the barrel(s), check that there is sufficient atomic flux, and verify that this flux is not likely to short nearby conductors (Fig. 3.22). One way to do that is



(a) The metallic film (gray in appearance) around the bottom and left sides of the cutout shorts board channels, effectively shorting trap electrodes. The film in this image is tantalum. The inadvertent source was  $\sim 2$  cm below the board.



(b) The lighter hue around the cutout is CaO in air. In vacuum that was calcium with the potential to short board channels. The board color is due to viewport failure causing air exposure during a bakeout. The oven top was a few mm below the board.

Figure 3.22: Electrode shorting due to oven firing. Shown are the bottoms of a in-vacuum filter boards (Sec. 3.4.3).

to put a glass slide in place of the trapping device (Fig. 3.23) and fire the oven. As current is passed through the tungsten filament, Ohmic heating from the filament is transferred to the alumina tube and then to the metal pellets inside. The initial heating of the oven after exposure to air (degassing) must happen slowly enough to allow slow thermal expansion of whatever is in the barrel, otherwise bulk matter is ejected and the devices are contaminated, damaging them or even rendering them



Figure 3.23: Calcium oven aligned. A microscope glass slide is covering the cut-out of the ZIF socket. The oven barrel (the same construction shown in Fig. 3.21a but equipped with spread-limiting tube), viewed form the top, is positioned as desired. Once sublimated, Ca deposits on the slide and a thin metallic film can be seen at a facilitating angle. The spot was not captured with the camera despite some effort.

inoperable (Fig. 3.24, Fig. 3.25).

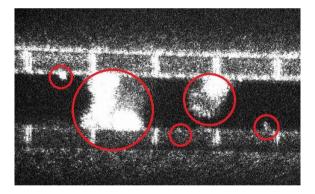


Figure 3.24: Calcium contamination of a device. One of two devices destroyed by a current surge due to a flaky connection in the oven current supply cable. Photoionization light is scattered off the surface while the device is imaged. The distance between the vertical lines (gaps between electrodes) is about 70  $\mu$ m. The particles appear larger than their actual size due to excessive scatter and being out of focus.

During degassing, a conservative approach was lately adopted that likely prolongs the life of the oven filament and ensures robust testing. Current is increased, in a manner that keeps the system pressure below  $10^{-5}$  Torr, until metallic calcium film

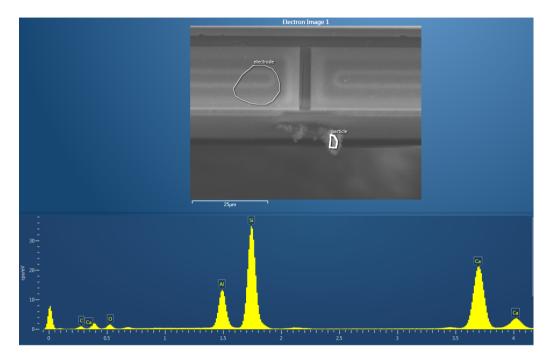


Figure 3.25: Energy Dispersive Spectroscopy (EDS) analysis shows the composition of the chunk shown on the SEM image.

is seen on the glass slide. The process takes a few hours. If sufficient amount of calcium was deposited on the glass slide, it may be possible to see traces of compounds after the chamber is vented(Fig. 3.26). It may be necessary to iterate venting/pumpdown/degassing until alignment is satisfactory, and it should be noted that the device die is an additional  $\sim 4$  mm above the glass slide. Once aligned, an oven may be removed for storage or a device installed. Depending on the spot size and location, oven removal may invalidate the alignment as the 1.33" CF flanges can only be registered within a few hundred  $\mu$ m. Once a device is installed and the oven degassed, the oven current does not need to be ramped up and the pressure increase due to oven firing is not detrimental to experimentation. Sufficient neutral atom flux is generated at about 10 W of power delivered to the filament. Less common means of delivering atomic calcium (laser ablation, pre-made sources covered with indium, and multiple stage sublimation) exist.

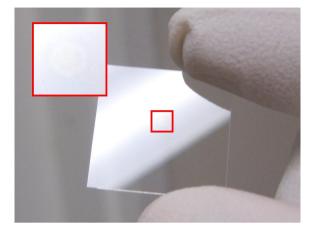


Figure 3.26: Evaporated calcium on a microscope slide. Calcium readily reacts with water, oxygen and nitrogen from the atmosphere, making it challenging to observe the thin film deposited when an oven is fired. The inset shows the calcium spot magnified.

# 3.5.2 Relevant atomic structure of <sup>40</sup>Ca and <sup>40</sup>Ca<sup>+</sup>

Calcium is an alkaline earth metal with [Ar] $4 s^2$  electron structure. One way to singly ionize  $^{40}$ Ca (Fig. 3.27) is to excite the atom from the ground  $4s^1 S_0$  to the  $4p^1 P_1$  state

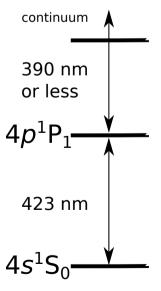


Figure 3.27: Neutral <sup>40</sup>Ca relevant structure.

with 423 nm light, then use any light with wavelength shorter than 390 nm to detach an electron. The resulting <sup>40</sup>Ca<sup>+</sup> ion (Fig. 3.28) is Doppler cooled (Sec. 2.2.1) at the

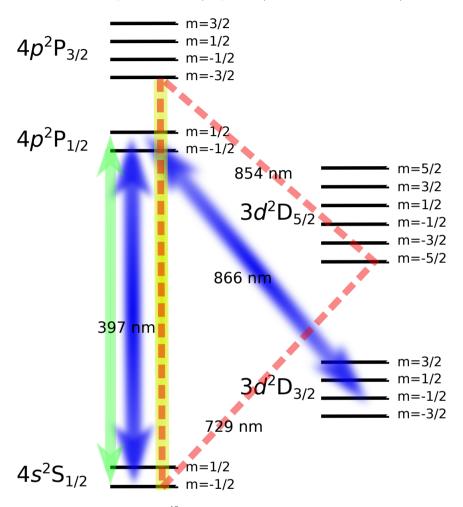


Figure 3.28: Singly ionized <sup>40</sup>Ca relevant structure with Zeeman splitting.

strongest dipole transition,  $4s^2 S_{1/2} \longleftrightarrow 4p^2 P_{1/2}$ , at 397 nm. There is, however, 6% probability [89] of decay,  $4p^2 P_{1/2} \leadsto 3d^2 D_{3/2}$ , which is a meta-stable state with a lifetime  $\tau = 1.2$  s [90], therefore 866 nm light is used to pump out of the  $3d^2 D_{3/2}$  and into the  $4p^2 P_{1/2}$  state.

A magnetic field of  $\sim 3-4$  Gauss at the position of the ion is used to access the Zeeman levels. The field is generated by a coil of  $\sim 6$ " diameter wound around the re-entrant viewport or the bottom flange, and two pairs of coils of about 3" diameter provide orthogonal fields in the plane of the bottom flange. Homogeneity is inferred by observing that, once the field and light polarization are tuned to enforce the chosen selection rules, no undesired transitions occur for ions over the extent ( $\sim$  5 mm) of the trapping volume. It was noted that the heat generated by running current in the coils is seen as pressure increase in the experimental chamber. For a given desired field  $H \propto IN$ , this is remedied by increasing the number of turns N in the coil and reducing the current I:

$$N \to \alpha N \& H = const. \Rightarrow R \to \alpha R \& I \to \frac{I}{\alpha} \Rightarrow P \to I^2 R/\alpha,$$

where  $\alpha$  is the scaling factor, R is the coil resistance and P is the power dissipated by the coil. For the experiment here, the bulk of the field was generated with  $\sim 1$  A in  $\sim 200$  turns of the 6" coil (expected best homogeneity for the target location).

Resolving the degeneracy allows for more efficient Doppler cooling as the superposition of the  $4s^2 S_{1/2}$  and  $3d^2 D_{3/2}$ , a dark state, can be avoided with a suitable polarization of the 397 nm light [91, 92]. An ion at  $T_D$  will have about  $n_D$  phonons (Eq. 2.7). For further cooling to the motional ground state (Sec. 2.2.2), the Zeeman structure of the quadrupole transition  $4s^2 S_{1/2} \longleftrightarrow 3d^2 D_{5/2}$  is exploited. Selection rules are enforced by suitable choice of the 729 nm light polarization  $\mathbf{e}$  and direction  $\mathbf{k}$ , and the direction of the magnetic field  $\mathbf{H}$ . After [93, 32], the condition  $\mathbf{k} \times \mathbf{e} \times \mathbf{H}$  is chosen to enforce  $\Delta m_j = \pm 2$ .

## 3.5.3 Photoionization Light

Multiple schemes for calcium photoionization have been demonstrated [94, 95, 96, 97]. The method used here (Sec. 3.5.2) is close to the one found in [98]. Photoionization light sources and their distribution for calcium changed several times over the course of the experiments. For 423 nm light generation, initially an 846 nm diode output was doubled by an external periodically poled crystal. The setup required a lot of attention and, over about a year, due to crystal aging, deteriorated

to outputting  $\sim 3 \, \mu \text{W}$  (at the chamber), a factor of 40 from the initially measured  $\sim 120 \ \mu \text{W}$  after coupling losses. While loading ions was still possible, sharing the light between experiments yielded sub-optimal results. The next installment utilized a direct diode laser in the Littrow configuration, mounted in an available in-house designed diode head. This ECDL provided plenty of optical power, however, since the mechanical and thermal stability of the head were not intended for a blue diode, wavelength tuning was a challenge. It was then decided to invest in a research grade system<sup>22</sup> which is currently in use. While this has been is the easiest system to use, the inherent difficulties associated with blue diodes are still present, notably the narrow mode-hop-free range and the extreme sensitivity to grating angle. The light is coupled at the head to a custom fiber beamsplitter, with a low power branch fed into an optical switch for locking (Sec. D.1), and a high power branch to deliver the bulk of the power to an experimental optical table, where it is distributed with fiber beamsplitters. A persistent problem with high intensity blue light is fiber tip damage, requiring periodic fiber tip polishing. Typically, 200 to 400  $\mu$ W reach the experimental chamber.

For the second stage of the photoionization process, 375 nm or 369 nm light have been used in the past. Currently, a 375 nm source<sup>23</sup> is set up. Since the exact wavelength is of no consequence, it is not monitored or controlled, and the only relevant issue is fiber tip damage, mitigated with mechanical shutters in the beam path before coupling into fibers. Typically, 200 to 400  $\mu$ W reach the experimental chamber.

 $<sup>^{22}\</sup>mathrm{DL}$  pro head with SC 110, DCC 110, and DTC 110 controllers from Toptica.

<sup>&</sup>lt;sup>23</sup>Obis from Coherent.

## 3.6 Ion Cooling, Detection, and Imaging

The main components in the imaging stack used for both experiments are an objective with about 0.29 effective NA, a CCD camera<sup>24</sup>, and a PMT<sup>25</sup>, one of the latter two selectable with a mirror. The CCD camera is used to image device features and ions and for position based measurements, and the PMT is used for all fluorescence based measurements.

#### 3.6.1 Doppler Cooling and Detection

Light from  $^{40}$ Ca<sup>+</sup> fluorescence is detected, imaged, and cooled on the 397 nm  $4s^2$  S<sub>1/2</sub>  $\sim 4p^2$  P<sub>1/2</sub> transition. In the presence of a magnetic field, unpolarized 866 nm repump light is tuned a few MHz blue of resonance, and red detuned 397 nm Doppler light polarization is adjusted to avoid dark states [92] and optimize count rate. 866 nm light power is kept above saturation, and for most operations, Doppler power is kept at or well below saturation to reduce broadening. The 866 nm light is software locked (Appendix D.1), while the 397 nm light is locked to an atomic reference via a transfer cavity (Appendix A). The 397 nm light frequency and power are modulated with an AOM in a double-pass configuration. When switching the beam on and off, attenuation of 105 dB is achieved by adding a second AOM in a single pass configuration. At the chamber, the linear polarization is adjusted with a waveplate for maximum fluorescence.

#### 3.6.2 Sideband Cooling

Resolved sideband cooling on the  $4s^2 S_{1/2} \longleftrightarrow 3d^2 D_{5/2}$  transition is used to cool the ion close to the motional ground state. The specific algorithms used are given

<sup>&</sup>lt;sup>24</sup>Andor Luca R.

<sup>&</sup>lt;sup>25</sup>Hamamatsu H10682-210.

in Appendix E.3, while the principles are outlined here. Assuming an ion cooled to  $T_D$  and  $\Delta m_j = \pm 2$  as in Sec. 3.5.2, the first step in the process is preparing the ion in the  $4s^2 S_{1/2}(m_j = -1/2)$  state. To that end, the ion is first cooled to  $T_D$  and prepared in the  $4s^2 S_{1/2}$  state by turning the Doppler light off. Next, a  $\pi$ pulse<sup>26</sup> for the  $4s^2 S_{1/2}(m_j = +1/2) \rightsquigarrow 3d^2 D_{5/2}(m_j = -3/2)$  transition is applied. If the ion was not in the  $4s^2 S_{1/2}(m_j = -1/2)$  state already, the ion is excited to the  $3d^2 D_{5/2}(m_j = -3/2)$  state. This is a long lived state, so unpolarized 854 nm light is used to pump out of the  $3d^2 D_{5/2}(m_j = -3/2)$  state and into the  $4p^2 P_{3/2}$ state. The favorable branching ratios and the presence of the unpolarized 854 nm and 866 nm light ensure a quick decay to the  $4s^2 S_{1/2}$  state. Since neither of the transitions in this step is selective, there is a probability that the ion ends up in the  $4s^2 S_{1/2}(m_j = +1/2)$  state, in which case the part of the cycle starting with the  $\pi$ pulse has to be repeated. Since a measurement is never performed, repeating the loop 6-8 times prepares the ion in the  $4s^2 S_{1/2}(m_j=-1/2)$  state with high probability. This agrees with the observations and calculation in [32]. The transitions involved in the process are chosen because they form a closed loop with high probability.

Once the ion is in the  $4s^2 S_{1/2}(m_j = -1/2)$  state, a closed (with high probability) transition loop is available for resolved sideband cooling. First, a  $\pi$  pulse<sup>27</sup> for the  $4s^2 S_{1/2}(m_j = -1/2) \rightsquigarrow 3d^2 D_{5/2}(m_j = -5/2)$  transition red motional sideband is applied. Next, unpolarized 854 nm light is used to pump out of the long lived state and to prevent spontaneous decay to the other  $3d^2 D_{5/2}$  allowed levels. Combined with the favorable branching ratio, the ion ends up, after spontaneous decay, in  $4s^2 S_{1/2}(m_j = -1/2)$  with high probability, and with a reduced  $\bar{n}$ , since the ion is in the Lamb - Dicke regime. As the ion cools down, the  $\pi$  pulse length increases as the population in the sideband decreases. Providing for that in the experimental loop allows for optimization in terms of the number of steps needed and the lowest

<sup>&</sup>lt;sup>26</sup>In Rabi flop context, not  $\pi$ -polarized.

<sup>&</sup>lt;sup>27</sup>As there is no true Rabi flop on a sideband of a thermal state, the minimum time needed to invert the population.

temperature attainable. Repeating an optimized loop 35-40 times cools the ion close to its motional ground state.

The 729nm light setup is outlined in Appendix B. At the chamber, the polarization is cleaned with a polarizing beam splitter, creating a potential for amplitude modulation. A feedback loop to remedy that is in the works.

## 3.7 Summary

Microfabricated surface devices offer an avenue to implementing complex scalable structures suitable for QIP applications and beyond, however, their use requires additional consideration when designing and assembling the supporting apparatus. The shallow traps and small dimensions with a large area exposed to the ion constrain the usable UHV pressure range and reduce the tolerance to particulate contamination. The multitude of control electrodes puts unique demands on control voltage filtering inside and outside of the vacuum vessel. Helical resonators offer a good compromise between filtering and size as a means to generate adequate rf voltage for trapping, and computer controlled DAC cards are used for control voltage generation. The ionic species ( $^{40}$ Ca<sup>+</sup>) in the experiments here are produced by photoionization of neutral atoms effused by a resistively heated oven in the trapping volume. The trapped ions are Doppler cooled and imaged, and can be cooled close to their motional ground state by exploiting the Zeeman splitting of their energy levels in a controlled magnetic field.

# Chapter 4

# Ring Trap Design

This chapter details the design of a device tailored for retaining an equidistant chain of hundreds of ions. The four metal level technology (Sec. 3.1) available at design time made the concept of islanded electrodes feasible, and the ring trap is one of the first devices to utilize such islanded electrodes. After putting the device in perspective (Sec. 4.1), the decisions that lead to the fabricated design (Sec. 4.2) are motivated, and then the remaining design stages that naturally arose with experience are detailed: meshing (Sec. 4.4), field calculation (Sec. 4.3), field manipulation (Sec. 4.5), and design optimization (Sec. 4.6).

## 4.1 Purpose

Ion traps that can hold a ring of ions are not a novelty. Interest in the availability of such a device was seen in proposals and experiments from diverse fields. These include simulations and studies of Ising models with long chains [99], Hawking radiation [100], ion chain dynamics and quantum phase transitions [101, 102, 103, 104, 105], topological defects for QIP [106, 107], time crystals [108], and the Aharonov Bohm effect [35]. A growing area of research, multipole traps have been demon-

strated [109], and theoretically studied [110, 111, 112, 113] for different applications. For quadrupole traps, ring geometries succeed the so-called race track traps [114] and have been used to study electron capture [115], storage of protons and ions [116, 117, 118, 119, 120, 121], advances in mass spectroscopy [122, 123, 124], and phase transitions [125, 118, 119, 120, 121]. Furthermore, ring traps have been proposed for frequency standard applications [126], antiproton confinement [127] (demonstrated Mg<sup>+</sup> trapping but no antiprotons), and isotope separation [128]. The rings in all those experiments and proposals relied on successful implementation of a traditional four rod structure (Sec. 2.1.2) and were therefore relatively large (40 cm ring diameter in [128]). Successful devices that yielded experimental results did not provide means for electric field control in the tangential direction (along the trap "axis"), and trapped ion locations and crystal structure were determined by pseudopotential features and mutual Coulomb repulsion, preventing the formation of an equidistant chain.

The purpose of the device described here is similarly to trap a ring of ions, but achieve that in a microfabricated segmented surface trapping device. Even if such a structure exhibits perfect azimuthal symmetry, the symmetry of the resulting pseudopotential will be broken by the presence of stray electric fields (e.g. due to charged particles nearby) and the trapped chain manifests those fields as spacing irregularities. To reduce the effect of stray fields, control electrodes along the circumference are used to generate a corrective field.

## 4.2 Layout

The first step in designing a device is determining a geometry that will serve the purpose (Sec. 4.1) of the device, while being technologically feasible (Sec. 3.1). The hyperbolic Paul trap (Sec. 2.1.1) can trap multiple particles, but with limited usability. Since the rf null is a point, particles away from the rf null experience excess

micromotion, and there are no means to control the positions of individual ions. Unlike hyperbolic Paul traps, linear traps (Sec. 2.1.2) provide means for holding ion chains. This is achieved by confinement that is strong in directions transverse to the trap axis as compared to the confinement along the axis. The resulting rf null is a line along the trap axis. In such a regime, trapped ions typically see a harmonic potential (to lowest order) in the axial direction. This harmonic potential, in conjunction with Coulomb repulsion between ions, results in variations in the density of the ion chain [129] – ion spacing increases with distance from the chain mid-point. Linear segmented ion trap designs [30, 31, 32, 69, 73, 130] add the capability to approach the unequal spacing issue by replacing the harmonic potential with a quartic one [131] (anharmonic traps). The latter approach has been used (in conjunction with reduction of stray fields, c.f. Sections 2.4, 5.5) to demonstrate less than 5% spacing variation in the middle 8 ions of a 10 ion chain [73]. This result has been improved upon to include 20 ions below the 5% variation mark [132]. Scaling the anharmonic approach to larger chains, however, remains a challenge.

If one imagines bending a linear surface trap in the plane of the surface, one arrives at a ring-shaped trap geometry. Such a layout overcomes chain density issues related to both axial potential shape and Coulomb repulsion by virtue of symmetry. Since the trap axis closes on itself, assuming azimuthal symmetry, a harmonic trap neither occurs nor is needed to confine the ions to the trapping volume. In the absence of external fields, however, that would mean that an ion could be anywhere in that volume. With the forethought that external fields always exist, we trade azimuthal symmetry for cutting out and segmenting otherwise grounded inner and outer (radially, with respect to the central control electrode) annuli. Those segmented inner/outer electrodes are used to confine and manipulate ions and chains (Sec. 5.4) and to correct for undesired fields (Sec. 5.5). We thus arrive at the geometry depicted in Fig. 4.1.

In deciding on the trapping radius, we wanted to store about 400 ions separated

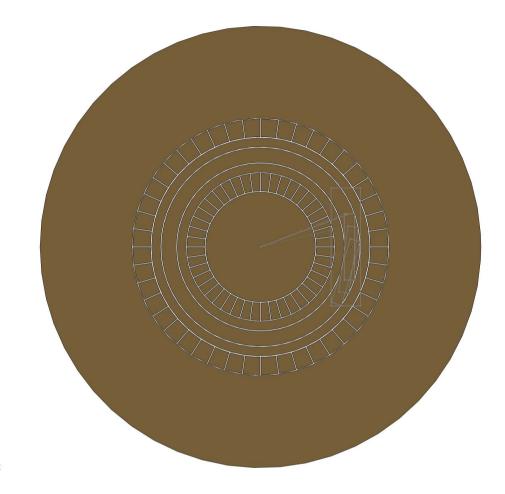


Figure 4.1: Ring trap layout.

by 10  $\mu$ m, requiring a 4000  $\mu$ m trapping circumference. Hence the required radius would be 4000  $\mu$ m/(2 ×  $\pi$ )  $\approx$  637  $\mu$ m. We choose the radius to be 625  $\mu$ m.

The widths of the rf and control annuli are chosen so that the simulated ion height (Sec. 4.5) is about 80  $\mu$ m. The widths can be optimized (Sec. 4.6) to achieve the desired trap parameters. The widths in the fabricated device are given in Fig 4.2.

The loading hole size is chosen to be the smallest technologically achievable at the time of design, 10  $\mu$ m diameter. The width of the gaps between electrodes is

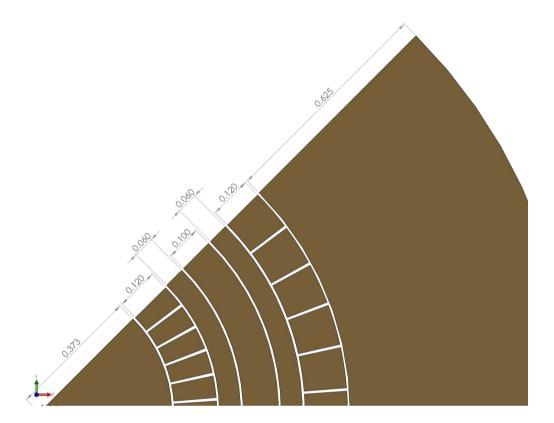


Figure 4.2: Ring trap dimensions, in microns.

also dictated by fabrication limits at the time to be 7  $\mu$ m. There are several reasons to aim to have the smallest possible interruption in the top metal layer. Although largely remedied by SNL fabrication processes (Sec. 3.1), a factor that encourages gap size reduction is the amount of dielectric that is potentially exposed to the ion [133]. In addition, any interruption of the surface creates potential "bumps" that may be difficult, if not impossible to deal with both in the design (Sec. 4.3) and in the operation (Sec. 5.4) the trap. Finally, gaps on the surface take space - if they have no purpose other than separating electrodes, they should be reduced. At some point of this reduction, the possibility of arcing in vacuum because of potential difference between electrodes becomes relevant. This is not a concern with the voltages and gaps involved here.

In deciding on the number of segmented electrodes, the following was taken into account. Assuming the ion height is not much larger than the electrode extent, and that unlimited number of electrodes are available in a given area, the larger the number of electrodes, the smaller their size, hence the higher the curvature of the field they could produce at the ion height. That determines the smallest undesired feature of the potential that could be addressed and must be balanced with the contradicting requirement that a uniform field (due to a single electrode) may be desired. In an attempt to make simulating the electric field (Sec. 4.3) easier, each quadrant had the same layout. However, it turned out that exploiting symmetry when simulating was not necessarily a good idea, but at the time this was realized, the overall layout had been agreed upon. Pairing the control electrodes in the radial directions allowed balancing a stray radial field with two electrodes. The chip package (Sec. 3.1) had 96 available channels for control electrodes. That allowed up to 12 electrode pairs per quadrant. The central control electrode was not to be grounded, which reduced the available channels to 95. Thus, the number of electrode pairs was reduced to 11 per quadrant. The final tally is: 88 control electrodes grouped in 44 inner/outer, radially aligned electrode pairs, plus a control electrode running under the trapping volume are all used for static potential shaping, and a pair of rf electrodes is used for generating a quadrupole pseudopotential above the surface.

The design decided upon was drawn with SolidWorks<sup>1</sup> and passed to SNL MESA Fabrication Facilities staff for further processing and fabrication (upon finalizing the design). A model was exported for the next step, mesh generation (Sec. 4.4).

#### 4.3 Field Calculation

While in the design process the field calculation takes place after meshing (Sec. 4.4), it is necessary to outline how electric fields are simulated in order to explain why mesh

<sup>&</sup>lt;sup>1</sup>from Dassault Systèmes SolidWorks Corp.

generation is needed. There are quite a few ways to to solve the electrostatic problem of finding the electric field in some volume due to a charge configuration. Analytic solutions for special charge configurations (e.g. a sphere, an infinite line of charge, an infinite plane) can be derived or found in many texts covering electrostatics (e.g. [134]), however, solving the problem for arbitrary shaped and placed electrodes is not trivial. For electrode configurations in a plane, as in surface traps, limited analytic methods were developed and recently described in the context of ion traps [135, 136, 137, 138, 139]. Although these methods can handle gaps [139] in the conducting surface, field estimates may not be great. At present, numerical methods are still preferred for field estimation.

A brief description of the many available methods for electromagnetic field calculation, with references, can be found in [140]. As a side note, it seems the research and implementation of such methods intensified with the increased accessibility of computing power. This is relevant because in some methods the number of calculations increases as the square of the number of elements involved. An in-depth discussion of selected field solving methods commonly used in the ion trapping community can be found in [141], with GPL - licensed boundary element method (BEM) solver code and examples available at [142]. The field calculations in this work are also done with a BEM solver, using the commercial software package CPO <sup>2</sup>. The CPO version available was limited to handling 6000 mesh elements.

As an outline of how BEM works, we consider the electrostatic [134] case of a charged conductor in equilibrium, in which all charge occupies the surface and the charge density increases with surface curvature. In BEM, the surface that is a field source is broken into adjacent triangles (Sec. 4.4). Each triangle is given uniform charge density, which is a function of the voltage on the surface, the triangle size and possibly of the surface curvature. The field/potential at a point of interest in space due to the charged surface is calculated as the superposition of the fields/potentials

<sup>&</sup>lt;sup>2</sup>http://simion.com/cpo/

due to each triangle. Usually, the field is calculated on a regular grid spanning some volume of interest.

In the case here, a typical grid around the trapping volume has dimension  $101 \times 101 \times 71$  (in R, T, Z, respectively (Fig. 5.1)) nodes and the physical spacing between neighboring nodes along a given dimension is  $2 \mu m$ . In the course of experimentation, it was found that using algorithms to exploit layout symmetry resulted in additional undesired features in the calculated field. Because of that, a mesh of a sizable part of the device was used for simulation ( $\sim 1.5 \text{ mm}$  radius from the device center, the full die being about  $1 \text{ cm} \times 1 \text{ cm}$ ), at the expense of mesh resolution. A separate grid was populated for a voltage of 1 V on each of the 89 control electrodes as well as the rf electrode pair. The resulting 90 grids are manipulated to calculate pseudopotential and trap parameters. Since field calculation is fairly resource-intensive, in the last few iterations of mesh generation and field calculation, the process of calculating fields with CPO was completely automated using Sikuli Script<sup>3</sup> – an outstanding open-source tool for handling repetitive tasks. Field calculation is repeated for each change of geometry or mesh.

#### 4.4 Mesh Generation

The boundary element method (BEM) solver that is used to simulate electric fields (Sec. 4.3) given some electrode geometry requires that the conductor surface is broken into primitives, in this case triangles. The process is referred to as mesh generation. It turns out that the strategy used to arrive at the size distribution and number of mesh elements has consequences for the model quality, a figure of merit being the measured device parameters with a trapped ion.

To gain some insight into the matter, for a fixed geometry, the field was cal-

<sup>3</sup>http://www.sikuli.org/

culated for a number of different meshes (selected examples in Fig. 4.3), and then manipulated to extract trap parameters (tabulated in Table 4.1).

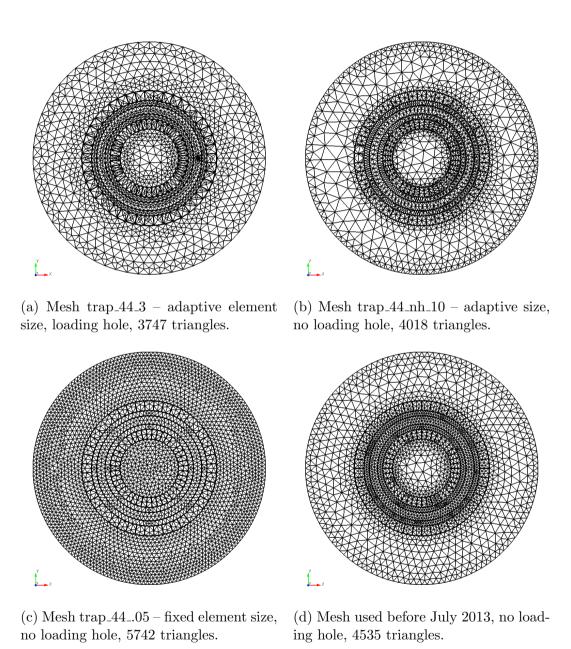


Figure 4.3: Examples of generated meshes.

What became evident from this effort is that a variance of 20 % in relevant trap

mesh id	$R (\mu m)$	$Z (\mu m)$	$\omega_R \; (\mathrm{MHz})$	$\omega_Z \; (\mathrm{MHz})$	$\omega_T \; (\mathrm{kHz})$	N	type
$\overline{\text{trap}_44_4}$	623.4	82.49	3.032	3.083	6.3i	3747	a
$trap_44_4$	623.9	83.22	3.038	3.021	18	2639	a
$trap_44_5$	622.7	83.23	2.992	2.915	48	1895	a
$trap_44_6$	624.1	83.15	2.954	2.944	2.2i	1571	a
$trap_44_7$	624.1	83.17	2.870	2.938	38	1409	a
$trap_44_nh_10$	624.5	82.24	3.061	3.123	4.0	4018	n
$trap_44.1$	621.1	78.50	3.421	3.468	21	1646	$\mathbf{c}$
$trap_44.05$	624.1	82.49	3.217	2.994	86	5742	$\mathbf{c}$
$trap_44_final$	624.2	82.11	3.106	3.124	0.34	4535	n
irregular	624.4	81.92	3.081	3.065	0.079	3998	n

Table 4.1: Mesh effects on trap parameters: R – trapping radius; Z – trapping height;  $\omega_R$ ,  $\omega_Z$ ,  $\omega_T$  – secular frequencies in R, Z, and T, respectively; N – number of mesh elements; type a – adaptive size strategy for mesh elements (small triangles near edges); type c – constant size of mesh elements, loading hole not present; type n – adaptive mesh size, loading hole not present. For a given trap geometry, different meshing strategy and parameters yield different calculated trap parameter values. The differences for radial secular frequencies ( $\omega_R$ ,  $\omega_Z$ ) projections can be  $\sim 20$  % of the value per direction, which suggests some convergence that is still tolerable. The differences in the projected tangential secular frequency ( $\omega_T$ ) show (i is the imaginary unit) that the modeling scheme is not a good predictor for behavior in this direction in the absence of a confining potential. Parameters are calculated for a Ba<sup>+</sup> ion, with 300 V amplitude and 40 MHz rf drive frequency.

parameter values can be attributed to meshing, and that calculating effects due to certain features of the geometry (the curved rf electrodes, the gaps between control electrodes, and loading hole) is not possible.

After the device was fabricated and thoroughly tested over a couple of years, a new look at the model was warranted by the need to better predict fields in order to achieve an equidistant chain. A new mesh incorporating feedback was generated (Fig. 4.4). The main difference between this mesh and previous attempts is that the size of the triangles is a function of their proximity to the point of interest around which the field/potential grid is populated. Trapping solutions obtained with the mesh kept the ion closer to the rf null, and the measured tangential frequency for a given trapping solution agreed better with the model prediction.

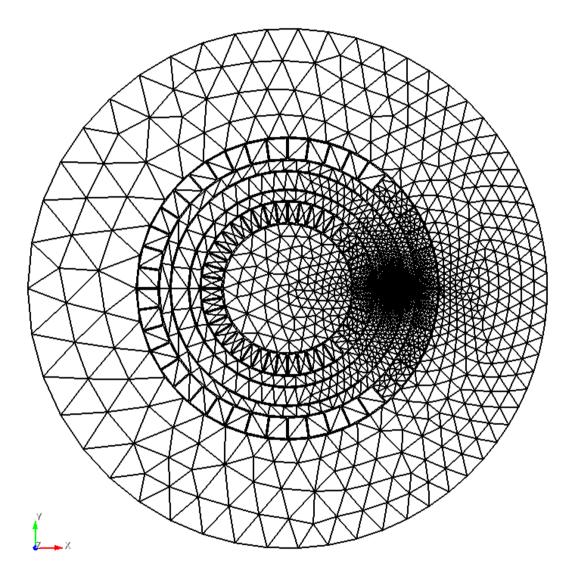


Figure 4.4: Ring trap mesh currently in use. Device loading hole is not modeled. The field is simulated around a point of interest, about 80  $\mu$ m above the 625  $\mu$ m radius intersecting the x axis. The mesh element size increases with distance from the point of interest, with 3998 triangles total. This mesh, generated in July 2013, produced parameters closest to those measured in the fabricated device (Sec. 5).

From the start, the meshing capabilities of CPO were avoided in favor of The CUBIT Geometry and Mesh Generation Toolkit <sup>4</sup> – a suite developed in part at SNL. Initially, device geometry was imported into CUBIT for meshing, but it became evident that re-generating the geometry in CUBIT was easier and evaded certain problems in vertex-matching. Moreover, recent versions of CUBIT benefit from full Python integration, making it possible to procedurally control the mesh size. The mesh generated with CUBIT was parsed in a suitable form for field calculation with CPO.

## 4.5 Field Manipulation

The generated fields and potentials (Sec. 4.3) resulting from a given mesh and layout are manipulated to extract trap parameters with Mathematica<sup>5</sup>, along the lines of (Sec. 2.1). First, data files are imported and parsed. The quantity

$$p = \frac{V^2 q^2}{4m\Omega^2}$$

(the ponderomotive constant) is calculated, where V is the rf drive amplitude, q is the elementary charge, m is the ion mass, and  $\Omega/2\pi$  is the rf drive frequency. The rf field magnitude  $E^2$  is calculated on the simulation grid, that is, the field due to applying 1 V to the rf electrodes that was calculated on the grid is dotted onto itself. The magnitude is interpolated for points that are not on the grid. The field magnitude is weighted by the ponderomotive constant and elementary charge to yield the pseudopotential (in eV) for an ion at location  $\mathbf{x}$  (Fig. 4.5),

$$U(\mathbf{x}) = E^2 \frac{p}{q}.$$

Since pseudopotential minima locations depend heavily on meshing, the volume is sampled and fits are run to extract an expected trapping radius R and height Z.

<sup>&</sup>lt;sup>4</sup>https://cubit.sandia.gov/

<sup>&</sup>lt;sup>5</sup>from Wolfram

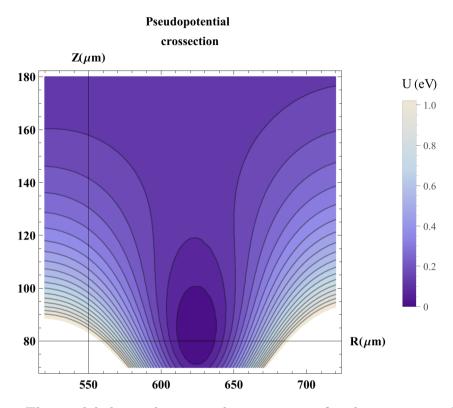


Figure 4.5: The modeled pseudopotential cross-section for the ring trap. R is measured from the ring center, and Z is measured from the surface.

Using the principle of superposition, on the simulation grid, the potential due to applying 1 V to each control electrode is weighted by the applied voltage and added to the pseudopotential. The control electrode potential is interpolated for points not on the grid. This is the total potential at the ion location. The applied voltages are typically chosen so that the sum of the field generated by the control electrodes has specific values at points of interest in the trapping volume. For example, weights can be chosen to create a harmonic trap in the tangential direction without affecting the orthogonal directions. Another example would be the generation of a homogeneous field for stray field correction. Trap depth is estimated as the potential difference between the local minimum and maximum of the total potential along the escape path of the ion in the simulated volume. This can be either done rigorously by explicitly finding the path, or roughly by assuming the path is normal to the surface.

The results for each technique are close for this design. Secular frequencies for motion in direction i are estimated for select minimum locations  $\mathbf{x}_m$  from the field curvature as

$$\omega_i|_{\mathbf{x}_m} = \sqrt{\frac{q}{m}\partial_i^2 U(\mathbf{x})}|_{\mathbf{x}_m}.$$

For the tangential direction, the directional derivative is replaced by a derivative evaluated along the location of the averaged trapping minimum curve, as opposed to along a tangential line. For select minimum locations  $\mathbf{x}_m$ , the principal axes rotation angle  $\theta$  (for axes normal to the tangent) is calculated as the angle of an eigenvector (a, b) of the Hessian matrix H of the total-potential

$$\theta|_{\mathbf{x}_m} = \tan^{-1} \frac{b}{a}|_{\mathbf{x}_m} \& H|_{\mathbf{x}_m} = \begin{pmatrix} \partial_Z^2 U(\mathbf{x}) & \partial_Z \partial_R U(\mathbf{x}) \\ \partial_R \partial_Z U(\mathbf{x}) & \partial_R^2 U(\mathbf{x}) \end{pmatrix}|_{\mathbf{x}_m}.$$

Secular frequencies  $\omega_1, \omega_2$  along the principal axes are calculated from the curvature along the axes. The stability parameter is estimated as

$$q_s = 2\sqrt{2} \frac{\max(\omega_1, \omega_2)}{\Omega}.$$

The amount of degeneracy is estimated as

$$\frac{|\omega_1 - \omega_2|}{\max(\omega_1, \omega_2)}.$$

Although the calculations themselves are not conceptually difficult, the amount of data being manipulated (a few gigabytes in memory for the grid described in Sec. 4.3 and 89 control electrodes + rf) presented problems for the software that inevitably manifested as stability issues. While most of the calculations performed are sufficiently well implemented in open source packages, a suitable 3-D interpolator was not found at the time of development. The existence of Mathematica's interpolation object is the core reason for using it for the analysis.

$d (\mu m)$	$r \; (\mu \mathrm{m})$	$R (\mu m)$	$Z (\mu m)$	$\omega_R \; (\mathrm{MHz})$	$\omega_Z \; (\mathrm{MHz})$	$\omega_T \; (\mathrm{kHz})$	U  (meV)
60	60	624.0	58.72	7.345	7.428	18	378
80	72	624.0	74.06	4.471	4.484	1.5	212
80	60	624.1	70.25	4.660	4.680	3.4	208
80	48	624.2	66.26	4.779	4.801	4.0	191
80	36	624.3	62.02	4.764	4.794	12	163
100	60	624.2	81.56	3.134	3.153	4.4	123

Table 4.2: Ring trap geometry optimization. d – central control electrode width; r – rf electrode width; R – trapping radius; Z – trapping height;  $\omega_R$ ,  $\omega_Z$ ,  $\omega_T$  – secular frequencies in R, Z, and T, respectively; U – trap depth. The target parameter here is  $Z \sim 80 \mu \text{m}$ .

## 4.6 Model Optimization

To optimize the trap electrode geometry for a given target parameter, the geometry is first re-generated with changes, then a new mesh is generated, fields are calculated from the mesh, and finally the device parameters are calculated. This resource-intensive procedure was not carried out beyond finding a suitable geometry for the target ion height (Table 4.2) and observing trends, because of the lack of automation options at the time of initial design.

Another optimization study explored the effect of the proximity of the top metal level rf lead on trap parameters. It was thus determined (Fig. 4.6) that the rf lead does not perturb the pseudopotential if it is brought up to surface at 1.5 mm away from the trap center. If it is closer, a significant defect is introduced in the symmetry of the ring's pseudopotential. As of the time of the latest mesh generation (July 2013), the process could be completely automated by parametrizing the geometry generation in CUBIT, using Sikuli to control the field generation, then using Mathematica to calculate parameters, all of that wrapped in a Python script.

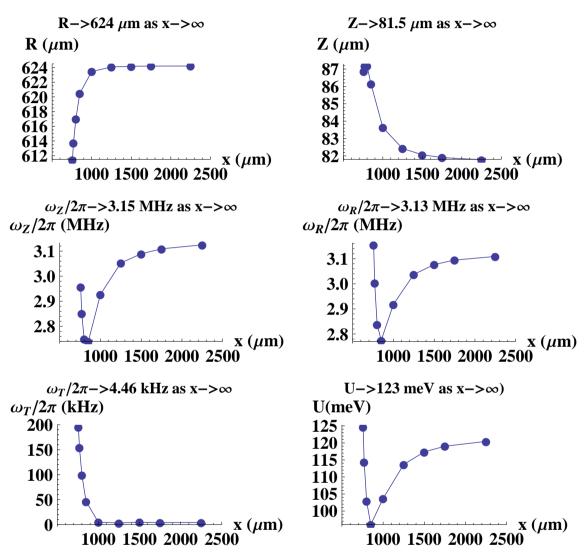


Figure 4.6: Effect of rf lead proximity on top level metal on trap parameters. R – trapping radius; Z – trapping height;  $\omega_R$ ,  $\omega_Z$ ,  $\omega_T$  – secular frequencies in R, Z, and T, respectively; U – trap depth. The horizontal axis is the radial distance x ( $\mu$ m) of the top layer rf feeding electrode from the trap center. Results are obtained by adding the field generated for 1.5 mm (in R) by 0.1 mm (in T) electrode surrounded by ground to the field of rf electrodes simulated on a quarter wedge. Meshing artifacts may add up to 20% error to this estimate.

## 4.7 Summary and Outlook

The process of designing a microfabricated device permits a well-structured approach. First, a surface geometry with desired features is identified. In the case described here, because of symmetry, a ring is chosen to store a large number of ions under identical conditions. Such a device could enable experimental research in diverse fields beyond QIP. Technological limitations and available features were factored in at the time of design. The electric field expected from the layout is estimated with BEM after meshing the surface, and trap parameters are calculated from the field, based on the pseudopotential concept. The choice of mesh has a large impact on the field estimate, as is evident from the variance in the estimated trap parameters. The process of choosing a layout, meshing, field calculation, and parameter estimation is iterated to optimize the layout geometry.

An interesting study for future work would be to relate mesh generation to measured device parameters. To that end, mesh size can be procedurally controlled, and parameters recalculated, to find the best agreement between model and measurements. In terms of design development, it should be noted that the electrode configuration is not a unique one satisfying the symmetry requirements above. For example, the inner or outer annulus of control electrode segments can be offset by half an electrode width, or control electrodes can be laid out on only the inner or outer annulus, or a different number of electrodes can be laid out in the inner/outer annuli while obeying the symmetry requirements. It is possible to also hide the loading hole from the top metal layer by putting it, for example, inside an additional slot splitting the central control electrode, and thus eliminating the expected bump in tangential direction. It would be also interesting to look at a scaled down or smaller device, as the larger electrode density would enable finer field corrections, and direct comparison in electric field noise in scaled devices can be made for devices fabricated on one die.

## Chapter 5

# Ring Trap Experiments

Experiments with the ring trap described in Chapter 4 are outlined in [76]. The goal of this chapter is to provide additional details on experiments conducted with these devices. The trap layout makes it natural to work in the frame of a trapped ion (Fig. 5.1). In such a frame, the tangential (T) direction (positive counter-clockwise) is the analogue of the axial direction for a linear trap, the radial (R) direction points outward from the circle center, and Z is the direction perpendicular to the trap plane. The specifics in Fig. 5.1 refer to the device used to build the equidistant chain.

#### 5.1 Fabricated Devices

Three devices were studied at SNL at different times. The first device used (Sec. 5.3) was one of the first fabricated with the four metal levels technology. The surface was not sputtered with gold, and the device had an initially floating electrode that was connected on the surface to the center ground disk via a wirebond. The second device used did not have electrode connectivity problems at the time of installation. The surface was sputtered with gold, and the remainder of the chapter describes efforts with this device (Fig. 5.2). Several devices identical to this one did not work well in

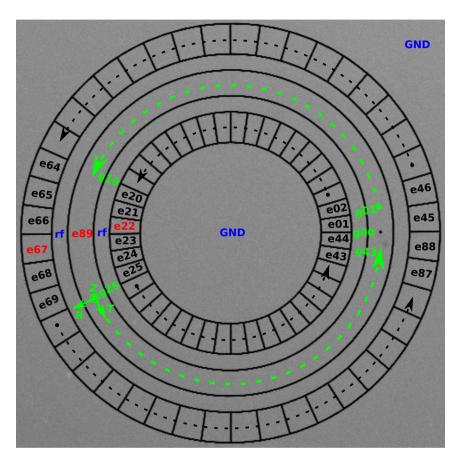


Figure 5.1: Ring trap nomenclature. Of the 89 available control electrodes, 86 performed as expected (black labels and dashed arcs), while e22, e67, and e89 (red labels) appeared to be shorted to ground at the time of experiment. The trapping volume is above the central control electrode, e89, and is designated by the green dashed arcs. The irregularities at the loading hole and the diametrally opposite location result from reduced control over the ion motion at these locations. The trapping sites at an intersection of the trapping radius and a radial line bisecting gaps between two outer control electrodes are labeled "gXX" and termed "gap" sites, with the loading hole at g00. Trapping sites at inner - outer electrode bisectors are labeled "eXX" and termed "electrode" sites. An R-T-Z reference frame is shown at g25.

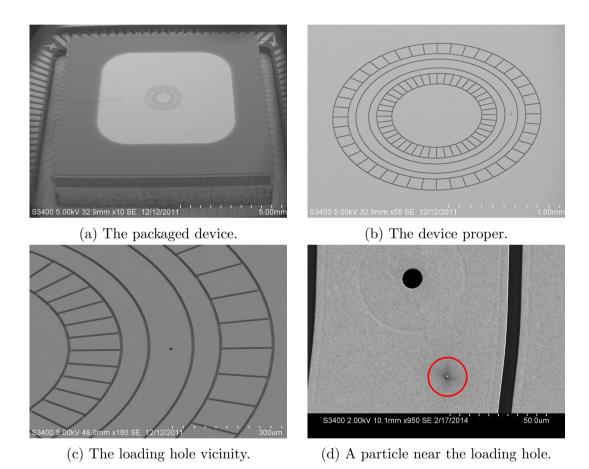


Figure 5.2: SEM Images of the ring trap. The images in a), b), and c) are taken at an angle, hence the elliptical appearance. Each image has a scale near the bottom.

an effort elsewhere [143]. The last device studied had half of the surface coated with gold and was used in the plasma treatment effort (Sec. 6) and will be covered there.

In Fig. 5.2a, a gold-sputtered device is shown at the center of a 1 cm  $\times$  1 cm die, placed on a spacer. Low profile wirebonds can be seen from the edge of the die to the CPGA pads (the light strands near the image edge). The rounded lighter tint square encompassing the device proper is the gold-sputtered area. The rest of the top metal level is aluminum. On the left hand side, the top level rf feed can be seen. The rf electrodes are connected to each other on a lower level metal at four symmetric points, in an effort to reduce possible phase offset between the inner and outer rf ring. The loading hole is on the diametrally opposite side from the rf lead. Fig. 5.2b depicts the device proper, laid out per the specifications in Sec. 4.2. Fig. 5.2c is an enlarged view of the section around the 10  $\mu$ m loading hole. The latter is shown magnified in Fig. 5.2d, along with what is possibly a large particle (1-2  $\mu$ m extent) on the surface (in the red circle).

#### 5.2 Experimental Setup

The UHV vessel used for most of the experiments described below is depicted in Fig. 5.3. The experimental chamber (Fig. 5.4) contains the packaged device, inserted into a ZIF socket, supported by two slabs, and mounted on four posts which are supported by the bottom flange. The ZIF socket is soldered into the filter board, and the control lines are connected through in-vacuum cable to the bottom flange feedthrough. The device is in the centroid of the chamber, about 7 mm below a reentrant viewport. The viewport is equipped with a stainless steel mesh ( $\sim 88\%$  transmission) screen (Fig. 5.5) electrically connected to the chamber, for the purpose of screening the device from accumulated charge on the viewport.

The experimental chamber design provides for through optical access along 3 axes

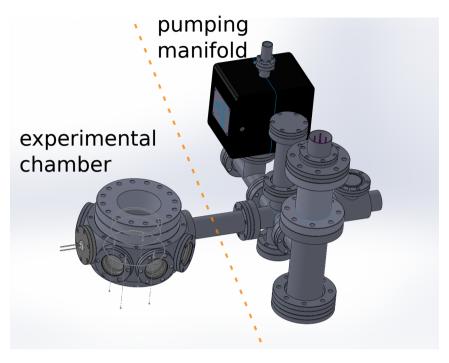


Figure 5.3: Ring trap experimental chamber cartoon. The dashed line separates the experimental chamber from the getters manifold.

(Fig. 5.6). A magnetic field (Sec. 3.6) is used to improve Doppler cooling efficiency and allow resolved sideband cooling. Most ion trapping experiments don't require working with more than few ions at a time. Moreover, these ions are often localized over an area of at most a hundred microns square. In contrast, this experiment required cooling hundreds of ions on a 625  $\mu$ m radius ring simultaneously and imaging them while minimizing scatter, which places unique requirements on the experiment. The profile of the beam used for the job is shown in Fig. 5.7. The imaging stack and the measurement Doppler beam (spherical lens,  $\sim 35\mu$ m waist diameter) are mounted on motors to enable motion and imaging automation on the ring (Appendix D.3).

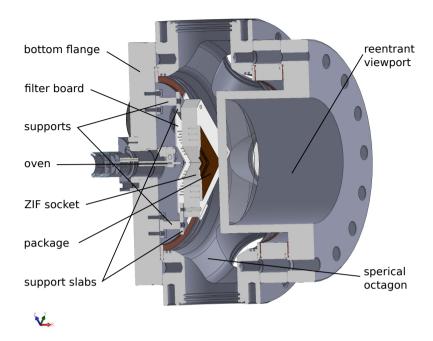


Figure 5.4: Ring trap experiment chamber detail.

## 5.3 Preliminary Studies

Several major results came out from the initial study with the aluminum surface device. Most of all, ions were trapped in the device, proving that both the design



Figure 5.5: Installed device with the screening mesh on the re-entrant viewport.

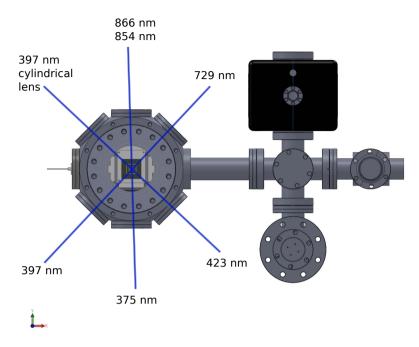


Figure 5.6: Ring trap experiment laser setup. The net magnetic field at the ion is in direction normal to the page. The device loading hole would be at 12 o'clock.

procedure and the fabrication procedure were sound. The device trapped ions over a wide range of rf power / control voltage scale settings, exhibiting a large stability space. The device provided a comparison point in terms of parameters for subsequent identical devices. In view of the shorted electrode, a control solution was developed allowing routine shuttling of an ion around the circumference more than 10 000 times without ion loss. The solution relied on interpolation between solutions at symmetry



Figure 5.7: Doppler beam profile for cooling the ring of ions. The beam size at the waist is on the order of 100  $\mu$ m by 3000  $\mu$ m.

points (g and e sites) and was customized to exclude the shorted electrode for sites nearby.

Despite a considerable effort focusing on relaxing the potentials, only short-lived 2-3 ion chains were assembled with the device, before it was retired in favor of the gold sputtered device. Shortly after the new device was deemed operational, a  $\sim$  50 ion chain was demonstrated (Fig. 5.8) by shuttling ions from the loading hole

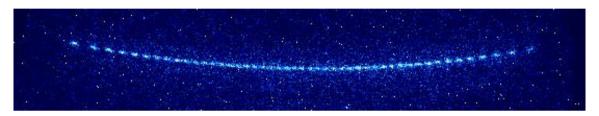


Figure 5.8: The first long chain demonstrated. The chain was formed at the location diametrally opposite the loading hole.

to the diametrally opposite site and relaxing a potential well formed with control electrodes there. At that time, it became clear that the infrastructure had to be upgraded to address the needs of the experiment. This primarily included writing an experimental control platform (Sec. D) to allow synchronized ion shuttling, cooling, and imaging, along with locking lasers and controlling instrumentation.

Several changes were made as part of this upgrade. First, the rf resonator resonance frequency was increased to  $\sim 53$  MHz by putting a small capacitor in series between the device and resonator. Next, a variation on the loading strategy above was attempted. The strategy (Fig. 5.9) relied on shuttling ions to multiple relaxed wells(pockets) which resulted in a number of long chains around the ring. Relaxing the wells, however, led to ion bunching in two location, instead of an equidistant chain.

After months of infrastructure development, the behavior of the system was quite comparable (Fig. 5.10). However, the tools permitting a systematic approach were now in place and tested in a different experiment (Sec. C). One of the first uses of

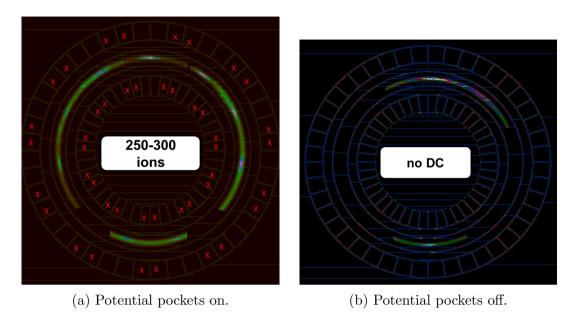


Figure 5.9: Multiple long chains in potential pockets. A red "x" designates an electrode on which a positive voltage is applied, forming a number of potential pockets.



Figure 5.10: Chain in the ring trap before correction. The segment shown corresponds to what is at 12 o'clock in Fig. 5.9b. The gap in the chain is due to the loading hole potential bump.

the fine control the system offered was to explore the effect of the expected potential bump at the loading hole (Fig. 5.11). This undesired effect was not quantified, be-

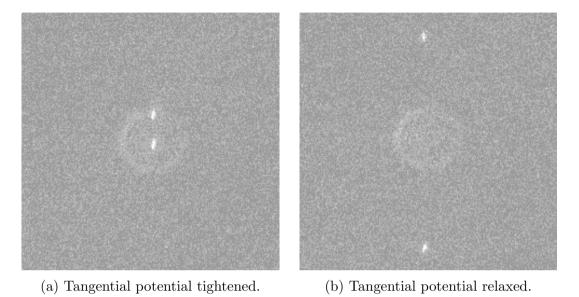


Figure 5.11: Clear evidence of loading hole potential bump. The bright dots are the ions, and the circle is unfocused scatter from the loading hole. The ion chain is split when the tangential potential is dominated by the loading hole bump.

cause the fields near the loading hole were not entirely predictable or reproducible. One possible explanation is that nearby particulate contaminants (Fig. 5.12a) were being charged (via photoelectron emission or through the strong gradients) by the near UV photo-ionization light. Counter-intuitively, small particles may be difficult to catch with SEM imaging (Fig. 5.12b), unless their location is approximately known, due to low contrast. Finally, it is possible that surface scatter is due to inherent surface roughness that sometimes occurs during fabrication. Surface roughness may not be easy to distinguish from a particle. Other means to explore the surface for contamination are white light interferometry and Energy Dispersive Spectroscopy (EDS).

Yet another observation came from subsequent attempts to shuttle an ion chain around the device. It was established that, depending on the number of ions in the

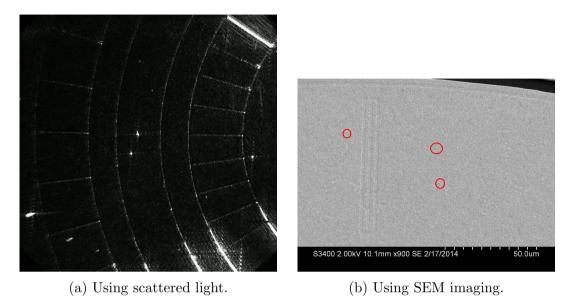


Figure 5.12: Locating particulate contaminants on the surface. Scattering light off the device surface reveals a large number of particles but at that point it is too late to remove them. The SEM image was taken from the ring trap (after removal from the chamber), at a location with high scatter.

chain and the potentials used, it may not be possible to shuttle all of the ions past the location diametrally opposite the loading hole. Upon further study, three electrodes were measured to be shorted to ground (Fig. 5.1). This was not consistent with the observed propensity of ions to congregate there, but meant that the fields in the vicinity were not controllable. The set of usable sites was thus limited (assuming only g sites should participate) to locations g00 - g19 and g25 - g43. While it was initially believed that the device was faulty, a subsequent (post-experiment) check showed the device was fully functional. Another working hypothesis was that the in vacuum filter board (Fig. 3.22b) was coated with  $^{40}$ Ca from the oven, thus shorting channels. However, that was not checked until after a number of prolonged exposures to air that would have allowed complete oxidation of the metal, thus eliminating the short and the opportunity for verification. Moreover, it was accidentally found that along the long chain of connections between a control electrode and its voltage source (Sec. 3.4), connector pins were damaged at an unknown time, resulting in

intermittent connections. In short, the reason for the lack of access to those electrodes at the time of experiment is still undetermined.

Finally, the setup was used as a testbed for resolved sideband cooling of  $^{40}\mathrm{Ca}^+$ , and motional heating rates were measured for the first time at SNL with this technique. A heating rate of 0.95(20) quanta/ms was measured for the tangential mode at  $\omega_T \approx 2\pi \times 0.9$  MHz.

## 5.4 Stray Field Measurement

With operational experimental control allowing hours of uninterrupted work, it was possible to systematically characterize stray fields over the extent of the device. From here on, unless otherwise explained, referring to an ion at some location means that the ion was loaded at the loading hole and then shuttled to the site of interest where it was cooled and imaged or detected with the PMT. The first step in the procedure most often employed to achieve that is to park the detection optics and the measurement Doppler beam at the site of interest and turn on the atomic oven. Next, in order to minimize avoidable UV exposure, PI light at the loading hole site is only unblocked after some pre-determined time needed to achieve a sufficient flux of <sup>40</sup>Ca. Upon PI light exposure, a shuttling cycle between the loading hole site and the target site is started. Finally, upon detecting or imaging an ion, the shuttling cycle is stopped, the oven is turned off, and the PI light is blocked.

It was decided that measurements would be taken at symmetry points only (g and e sites). The rationale behind that is the reasonable expectation for a small spread in the absence of undesired fields. Because of the inaccessible electrodes and the desire to achieve a  $\sim 1$  MHz tangential frequency within the 20 V pp range of the generating DACs (also commensurate with the breakdown voltage expectations), a control solution comprised of four inner and outer electrode pairs was used. The solution

tilted the principal axes by about 15 degrees, allowing adequate Doppler cooling of all modes at most locations. Given the locations of the problematic electrodes, a contiguous arc (Fig. 5.1) of 39 gap sites (out of 44) was available for study.

Radial fields (Fig. 5.13) are assessed at q sites on the arc with the following se-

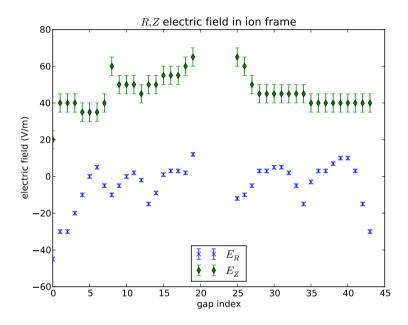


Figure 5.13: Radial fields for the measurement locations.

quence. First, a parametric resonance scan (Sec. 2.4.1) with a single ion at a given site is obtained, followed by a cross-correlation scan (Sec. 2.4.1). Next, pre-determined control voltages are applied that, according to simulation, create a uniform field of known magnitude that pushes an ion along the R or Z direction at the site. The preceding steps are applied until the parametric resonance and cross-correlation features are minimized. Minimization is confirmed by ensuring the features grow upon increasing the field in the given direction. The fields that minimizes the features are (within the simulation and experimental error) the negative of the stray field at the site.

To asses tangential fields (Sec. 2.4.2) at the g sites, one measurement of the

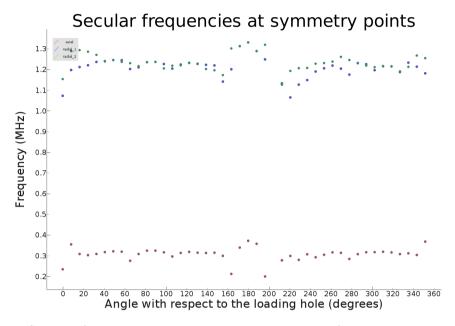


Figure 5.14: Secular frequencies around the ring. Note the features at the diametrally opposite location to the loading hole. It is likely that the ions were not exactly at the nominal g location. The radial directions frequencies are at about 1.2 MHz for the rf power used.

tangential secular frequency per site is needed. One way to capture all three secular frequencies (Fig. 5.14) is the use of a "tickle" voltage. The method relies on the anharmonicity of the true potential (i.e. a Duffing oscillator [144] model for the axial direction), which is manifested in a fluorescence change observable when the potential is modulated at the secular frequency. In practice, an rf voltage (the tickle voltage) is applied to a nearby electrode, chosen so that the field has components along all three axes at the ion location, and the frequency is scanned. In addition to the fluorescence features, characteristic smearing of the ion can be observed in the respective direction, when the tickle frequency matches the secular frequency.

The other component of tangential field (Sec. 2.4.2) measurement is the displacement of the ion (Fig. 5.15) upon scaling the potential. To that end, for an ion at a given location, an image of the ion is taken for each different voltage scale. Since there is no reference feature other than the ion, it is imperative that the imaging

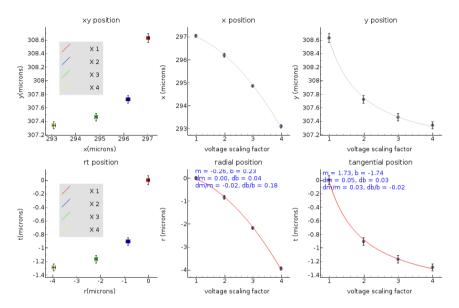
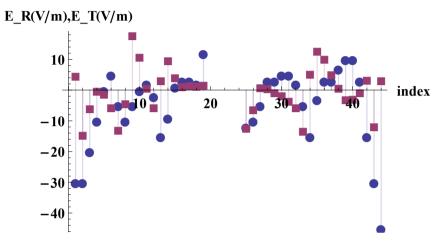


Figure 5.15: Tangential displacement extraction. Four potential scales are used in this example, from  $1 \times$  to  $4 \times$ , with a step of  $1 \times$ .

system does not move for the duration of the experiment. From the images, relative locations for the ions are extracted and converted to the respective R-T frame, and T displacement is inferred. The displacement is used with the secular frequency to calculate the tangential field  $E_T$  (Fig. 5.16a).

In the hope that a pattern may emerge corresponding to a long range field, the fields measured in the R-T frame are converted to a local X-Y frame (Fig. 5.16b), yet no patern was revealed. Given the amount of effort needed to collect the data, a relevant question is how fast do the fields change. Fig. 5.17a shows the tangential fields at time t and 5 days later, and Fig. 5.17b shows the change in tangential fields from time t to a month later. Another important feature of the field is its smoothness. This can be seen in Fig. 5.17a: the data depicted with squares is twice as dense as the initial data (circles), because the field was assessed at e sites in addition to g sites. The field is reasonably smooth, as the changes of sign may be interpreted as the site being on one side or another of a charged particle (or some other field source nearby). An ion moving towards a charge would see the field appear in a different



(a) Measured stray fields in the R-T frame.

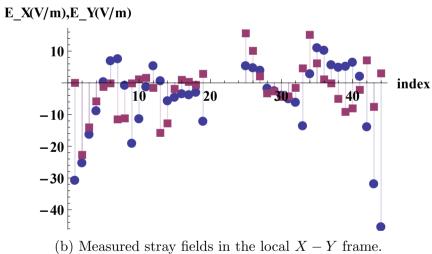
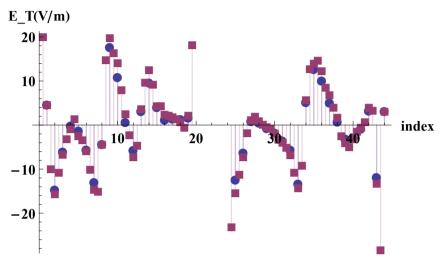
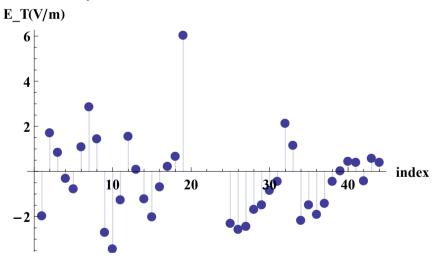


Figure 5.16: Measured stray fields in the plane of the device. Changing the reference frame did not offer new insight.



(a) Two tangential field measurements separated by five days. The data depicted by squares were taken five days after the data depicted by circles. The data depicted by squares were taken at g and e sites to assess stray field smoothness.



(b) Tangential field change over a month.

Figure 5.17: Tangential field change over time. Details are in the text.

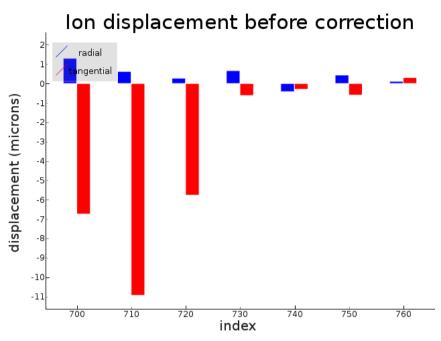
direction than one moving away from the charge.

#### 5.5 Stray Field Correction

With the focus on achieving an equidistant chain, a sound strategy would be to try to reduce the fields in the tangential directions. For that purpose, one electrode was assigned to correcting for each measurement location. Electrodes e69 to e88 and e45 to e63 (39 total) were selected for the correction. The field that a single electrode produces, as modeled, extends over the trap to all measurement locations. Hence, the effect of all participating electrodes was taken into account at all measurement locations. Because of the symmetry, the field from all electrodes was calculated for only one location, the one with the densest mesh, and rotations were applied to simulate fields at the rest of the locations. Therefore, the problem was reduced to finding weights on the participating (correcting) electrodes, so that the total produced field negated (according to simulation) the measured field. This is captured in the expression:

$$-\begin{pmatrix} E_1 \\ \vdots \\ E_{39} \end{pmatrix} = \begin{pmatrix} e_1^1 & \dots & e_1^{39} \\ \vdots & \ddots & \vdots \\ e_{39}^1 & \dots & e_{39}^{39} \end{pmatrix} \begin{pmatrix} \alpha^1 \\ \vdots \\ \alpha^{39} \end{pmatrix}, \tag{5.1}$$

where  $E_i$  is the measured tangential field at location i,  $e_i^j$  is the simulated tangential field at location i due to one volt applied to electrode j, and  $\alpha^j$  is the weight, or actual voltage applied to electrode j. Before the focus shifts to the main result of the study (Sec. 5.6), a digression is warranted to answer the question: what happens between the g sites? As was shown in Fig. 5.17a, the tangential field was well behaved at locations that would not be used in the correction calculation. There is no guarantee, however, that the correction would not change that in an undesirable manner. To check for that, the displacement upon scaling (which is proportional to the field) was measured and corrected for at four g sites by inferring the field, and was only



(a) Before the correction is applied.

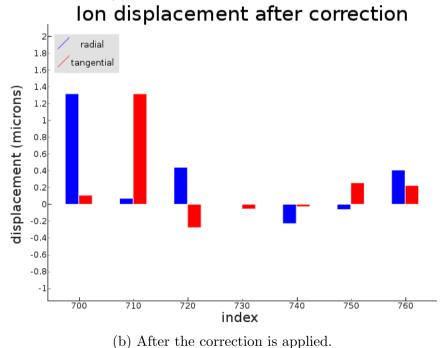


Figure 5.18: Displacement upon scaling at intermediate locations. The correction applied is calculated from the displacements (upon control electrode voltage scaling) at indices 700, 720, 740, and 760 only, but the corrective effect is seen at the intermediate sites, at indices 710, 730, and 750.

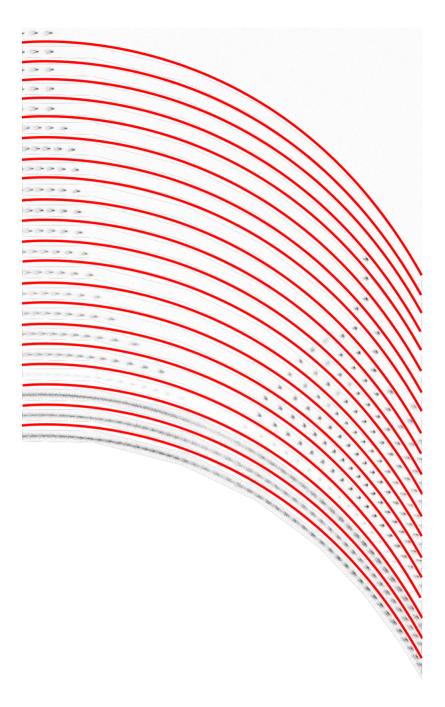


Figure 5.19: Scaling the corrective field in the ring trap. Each red line delineates an image taken with a 5% increase of the corrective voltage, from top to bottom. There are only 2 ions in the region without a correction applied, while the region (corresponding to an angle of about 45 degrees, an octant) is fully populated as the correction is fully applied.

measured at the intermediate three e sites, before and after the correction at the g sites was applied. The results (Fig. 5.18) show that the fields are smooth enough so that the correction effect extended between the correction sites, thus justifying the initial assumption of homogeneous stray fields. Fig. 5.19 further supports this conjecture.

#### 5.6 The Equidistant Chain

Applying the correction to the contiguous region of locations q00-q19 and q25-q43allows filling the ring with ions (Fig. 5.20). The magnification in the imaging system balances the contradicting requirements of high resolution and a large field of view, and can capture almost a quarter of the ring. To image the whole chain without losing resolution, images are taken along the ion chain at 45 degree rotational increments, starting at g00. Because there is no feature that can be used as a reference at the focus distance for imaging ions, once the camera has been moved, the exact knowledge of the number of ions is lost. This lack of reference is the reason for manually composing the image on Fig. 5.20 from overlapping images taken in each octant. From continuous imaging of an octant, It was observed that an ion was lost every few minutes, and the ring was still populated after hours of cooling the long chain. In fact, at the time of experiment, device performance was tuned well enough to allow more than 7 hours of cooled life-time for single  ${}^{40}\mathrm{Ca}^{+}$  ions. Some interesting features were not quantified but are worth mentioning. The first of them is loading dynamics. Although the potential is sufficiently smooth to allow imaging the long chain, it seemed that Coulomb repulsion played a large role in the final potential, which should be expected. This is supported by the observation that ions were loaded in separate wells around the circumference and then spilled over, as their aggregation modified the well. Loading the full ring took about 5 minutes. Another expected yet interesting feature was the formation of complex 3-D crystals in the location opposite

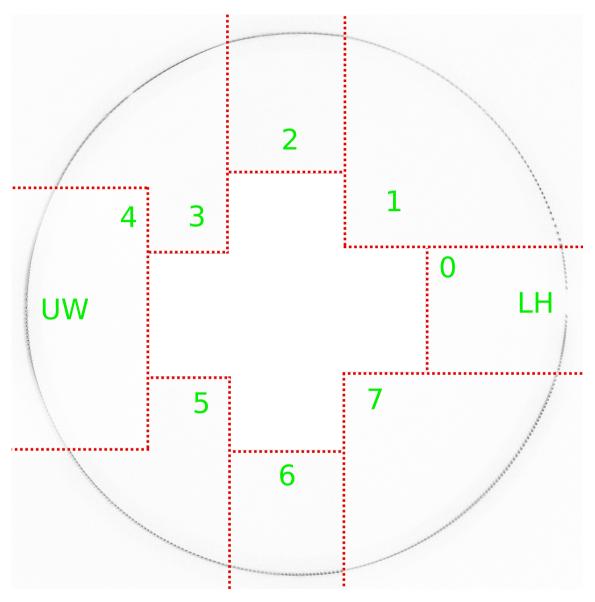


Figure 5.20: The ring trap filled with ions. The red dots designate the original image boundaries. The numbers are octant labels. LH designates the loading hole gap, and UW designates the unwanted well that attracted ions.

the loading hole, depending on the rf drive voltage and the ion density. By varying the focus, a helical structure was observed on several occasions. Finally, the spots which were populated with ions last seemed to correlate with known nearby particles on the surface, suggesting the particles may be a stray field source.

To quantify the effect of the correction, tangential fields were measured again, with a single ion, after applying the correction (Fig. 5.21). Indeed, the field was

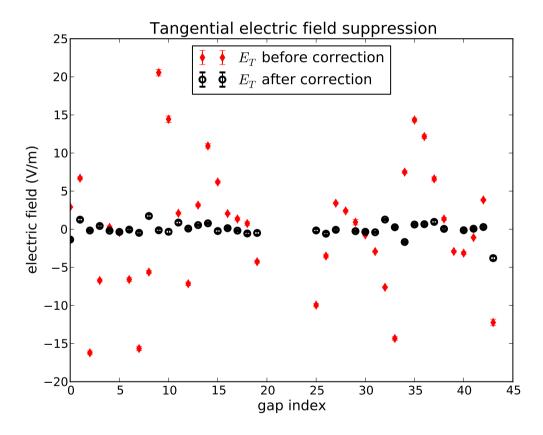


Figure 5.21: Tangential field for the measurement locations before and after correction.

reduced at the measurement locations.

Another metric used to quantify the correction was the distance between ion pairs. For that purpose, ion positions were extracted from the images of octants 5,6, and 7, and distances were calculated (Fig. 5.22). The average distance between

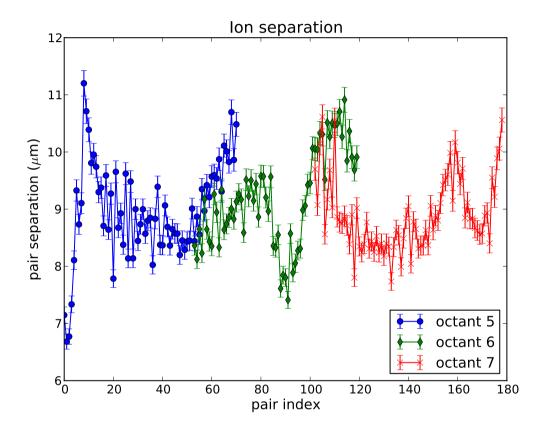


Figure 5.22: Ion separation after applying the correction. The error bars are based on the uncertainty of the total magnification, but the positions are not corrected for aberrations at the edge of the collection optic. This image accounts for the overlap of the original images.

neighboring ions, as seen from the picture, is about 9  $\mu$ m. The reason to be hesitant with statistics in this case is the imaging system. The imaging stack was never fully characterized, so none of the images is corrected for aberrations. The reason that only three octants are used is that all ions could be resolved in only these octants, without image processing. From the resolved images, it is estimated that there are about 400 ions in the chain. It is quite possible that a better estimate can be made by counting the ions on Fig. 5.20, especially when magnified.

Besides aberrations, there are other factors that possibly contribute to the perceived smearing of ions. The first of them is the different focus distance at different points along the ring, resulting from the trap plane not being parallel to neither the imaging stack translation plane nor the camera. Another possibility is that the ions' motion was excited at these locations and the chain did not crystalize, due to some unintended feature of the device or the surface contaminants. Such motion would be consistent with rf pickup from electrodes. Yet another option is inadequate cooling. It is possible that the Doppler beam was ever so slightly misaligned at the time of taking the image, and the chain was not cooled well locally. For a flat beam parallel to the surface and passing above the ring center, a rotation of 1 degree would move the beam by 11  $\mu$ m at 625  $\mu$ m radius. Along the same lines, an aligned flat beam could only work for ions in a plane. Without an accurate method to assess the ion height, the constant ion height is only an assumption.

#### 5.7 Summary and Outlook

The route to engineering an electric field, subject to geometric constraints and available degrees of freedom but otherwise arbitrary, in a segmented surface device is exemplified by assembling a long ion chain in the ring trap. Approximately 400 ion chain with  $\sim 9~\mu \mathrm{m}$  ion to ion distance is demonstrated after measuring the stray electric field at multiple locations and calculating a field correcting the tangential component of the stray field at the measurement locations. For that purpose, high level of automation is implemented in the experimental setup and control, allowing taking the necessary measurements over several hours.

A future experiment could improve the results by employing different strategies for measuring and applying a corrective field, and using all available degrees of freedom. One such strategy could be based on assigning more electrodes to regions with larger field curvature. Some combination of correcting the radial fields and the tangential fields could also be explored. An obvious improvement in the design of a new device would be the removal of the loading hole from the top metal level, as outlined previously (Sec. 4).

The results from the experiment can also motivate the simulation of a new device and its performance near stray field sources, with the aim of finding a geometry that optimizes the generation of an arbitrary field for a fixed number of available control electrodes. Given that experimental imperfections are not necessarily avoidable (e.g. dust particles have been found in the clean room), such a simulation could be a gauge for the feasibility of designing a new ring trap for some of the experiments that motivated the initial effort. While imaging imperfections prevent stricter interpretation of the ion spacing results, it is unlikely that the current device, as designed and as performing, will come close to the requirements laid out in some of the motivating proposals. In particular, a successful device would have to be capable of maintaining a crystal in which the secular frequencies for ions (with temperatures on the order of  $\mu$ K) could be resolved within a few Hz [103] – a regime that is out of reach, even for a small chain. At the same time, by virtue of the device geometry alone, the device could still be useful in an experiment as the one studying the Aharonov - Bohm effect [35].

### Chapter 6

# Treating Surface Traps with Argon Plasma

This chapter details the implementation of the plasma treatment effort, with emphasis on its ion trapping aspect. Details on the plasma generation and characterization aspects can be found in [145]. A brief discussion of anomalous heating (Sec. 6.1) will motivate the need for this experiment. The experiment premise (Sec. 6.2) will be followed by a motivation of the choice of the device predominantly used for the experiment (Sec. 6.3). Next, the experimental apparatus is discussed (Sec. 6.4), followed by a discussion of capacitive plasma discharge (Sec. 6.5). Next, details on implementing inductive plasma discharge (Sec. 6.6) are presented. The procedure for measuring heating rates is deferred to (Sec. E.3). Heating rate results are discussed for pre-treatment (Sec. 6.7) and post-treatment (Sec. 6.8) measurements. As this is an active investigation, future work is outlined (Sec. 6.9).

#### 6.1 Anomalous Heating

Trapped ions experience heating - the acquisition of energy by means of electric field noise coupling to the ion's motion. For coupling to occur, the electric field noise must exhibit components at the secular frequencies of the motion. While heating is inevitably observed, little is known about the mechanism through which the electric field noise is generated. A number of competing models have been developed in the efforts to tackle the issue, yet none of them conclusive. Anomalous heating [146, 147, 71], as the phenomenon is termed, is particularly relevant to microfabricated surface ion traps. The reason for that is that heating increases dramatically as the ion approaches the surface, putting a limit on device miniaturization. Two models that pertain to this study are those of adatom diffusion and adatom dipoles. These models predict different dependence of the noise density S in terms of mode frequency  $\omega$ , ion-to-surface distance, and trap temperature. Of these parameters, the only one that can be explored with this experiment is the frequency, as the secular motion frequency may be varied by changing the rf and control voltages. By measuring  $S \propto \dot{\omega n}$  for different mode frequencies, a specific model can be validated.

#### 6.2 Study Premise

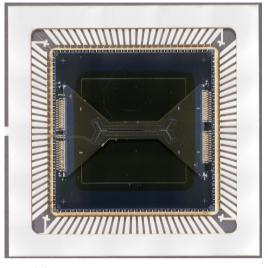
The results of several experiments focusing on surface contamination removal imply that the source of anomalous heating is surface adsorbates. Laser ablation [148] was successfully used for heating rate reduction, at the expense of peeled off electrodes and removed gold from the surface. Argon ion beam bombardment with 500 eV to 2000 eV beam energy [149] and 300 eV beam energy was also shown to reduce the heating rates of the respective devices. The energies involved, however, are well above the sputtering threshold (an atom sputtered for every ion) of 25 eV for gold (the surface metal in allthree studies). A recent experiment [150], very much along

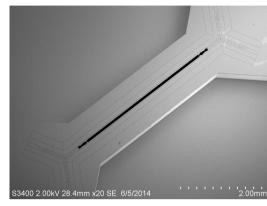
the lines of this work, also demonstrated successful heating rate reduction, but the plasma energy was not calibrated and it is therefore not known how likely it is that sputtering occurred.

The goal of the study is to explore whether the removal of carbonaceous contaminants from the surface of a surface electrode ion trap with an  $in\ situ$  Ar plasma treatment that does not cause structural (via sputtering) surface changes has an impact on the device heating rate. The associated work [145], demonstrates that, indeed, the presence of carbon is virtually eliminated from gold and aluminum surface after calibrated, low energy ( $\sim 20\ {\rm eV}$ ) Ar plasma treatment, and that no detectable sputtering occurred on a device with a gold/aluminum interface. Furthermore, oxygen is also removed from the gold surfaces but not from the aluminum surface, as is expected given the large Al-O binding energy. The question of whether the removal of these compounds alone is sufficient to reduce the heating rate remains open.

#### 6.3 HOA2 Device Details

The first device used in this effort was a ring trap, discussed in Sec. 6.5. Subsequently, we decided to attempt trapping in a newly designed and fabricated (Fig. 6.1b) High Optical Access, Rev. 2 (HOA2) device for several reasons. First, a ring trap offers the advantage that, for a fixed laser direction, a different proportion of the laser **k** vector will be along the ion motional modes depending on the ion's position along the circumference. However, a heating rate study should be performed at multiple points with a consistent laser direction relative to the motional modes. This is the case with a linear device, such as the HOA2, which has several large linear regions. Next, the ring trap is a true surface device - all electrodes are in one plane, and the ion is always above the device metal. The HOA2, on the other hand, has most of the slotted region electrodes on the third metal level, with short segments at the slot ends that are on the top level. The HOA2 device also has regions with top





- (a) The packaged HOA2 device.
- (b) A SEM image of the HOA2 device.

Figure 6.1: The HOA2 device used for most of the experiments.

metal electrodes, providing three distinct regions to explore in terms of ion proximity to metal. A single ion was successfully shuttled multiple times through all three regions. As the device name suggests, the HOA2 provides excellent optical access, as compared to most other surface device designs. Thus, the exposure of surface contaminants to laser light, which can produce stray electric fields, is reduced [151] and cooling is not inhibited by excess micromotion. The improvement in optical access transverse to the slot is achieved (Fig. 6.2) by virtue of the characteristic "bow-tie" shape of the die, wirebonded to an interposer (providing signal routing and equipped with 1 nF trench capacitors) with low profile wirebonds congregated at the ends of the "bow-tie". The interposer is wired to the package with low profile wirebonds as well. For a comparable rf drive, the HOA2 device generates a trap with a potential depth about an order of magnitude higher than that of the ring trap. Without micromotion elimination, a cooled ion lifetime exceeding 8 hours was observed ( $^{40}$ Ca<sup>+</sup>), and dark times exceeding 1 minute were measured.

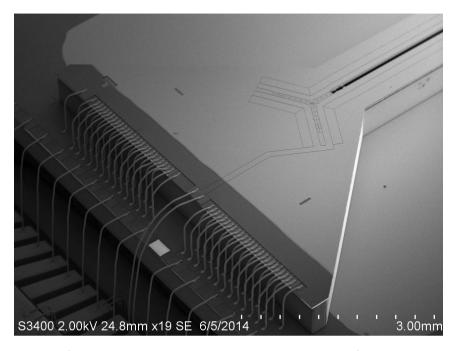


Figure 6.2: Achieving high optical access with a microfabricated device.

#### 6.4 Chamber Modifications and Setup

Initially, the ring trap chamber described in Sec. 5.2 was used. During the course of the experiment, however, the chamber design evolved as issues were tackled. In what follows, the current state will be described unless otherwise noted. In exterior view (Fig. 6.3), the chamber was functionally redesigned to allow gating off the getters manifold with an all metal bakeable gate valve<sup>1</sup> while flowing argon for plasma generation from a 1.33" all metal bakeable angle valve<sup>2</sup> added to the bottom flange (not shown on the picture) to the pump-out valve shown. A two-part optics support assembly was also added to the experimental chamber.

Inside the chamber (Fig. 6.4), the functional changes included replacing the screening mesh with a solid metal plate with a cutout for imaging, insulated from the rest of the conductors in the chamber and electrically connected for plasma biasing to

<sup>&</sup>lt;sup>1</sup>Series 48 2.75" valve from VAT.

 $<sup>^{2}9515014</sup>$  from Agilent.

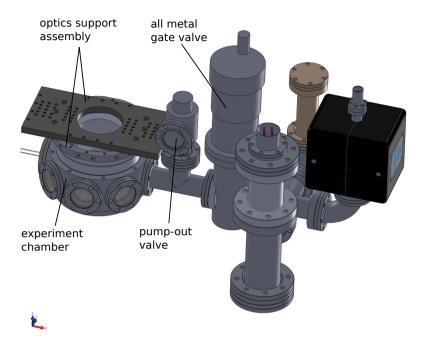


Figure 6.3: Functional changes to the chamber. A path for flowing argon is provided by adding an inlet valve at the bottom of the chamber (not shown) and pumping out through the valve shown. A gate valve is added to avoid saturating the getters with argon with minimal penalty on system conductance.

the 100 pin Micro-D connector on the bottom flange. The only physical components that survived all changes were the in vacuum 100 pin Micro-D connector and cables and the ZIF socket support slabs. Everything else (oven, filter board, ZIF socket) was changed due to component failures. The supports were trimmed to account for the height added by the interposer on the HOA2 package.

The use of the two-part optics support assembly shown in Fig. 6.3 and Fig. 6.4 is also seen in Fig. 6.5. The round part of the support, not seen in this picture but in the other two, is put on top of the reentrant viewport and baked with the chamber. The rectangular part, seen in all three images, is attached to the round part before or after a bake, thus registering anything attached to it to the chamber. In this case, the imaging stack and the 423 nm PI light are registered. The importance of this is that, once imaged, a device image is displaced by at most a few hundred microns

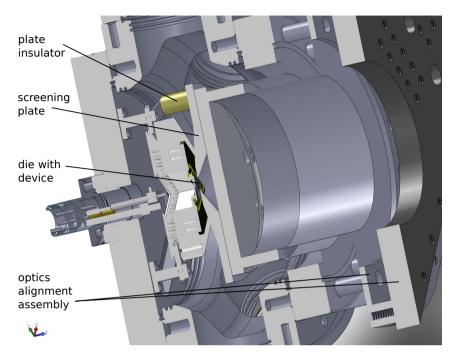


Figure 6.4: Functional changes inside the chamber. The screening mesh is eliminated in favor of an insulated screening plate in order to apply a bias voltage.

(due to the loose fit of screws in the plane of the device) when the rectangular plate is reinstalled, saving hours, and sometimes days of effort to image the trap after a bakeout. Similarly, 423 nm light (that could be used for imaging the trap) is at most a few hundred microns from its nominal position in the plane of the device. So, minimal adjustments in the direction normal to the device plane (camera focus and 423 nm light height) is all it takes to image a device. In addition, <sup>40</sup>Ca can be imaged before a bakeout to confirm the atomic oven is operational. In aggregate, this small contraption adds a lot of value when devices are often changed. Sadly, it was only conceived and used at the end of this research.

The next change (Fig. 6.6) from the ring trap setup is the addition of a gas manifold for introducing Ar into the experimental vessel and a pumping station to pump it out from the pump-out valve. The rationale behind using a two port system is that although the flow is limited by an orifice, it helps avoiding the formation of

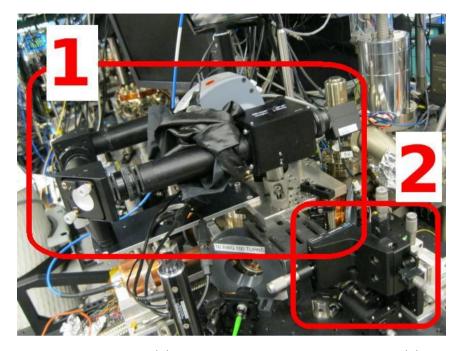


Figure 6.5: The imaging stack (1) and the 423 nm PI light launcher (2) are registered to the chamber through the optics support assembly.

Ar pockets in the vessel. Details of the manifold itself are in [145].

Finally, the optical setup (Fig. 6.7) is changed to benefit from the long linear segment of the HOA2 device. The device is installed so that its slot, in which most of the measurements are taken, is along the direction of the 866 nm, 854 nm, 375 nm, and 423 nm beams. Thus, only the Doppler and 729 nm beams need to be moved when the trapping location is changed. In addition given that the principal axis is tilted from the direction normal to the page, all three motional modes of an ion can be cooled.

#### 6.5 Capacitive Plasma Discharge

The first device used in this experiment was a ring trap (Fig. 6.8). Initially, surface treatment was performed with a capacitive plasma discharge [152]. For that pur-

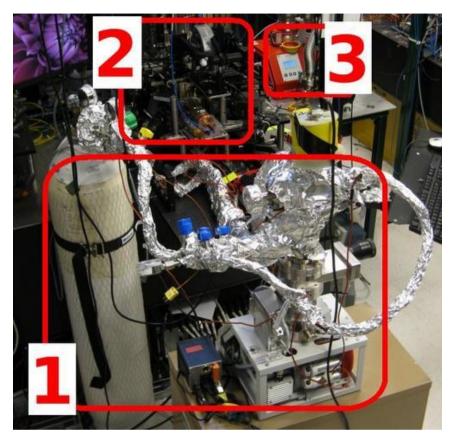


Figure 6.6: The gas manifold. Ar is introduced into the chamber (2) from the gas manifold (1), and is pumped out from the pump-out port with the pumping station (3).

pose, the device package had to be modified to allow rf delivery - a labor intensive procedure, which later became one reason to discard this approach. Another reason that capacitive discharge plasma did not work well was the difficulty in localizing the plasma. Even when the plasma was eventually localized, it was difficult to control the plasma location - the plasma surrounded the device without covering it. Finally, the operating energies were not well controlled, leading to severe package damage in some cases.

On the ion trapping side, this device is of interest because half of the device was gold-sputtered in anticipation of enabling comparison of ion behavior over the two metals (sputtered gold and native aluminum). This was the first device at SNL to

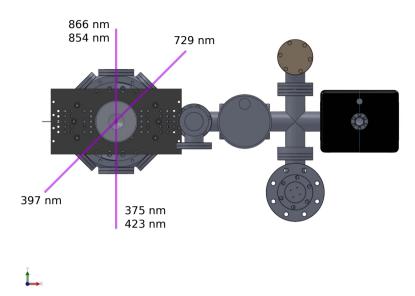
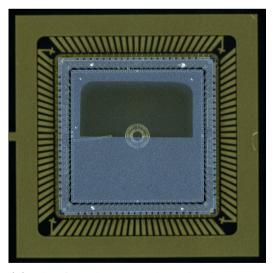
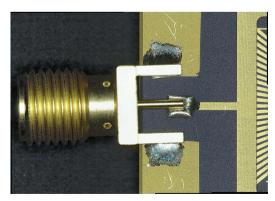


Figure 6.7: Laser setup, optimized for loading at multiple locations.



(a) The first device with multiple metals on the top metal layer.



(b) An SMA connector is attached to the package.

Figure 6.8: The ring trap device used for the capacitive discharge effort.

feature multiple metals exposed to the ion, and a point of investigation was whether the metal interface could be traversed despite the difference in work functions. While traversing the interface worked well, the primary goal of having the device in vacuum – cooling an ion motional mode to its ground state, and subsequently measuring the heating rate, failed. The reason for that was that the device was severely contaminated with macroscopic particles, and quite possibly, Doppler cooling left the ion at a temperature far above  $T_D$  and preventing sideband cooling. An estimate using the sidebands envelope [153] method suggested that at best,  $\bar{n} \sim 40$ . Eventually, non-localized capacitive discharge was initiated, after which trap performance deteriorated further.

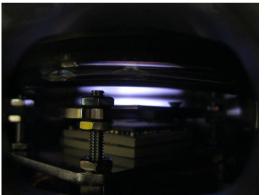
#### 6.6 Inductive Plasma Discharge

Inductive plasma discharge [154, 152] is used in the remainder of the effort. Inductive discharge is characterized with better control and localization, and with lower plasma energies. Inductive plasma can be generated without any modification to the package or chamber. A coil is brought into the recess of the reentrant viewport after the imaging stack is removed, and the screen inside vacuum serves as ground. The resulting plasma sheet density is highest between the viewport and the screen, but can be controlled by biasing the device surface. While learning about inductive plasma parameters, we also learned that the chamber parts could not handle the energies involved. In particular, during plasma discharge, the current in the mesh was sufficient at times to heat and deform the mesh considerably (Fig. 6.9). Although this happened with a relatively high plasma rf drive that was not anticipated to be used for surface treatment, it meant that repeatability of results would be compromised by the flexibility of the mesh. Hence, a solid stainless steel screen was designed, with rigidity and optical access in mind. Not much was known about the screening efficiency of the plate at chamber assembly time, yet it seems to perform at least as

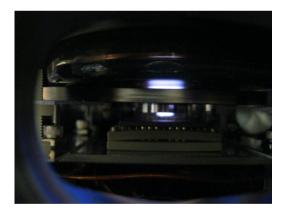


Figure 6.9: Mesh screen damage during plasma generation. Argon plasma is seen as the cloud with a purple/pink hue. The red/orange bulge is a heated and deformed mesh screen similar to the one covering the viewport in Fig. 5.5.

well as the mesh. The screen plate is electrically insulated from the remainder of the vacuum vessel with four ceramic standoffs, and is wired to the bottom flange Micro-D connector. Inductive plasma parameter space was thoroughly investigated in a







(b) Localized plasma.

Figure 6.10: Inductive discharge plasma in a test chamber. The non-localized plasma shown is an example of a mild case of lost localization. In some instances the plasma occupied most of the chamber available volume.

test chamber and in the experimental chamber to ensure that localization (Fig. 6.10) is well understood. The plasma energy was calibrated with a retarding field analyzer [145], and it is estimated that the energy used for the successful removal of

contaminants from the surface was  $\sim 20$  eV [145].

#### 6.7 Heating Rates Before Treatment

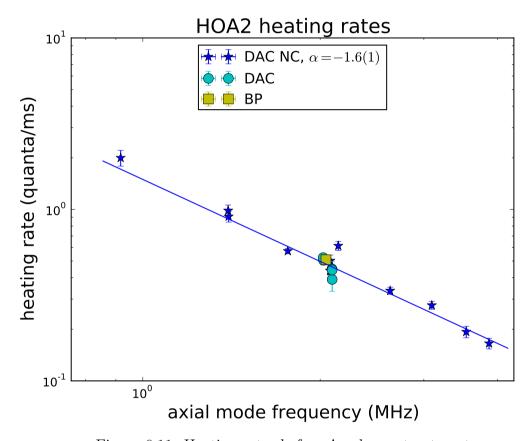


Figure 6.11: Heating rates before Ar plasma treatment.

Following the procedure in Appendix E.3, heating rates at various locations and under varying conditions were measured before treatment. Fig. 6.11 depicts the results of a representative subset of the measurements in the middle of the slot of the HOA2 device. Data points labeled "DAC" pertain to measurements after stray fields were minimized, in which control voltages were supplied by the NI DAC cards. Since only the axial mode temperature is measured, stray field minimization was

not performed for the set labeled "DAC NC". This set also explores the functional dependence of the heating rate with mode frequency, yielding

$$\dot{\bar{n}} \propto \omega^{-1.6(1)} \tag{6.1}$$

$$\Rightarrow S \propto \omega^{-0.6}$$
. (6.2)

To check if the measurements were influenced by DAC noise, a battery pack was used to provide voltages (label "BP"). Measurements taken at other trapping sites exhibited comparable consistency.

#### 6.8 Heating Rates After Treatment

After a satisfactory amount of heating rate data was collected over a range of conditions, the point of no return was reached by initiating an inductive plasma discharge (Fig. 6.12). The plasma parameters used were 0.25 Torr argon pressure, with 4 Watt

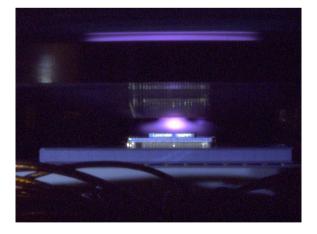


Figure 6.12: Localized plasma in the experimental chamber.

of plasma rf power at 72 MHz, over 300 seconds. This set of parameters was known to remove carbon from a gold surface (as was the case with the device in the chamber) below the detection level immediately after treatment [145]. After that, once the

pressure was near  $\sim 10^{-10}$  Torr, heating rates were measured again (Fig. 6.13, label "after treatment"). Surprisingly, there was no sizable change in the heating rates,

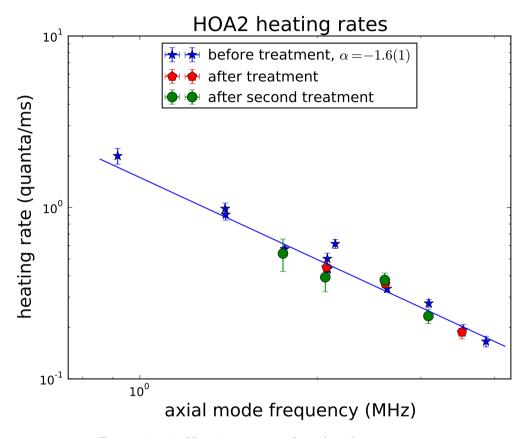


Figure 6.13: Heating rates after Ar plasma treatment.

so, on the suspicion that carbon re-deposition occurred over the 300 seconds of exposure, a second treatment with shorter exposure was applied. The parameters for the treatment were 0.5 Torr argon pressure, with 4 Watt of plasma rf at 72 MHz, over 60 seconds – another set known to eliminate carbon immediately after treatment [145]. Heating rates were measured again (Fig. 6.13, label "after second treatment"), and again there was no sizable change in the measurement result.

This observation permits several interpretations. The first of them is that we did not reach the technical noise limit in the experiment. The change incurred by the treatment was below that limit, however, that is unlikely to be the case, given the results of measurement with a battery pack. Another possibility is that the amount of carbon deposited is larger than anticipated and we did not apply treatment that is aggressive enough to detect a difference. Indeed, during bakeout, CO<sub>2</sub> and H<sub>2</sub> are outgassed from stainless steel, and it is likely that outgassing from the unusually high amount of polymers in the chamber (PCB, ZIF socket, etc.) would dwarf the contribution from steel. A third option is that carbon was initially removed, however, it was re-deposited with time. While this was shown [145] to be a true statement, it is unlikely to be the explanation at the relevant time scale. Finally, it is possible that carbon was removed, however reordering of the surface (via sputtering) is needed in order to reduce the electric field noise.

Incidentally, a sample was explored that was attached with a piece of carbon tape to a sample holder. for that sample, an unusually high amount of carbon was found after treatment. At the same time, it turned out that the device die was attached with a conductive epoxy with a high carbon content, and that epoxy was exposed to plasma. It was then decided to change the die attachment process, so that no carbon compounds are in the vicinity of the device, and the chamber was vented. Over the course of two months afterwards, two devices in which the die was attached with solder were installed and promptly destroyed by what turned out to be erupting <sup>40</sup>Ca pellets from the oven. After spending some time on studying the phenomenon, the reason for the oven behavior was accidentally traced to a cold joint in a cable that is used once every few months under normal circumstances. A third device (Fig. 6.14), prepared in the same manner as the previous two, is currently in the chamber. About one third of the slotted region of the device is sputtered with platinum, another third is sputtered with cold, and one third is native aluminum. The device was demonstrated to trap, and a pre-plasma treatment heating rate study is pending.

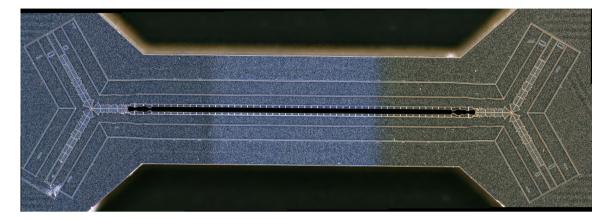


Figure 6.14: Third HOA2 device with three top metals, currently in the chamber. The different hue is due to a different metal on the surface. From left to right: platinum, aluminum, and gold.

#### 6.9 Summary and outlook

The premise that adsorbates on metal surfaces contribute to anomalous heating—the coupling of trapped ions to the unexplained ambient electric field noise is examined. Based on the observation that low energy plasma removes carbonaceous compounds from a gold coated surface, a heating rate measurement over a range of mode frequencies was taken in a gold coated device, before and after plasma treatment. Before treatment, the relation between electric field noise density and mode frequency did not agree with the models for field noise due to impurities adsorbtion. After treatment, no change in heating rates was observed. So far the experimental results do not justify a conclusion on whether surface treatment with low energy argon plasma has any effect the electric field noise at the ion location, as a source of carbon was found in proximity of the plasma.

A new device, packaged with a carbon-free technique, is currently in the experimental chamber. In addition to providing insight on the current results, the device may permit the unique measurement of electric field noise above three different metals under exactly the same vacuum conditions. Furthermore, in the light of the recently demonstrated reduction of heating rates above a Nb surface [150], it is not unlikely that a similar observation takes place, with the right plasma conditions, perhaps with energy above the sputtering threshold. Finally, the study may be combined with an *ex situ* argon beam cleaning preparation before the *in situ* treatment, in order to include the effects of reordering of the surface.

## Chapter 7

## Summary and Outlook

The focus of the work described here has been on overcoming engineering challenges pertaining to ion trapping with microfabricated surface ion traps. The first task at hand was the design of a circularly symmetric device – a unique topology with the potential to enable experiments not accessible with linear devices. In approaching the task, a design process was formulated, and limitations of the process were explored. The design process was improved upon after experiments with the fabticated device allowed progress towards reconciling the model with the physical device. The initial studies of the device - one of the first employing a four metal layer process, helped to set a perspective on what are reasonable expectations for devices fabricated with the process, both in terms of device performance and of fabrication yields.

The successful demonstration of the device was followed by a period of building infrastructure that would enable non-trivial experiments with the device. An atomic reference was built for the purpose of locking Ca<sup>+</sup> and Yb<sup>+</sup> Doppler cooling light to the reference. A transfer cavity was built and locked to the reference, and Ca<sup>+</sup> Doppler light was locked to the cavity. Software programs were written to allow locking of the remaining lasers to the atomic reference through a high resolution wavemeter. The venture into writing code expanded to writing a complete exper-

imental control system. The system was the core tool in obtaining the results for an experiment demonstrating the scalability of fabricated devices [78] (not detailed here).

With the infrastructure in place, the systematic approach to mapping and reducing the electric fields in the ring trap allowed the formation of a long and regular ion crystal, thus proving the method used to be a viable way to engineer an arbitrary electric field in an ion trapping device. The studies with the device led to design and fabrication feedback applicable to future development.

The next experiment discussed explored the potential for reducing electric field noise by means of "in situ" argon plasma treatment. Progress in this effort demanded improving a number of procedures and taking a critical look at failure modes of both devices and the supporting infrastructure. For example, targeted studies of quarter wave helical resonators, atomic ovens, and device burnout limits were carried out. In aggregate, these studies contributed a lot to the "what not to do" list. On the bright side, this experiment led to the successful demonstration of two variants of a previously untested device, including the shuttling of an ion over three different metals, and shuttling of an ion through electrodes with different height. While details in the experiment at this time prevent any conclusion on electric field noise reduction, a new device is ready to be explored, keeping the potential for contribution to the larger ion trapping community open.

## Appendices

## Appendix A

## Transfer Cavity Lock

The purpose of the transfer cavity scheme is to allow tight locking of light for which there is no suitable direct reference, to an available reference. In this case, light used for Doppler cooling of Ca (794 nm before doubling) and Yb (740 nm before doubling) is locked to a Rb reference at 780 nm. As with nearly all components of the experimental setup, the transfer cavity lock evolved substantially over time. Notably, the in-house built 780 nm source was succeeded by a research grade system<sup>1</sup>, and the lock was re-implemented to allow locking of 740 nm light in addition to 794 nm. Only the latest version will be discussed.

The transfer cavity is made of a 1" thick drilled Invar rod, two spherical mirrors with a radius of curvature of 7.5 cm, and a piezoelectric stack, for a cavity length of 10 cm. The free spectral range is 1.5 GHz, and the measured finesse is at least 160, yielding a spectral width of 10 MHz.

The 780 nm source schematic is given in Fig. A.1. An important feature of this implementation is that it makes available unmodulated light for other experiments, as follows. Light from the ECDL (D) is followed by an optical isolator (OI) to prevent

<sup>&</sup>lt;sup>1</sup>DL pro head with SC 110, DCC 110, and DTC 110 controllers from Toptica.

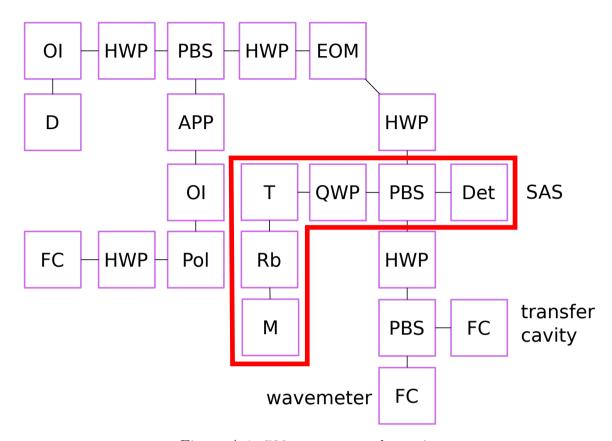


Figure A.1: 780 nm source schematic.

unwanted feedback. A  $\lambda/2$  waveplate (HWP) controls the branching at the polarizing beamsplitter (PBS). The branch that is used for saturated absorption spectroscopy (SAS) continues with a HWP, followed by an electro-optic modulator (EOM)<sup>2</sup>, used for frequency dithering. Another HWP and PBS split the light into the SAS branch: a  $\lambda/4$  waveplate (QWP) (adjusted to pass light to the detector (Det)), followed by a telescope (T) to enlarge the beam, followed by a natural abundance Rb cell (Rb), and by a back-reflecting mirror (M); the other branch is split again by a HWP and a PBS to provide a reference to the wavemeter and to the transfer cavity through the fiber couplers (FC). The signal from the detector is mixed with the local oscillator dithering the light to extract an error signal in a Pound-Drever-Hall (PDH) scheme<sup>3</sup>.

<sup>&</sup>lt;sup>2</sup>20 MHz resonant, from New Focus.

<sup>&</sup>lt;sup>3</sup>Implemented with a mixer, a bias T, and a splitter, all from MiniCircuits.

The unmodulated light before the EOM is passed through an anamorphic prism pair (APP), an OI, a polarizer (Pol), and a HWP to a FC, to be used in a different experiment. The light is locked to the D2 line F=3/F=4 crossover of <sup>85</sup>Rb as it yields a large and steep error signal.

The light from the 780 nm source is mixed with the EOM modulated light at 794 nm <sup>4</sup> and 740 nm into the transfer cavity with the help of a beamsplitter and a dichroic mirror. The cavity transmission is monitored. The back-reflection of the cavity is incident on a grating to separate the three colors, each of which is directed to a fast photodetector. The 780 nm light detector is used to extract an error signal to lock the cavity to the 780 nm light, and the other two colors are used to lock the respective ECDLs. The same PDH scheme is used for all three locks.

 $<sup>^4\</sup>sim$  GHz level fine control shift is provided by a voltage controlled oscillator from Mini-Circuits. An offset is implemented with EOMs from EOSPACE Inc.

## Appendix B

## 729 nm Light Lock

The 729 nm light source (Fig. B.1) is an ECDL locked to an Ultra Low Expansion (ULE) cavity, in a scheme along the lines of [155, 156]. The light from an ECDL

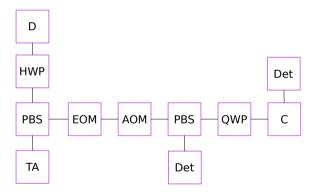


Figure B.1: Functional schematic for the 729 nm source.

(D) is split with a  $\lambda/2$  waveplate (HWP) and a polarizing beamsplitter (PBS) into a branch for locking and another for experimentation. The experimentation branch seeds a tapered amplifier (TA), the output of which is passed through an acousto-optic modulator (AOM) in a double-pass configuration for amplitude and frequency control before delivery to the chamber. The locking branch passes through an electro-optic modulator (EOM) for light dithering (thus avoiding modulation on experiment

light), then through an AOM for tuning. A PBS and a  $\lambda/4$  waveplate (QWP) allow routing of the back-reflected light from the vertical ULE cavity to the detector (Det). Another detector (comprised of a fast photodiode and a CCD camera) is used to monitor the transmitted light. The back-reflected signal is amplified and demodulated with a phase mixer at the local oscillator frequency of the EOM to extract a Pound-Drever-Hall error signal. The error signal is fed into a PID regulator<sup>1</sup>.

The ULE cavity and the ECDL are installed in an anti-vibration compartment capable of thermal stabilization. The latter function, however, is not implemented. To estimate the resulting drift (Fig. B.2), The  $4s^2 S_{1/2}(m_j = +1/2) \longleftrightarrow 3d^2 D_{5/2}(m_j = -3/2)$  and  $4s^2 S_{1/2}(m_j = -1/2) \longleftrightarrow 3d^2 D_{5/2}(m_j = -5/2)$  transitions are scanned consecutively over a few hours. The drift that can be attributed to magnetic field change (6(3) Hz/min) is inferred from looking at the time evolution of the difference between the two frequencies, and the drift that can be attributed to cavity thermalization ( $\sim 30(3)$  Hz/min) is inferred from the change of either frequency. This is the reason for the calibration routine described in Sec. E.3. Another important observation in this data is that the population amplitude in each manifold varies substantially with time ( $\sim 20\%$ ), which is consistent with changing Rabi time, in turn suggesting the intensity of light on the ion changes. A feedback loop is in the works to try and address that.

Despite the drift above, after a recent tune-up, the system stays locked for weeks under normal lab conditions. The locked laser linewidth is estimated at  $\sim 10 \text{ kHz}$ .

<sup>&</sup>lt;sup>1</sup>FALC 110 from Toptica.

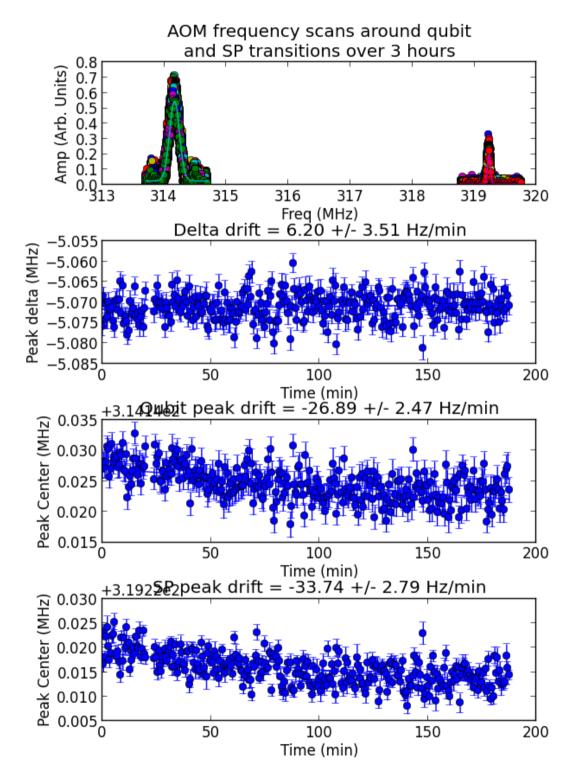


Figure B.2: 729 nm ULE cavity drift. The drift in the difference between frequencies (delta drift) can be attributed to magnetic field changes, while the drifts in the frequencies (Qubit peak and SP peak) are an indication of the ULE cavity drift.

# Appendix C

# Light Collection With Diffractive Optic Elements

The Diffractive Optic Elements (DOE) integration experiment [78] is an experiment relying on the experimental control software described here (Appendix D). With this experiment we demonstrate the potential of surface ion trapping devices for scalability as DOEs are successfully integrated under a device. The full text is included.

# Characterization of Fluorescence Collection Optics Integrated with a Microfabricated Surface Electrode Ion Trap

Craig R. Clark, <sup>1</sup> Chin-wen Chou, <sup>3</sup> A. R. Ellis, <sup>1</sup> Jeff Hunker, <sup>1</sup> Shanalyn A. Kemme, <sup>1</sup> Peter Maunz, <sup>1</sup> Boyan Tabakov, <sup>1,2</sup> Chris Tigges, <sup>1</sup> and Daniel L. Stick <sup>1,2</sup>

<sup>1</sup>Sandia National Laboratories, P.O. Box 5800, Albuquerque, New Mexico 87185-1082, USA

<sup>2</sup>Center for Quantum Information and Control, University of New Mexico, MSC 07-4220,

Albuquerque, New Mexico 87131-0001, USA

<sup>3</sup>National Institute of Standards and Technology, 325 Broadway Street, Boulder, Colorado 80305, USA

(Received 12 December 2013; published 27 March 2014)

We demonstrate and characterize a scalable optical subsystem for detecting ion qubit states in a surface electrode ion trap. An array of lithographically fabricated diffractive lenses located below the plane of the trap images ions at multiple locations, relaying the collected light out of the vacuum chamber through multimode fibers. The lenses are designed with solid angle collection efficiencies of 3.58%; with all losses included, a detection efficiency of 0.388% is measured. We measure a minimal effect of the dielectric optical substrate on the temporal variation of stray electric fields and the motional heating rate of the ion.

DOI: 10.1103/PhysRevApplied.1.024004

In recent years, there have been multiple efforts to maximize the efficiency of fluorescence collection from single ions [1-3]. Higher efficiencies lead to higher detection fidelities, shorter detection times, and increased rates of photon-mediated remote ion entanglement [4,5]. In this paper, we focus on another aspect of fluorescence collection, the ability to scale the optical system to simultaneously image multiple ions. Single optics with large fields of view can image multiple ions but sacrifice collection efficiency and are not arbitrarily scalable. Multiple optics each imaging separate locations are scalable if their individual lateral dimensions are comparable to the size of a single trapping well (the exact requirement depends on the specific architecture). In the case of microfabricated surface traps [6], this scalability requires the lateral dimensions of single optics to be smaller than ≈1 mm. To simultaneously meet this requirement and still retain a high numerical aperture (NA), the lens must be commensurately close to the ion (< 1 mm). This proximity is generally undesirable due to the physical constraints imposed on the trap electrodes, the reduction of vertical optical access, and issues due to stray charge buildup [7]. Here we describe a system combining ion traps and scalable microfabricated lenses, measure their collection performance, and show that proximity has a manageable impact by measuring the stray electric fields and motional heating rates at different positions in the trap.

Most experiments use multielement refractive lenses outside of the vacuum chamber for imaging ions. These lenses are normally 10–30 mm away from the ion, subtending only a small fraction of the  $4\pi$  solid angle (SA). Some recent experimental setups explored moving the optic inside the vacuum chamber, including a custom in-vacuum lens (4% SA subtended) [1], a spherical mirror surrounding a trap (10% SA subtended, 0.43% end-to-end detection efficiency) [2], and a microfabricated Fresnel optic with a 5-mm

diameter and 3-mm working distance (12% SA subtended, 4.2% effective collection efficiency) [3]. Each of these methods maximizes light collection for single ions in macroscale traps. Other recent experiments focused on demonstrating the size scalability of the collection optics, such as a fiber integrated with a surface electrode trap (2.1% SA subtended) [8] and a micromirror fabricated as part of a surface trap (collection enhancement factor of 1.9 over the free space imaging system) [9]. Here we demonstrate a fiber-coupled array of microfabricated diffractive optic elements (DOEs) with lenses that are slightly smaller than the trapping well size (165- $\mu$ m focal distance to the ion, 250- $\mu$ m periodicity), a proof-of-principle experiment combining scalable light collection with integrated microlenses.

The surface electrode ion trap (Fig. 1) used here is operated with a 250-V peak amplitude rf signal at a frequency of 35 MHz. Loading <sup>40</sup>Ca<sup>+</sup> is achieved by using a natural calcium source which delivered atoms through the back side of the trap (to prevent the electrodes from being coated) along with lasers for photoionization. After compensation, the resulting secular frequencies of the ion are [1.1, 5.4, 6.2] MHz. More details on the trap fabrication, characterization, and operation can be found in Ref. [10]. The mechanical integration of the collection optic with a surface ion trap is described in detail in Ref. [11].

The array of five lenses is located 165  $\mu$ m below the ion, with each 140- $\mu$ m square lens separated by a 110- $\mu$ m gold ground plane from its neighboring lens, as shown in Fig. 1(a). Each lens is aligned to a multimode fiber with a ceramic ferrule, fixing the lens array's optical axis to the optical axis of the fiber [Fig. 1(b)]. The fiber is connected to a UHV feedthrough for delivering the coupled light outside of the chamber.

UV light in proximity to exposed dielectric surfaces can lead to charge buildup, which is dissipated slowly relative

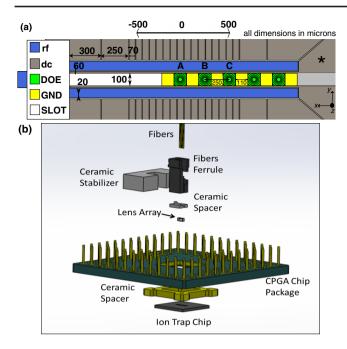


FIG. 1. (a) Plan view of the trap and optics with all dimensions shown in microns [10]. Green squares are the DOEs, gold squares are the gold ground planes between each DOE, and the white region is a slot in the trap for loading ions from the back. The electrode labeled with an  $\ast$  is used to shift the ion in the y direction. (b) Assembly drawing (exploded view) of the optics integrated with the trap chip [11].

to the experiment time. Oxides or contaminants on the trap electrodes can also become charged and generate electric fields at the ion, leading to excess micromotion, which negatively impacts Doppler cooling, light collection, and the motional heating rate of the ion [12–14]. Although the ion is in a direct line of sight with the DOEs, it is significantly shielded by the surrounding electrodes and the grounded gold coating in the space between each DOE, as shown in Fig. 1. Considering this interplay between the different system components, we characterize three properties of the combined trap-optic system: the difference in stray electric fields above and away from the exposed dielectric of the DOE, the motional heating rate difference above and away from the DOE, and the light collection properties of the DOE.

Excess micromotion occurs when the ion is not positioned at the rf null, due to out-of-phase rf signals on different electrodes, an imperfect static trapping solution, or a stray electric field. The first issue can be practically eliminated by capacitively shunting the static control electrodes [10], while the latter two can be eliminated with a static offset applied to the electrodes, provided the stray field does not change on a fast time scale [15]. The stray electric fields are eliminated at multiple locations by employing an adaptive algorithm with iterative measurements of the micromotion along the two transverse axes [15–17]. Combining these techniques allows us to

compensate stray fields down to several V/m. After this procedure, the applied voltage solution is compared to boundary element simulations of the trap to estimate the stray field in both the y and z directions.

Figure 2 shows measured stray fields in the y and z directions (radial to the rf confining potential) using an automated compensation procedure, compared at locations away from and above the DOEs. Stray field measurements are taken at a coarse spacing of 77  $\mu$ m over a total range of  $\pm 500 \ \mu$ m from the center of the x axis of the trap, along with higher-resolution measurements at a 5- $\mu$ m spacing between optics B and C (Fig. 1).

Figure 2(a) shows a steady increase in the applied field needed to position the ion at the rf null in both the y and z directions, corresponding to the ion's position relative to the DOEs. This increase is primarily due to a modification of the trapping potential by the DOE assembly, as compared to above the open slot at  $-300 \ \mu m$ . When measured above the slot, the stray field  $E_z$  is the same order of

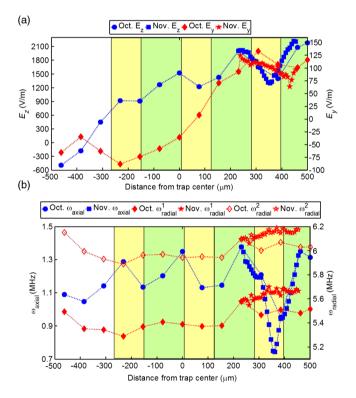


FIG. 2. (a) Stray field measurements of  $E_z$  (blue) and  $E_y$  (red). The measurement error is 13 V/m in  $E_z$  and 3 V/m in  $E_y$ . (b) Secular frequency data taken along the z axis of the trap after performing the compensation procedure. (blue) Axial frequency measurements have errors below 1 kHz, and (red) radial frequency measurements have errors less than 10 kHz. Coarse data are taken at 77- $\mu$ m steps (blue circles and red diamonds); higher-resolution data (blue squares and red stars) are taken a month later between the center of two DOEs at a step size of 5  $\mu$ m. The background color of the figure corresponds to the different regions of the trap: (white) the loading slot, (gold) ground plane, and (green) DOE. All lines are to guide the eye.

magnitude as  $E_{\nu}$ , but, as the ion moves above the DOE assembly,  $E_7$  dramatically increases. At positions 0, 250, and 500  $\mu$ m, there are local maxima in  $E_z$  of 1500, 2000, and 2200 V/m, which correspond to trapping positions directly above the center of optics A, B, and C, respectively. The local maximum at the position  $-220 \mu m$  corresponds to the edge of the optics mount where the gold ground plane was accidently chipped off during assembly, exposing the dielectric. The local minimum in  $E_z$  of 1300 V/m at 350  $\mu$ m corresponds to storing the ion directly above the goldcoated ground plane between B and C. The secular frequencies show a similar trend due to the stray field. The axial frequency has a local maximum and local minimum corresponding to positions above the DOE and ground plane, respectively. Figure 2(b) also shows the radial frequencies at each location; their fractional change is less significant than that of the axial frequencies and does not exhibit the same spatial modulation. The increase in radial frequency shown on the high-resolution data is ascribed to changes in the helical resonator over the month in which data were taken.

To determine the impact of the DOEs on the temporal stability of the stray electric field, the automated compensation procedure is continuously performed over several hours at locations away from  $(-385 \mu m)$  and above DOE-C (500  $\mu$ m). Excluding the 15 min following loading,  $E_v$  and  $E_z$  change less than 2.5 V/m over the following 5 h (below the measurement resolution), while the secular frequencies change less than 1 and 10 kHz in the axial and radial directions, respectively. The loading process results in additional stray fields of  $\Delta E_z \approx \pm 25 \text{ V/m}$  and  $\Delta E_{\rm v} \approx \pm 15 \text{ V/m}$  at both locations. Over 5 h, the axial and radial frequencies change less than 2 and 50 kHz, respectively, including the effects of loading. This result would be compatible with high-fidelity two-qubit gates using axial modes of motion ( $\delta f/f < 0.2\%$ ). The greater variability in the radial frequency is ascribed to drift in the resonance frequency of the rf resonator.

A well-known issue with ion traps is the motional heating due to electric field fluctuations on the electrodes [12]. This issue is particularly problematic in traps that confine ions close to trap electrodes (80  $\mu$ m in the current work). The experiments described here employ the Doppler recooling technique [18] to measure and compare heating rates in the slotted region of the trap and above DOE-C. One set of measurements is taken by using National Instruments voltage sources and vields similar rates above the slot and optic (32 and 42 quanta/ms, respectively). A measurement with a battery voltage supply in the slotted region yields a heating rate of 11 quanta/ms (this method does not allow shuttling an ion to other locations). While these measurements show that the heating rate is comparable near the optic, it should be noted that the overall heating rate of the trap must be reduced to be compatible with highfidelity two-qubit gates.

The detection efficiency (DE) of each optical system is determined by using a single-photon counting technique [1,2] in which a single photon is emitted with very high probability per experimental sequence. This technique is advantageous, because it does not require calibrating all of the relevant experimental conditions (intensity and detunings of lasers, magnetic field, motional state of ion, etc.) and fitting the calcium atomic spectra to an eight-level optical Bloch equation. The DE values reported in this paper include all system losses, from the solid angle collection to the quantum efficiency of the photomultiplier tube (PMT). The ion is cooled for 2  $\mu$ s with both lasers, 397 and 866 nm [Fig. 3(a)]. Then it is exposed to a 397-nm laser for 1.5  $\mu$ s to optically pump to the  $D_{3/2}$  state (lifetime = 1 s). A 1.5- $\mu$ s delay is inserted to ensure the previous laser is fully extinguished. Then the 866-nm laser is turned on to pump to the  $P_{1/2}$  state, which decays and generates a single 397-nm photon [Fig. 3(b)]. This sequence is repeated 10<sup>6</sup> times for statistics.

Figure 3(c) is a schematic of both the Standard Imaging (SI) system and the DOE collection setup, along with the transmittance of each optical component. Our standard imaging system includes a grounded mesh to mitigate charge buildup on the reentrant view port. The imaging optic is a UV objective with NA = 0.29 (effective solid angle collection of 1.9%); when combining the view port and optic, the effective solid angle collection is 1.34%. Additional but small losses occur at a UV-coated mirror and filter. Finally, a PMT (Hamamastu H10682-210) is used for photon counting. Considering all these losses, a DE of 0.34% is expected, matching the measured value of  $DE_{SI} = 0.341(6)\%$ .

In designing the DOE lens system, the most important metrics are the solid angle collection efficiency and diffraction efficiency. The solid angle collection efficiency of the lens system reported here is calculated to be 3.58%

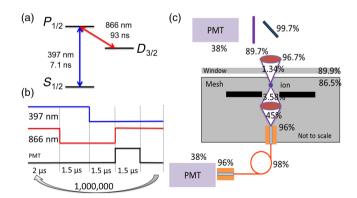


FIG. 3. (a) Ca<sup>+</sup> energy diagram showing the relevant laser transitions. (b) Single-photon generation pulse sequence. (c) Schematic of the standard imaging system and DOE collection system (not to scale). All percentages correspond to the transmittance or reflectivity at 397 nm. The product of each stage results in a total DE of a trapped fluorescing Ca<sup>+</sup> ion.

(this value accounts for the square shape of the lens). Two on-axis lenses are used to image each location in the linear array, as described in Ref. [11]. A standard knife-edge test is used to measure the diffraction efficiency, i.e., the fraction of light transmitted by the lens system into the desired transmitted  $\pm 1$ st order. The range of diffraction efficiencies of 15 fabricated and measured two-lens elements (in series) is 44%–49%, while the integrated lens has an efficiency of 45% and a measured focal distance of 168  $\mu$ m. The collected light is coupled to a multimode optical fiber (Polymicro's FVP100110125) in which 4% loss is expected at the input and output facets and 2% absorptive loss occurs in the fiber. By using the same PMT as above, a DE<sub>DOE</sub> of 0.55% is predicted.

Figure 4(a) is an image of the ion after stray electric fields are canceled, along with 397-nm light backilluminating the DOE through the multimode fiber. It shows that the compensated ion is not at the focus of the DOE but is translated in the y direction by almost 20  $\mu$ m. This conclusion is confirmed after removing the trap from the vacuum chamber and measuring an 18(2)- $\mu$ m translation, which likely occurred during the bake of the chamber. The height of the focus is *in situ* measured to be at the height of the ion. The backillumination size is larger than the focal spot size of the lens due to the core size of the multimode fiber. For more details on the preinstallation alignment procedure, see Ref. [11].

Additional voltage is applied to the dc control electrodes to shift the ion towards the optic by  $\approx 7 \mu m$ , as shown in Fig. 4(b). This voltage induced a significant amount of

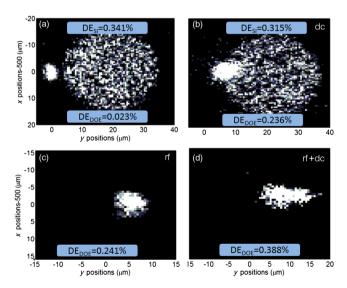


FIG. 4. (a) Image of the compensated ion with corresponding  $DE_{SI}$  and  $DE_{DOE}$ . (b) Image after applying voltage to the dc electrodes to shift the ion. The large circles in both cases correspond to 397-nm light backilluminating the optic through the fiber. (c) Image after applying rf voltage to the center dc electrode indicated by the star in Fig. 1. (d) Ion after applying both an rf shift and a dc shift of the ion. The smearing of the ion is due to the micromotion.

micromotion, but the single-photon counting method is relatively (though not completely) insensitive to micromotion. To quantify the effect, the  $DE_{SI}$  is remeasured to be 0.315% corresponding to a drop of 7.6% in the signal compared to the compensated  $DE_{SI}$ . Shifting the ion towards the center of the optic increases  $DE_{DOE}$  to 0.236 (5)%, compared to 0.023(2)% when compensated. This result is still significantly lower than the theoretical value of 0.51% (which includes the fractional reduction due to micromotion).

It is possible to improve  $DE_{DOE}$  further by applying an additional rf voltage to one of the center dc electrodes (indicated in Fig. 1 with an \*). By reducing the rf amplitude ( $V_{\rm rf}=80~{\rm V}$ ) and applying a phase-locked signal to a center electrode, the rf null shifts toward the center of the DOE. Figure 4(c) shows the shift while applying  $10V_{\rm rf}$  of phase-locked rf, resulting in an ion displacement of 8  $\mu$ m and a  $DE_{\rm DOE}$  of 0.241(5)%. Figure 4(d) shows the ion displaced by 10– $12~\mu$ m when both rf and dc fields are used. In this case,  $DE_{\rm DOE}=0.388(6)\%$ , less than the expected DE of 0.51% due to the remaining imperfect overlap of the ion with the DOE focus.

In conclusion, we demonstrate an integrated array of DOEs with a surface electrode ion trap, coupling fluorescence from a trapped Ca<sup>+</sup> ion into a multimode fiber under ultrahigh vacuum conditions and successfully transmitting the light out of the vacuum chamber to a PMT. Stray electric fields are compensated over the optic and remain stable over the course of weeks, and the DOE does not noticeably affect the motional heating rate of the ion. Using a single-photon counting technique, we measured an overall DE for the DOE of 0.388%. These optics could be arrayed in a scalable fashion and would allow for detection times < 200  $\mu$ s of Ca<sup>+</sup> with infidelities <  $10^{-4}$  [19]. We show in this paper that their presence does not create stray field drifts that would preclude high-fidelity two-qubit gates and that the heating rate is not noticeably worse near the optic.

We acknowledge and thank Robert Boye for many helpful discussions and M. G. Blain, Joel Wendt, Sally Samora, and the entire fabrication team for providing us with the trap and optics. We also thank Greg Brady for the optical design. This work was supported by the Intelligence Advanced Research Projects Activity (IARPA). Sandia National Laboratories is a multiprogram laboratory managed and operated by Sandia Corporation, a wholly owned subsidiary of Lockheed Martin Corporation, for the U.S. Department of Energy's National Nuclear Security Administration under Contract No. DE-AC04-94AL85000.

<sup>[1]</sup> M. Almendros, J. Huwer, N. Piro, F. Rohde, C. Schuck, M. Hennrich, F. Dubin, and J. Eschner, Bandwidth-tunable single-photon source in an ion-trap quantum network, Phys. Rev. Lett. 103, 213601 (2009).

- [2] G. Shu, N. Kurz, M. R. Dietrich, and B. B. Blinov, Efficient fluorescence collection from trapped ions with an integrated sherical mirror, Phys. Rev. A 81, 042321 (2010).
- [3] Erik W. Streed, Benjamin G. Norton, Andreas Jechow, Till J. Weinhold, and David Kielpinski, Imaging of trapped ions with a microfabricated optic for quantum information processing, Phys. Rev. Lett. **106**, 010502 (2011).
- [4] P. Maunz, S. Olmschenk, D. Hayes, D. N. Matsukevich, L-M. Duan, and C. Monroe, Heralded quantum gate between remote quantum memories, Phys. Rev. Lett. 102, 250502 (2009).
- [5] R. Noek, G. Vrijsen, D. Gaultney, E. Mount, T. Kim, P. Maunz, and J. Kim, High speed high fidelity detection of an atomic hyperfine qubit, Opt. Lett. 38, 4735 (2013).
- [6] J. Chiaverini, R. B. Blakestad, J. Britton, J. D. Jost, C. Langer, D. Leibfried, R. Ozeri, and D. J. Wineland, Surface-electrode architecture for ion-trap quantum information processing, Quantum Inf. Comput. 5, 419 (2005).
- [7] M. Harlander, M. Brownnutt, H. Hänsel, and R. Blatt, Trapped-ion proding of light-induced charging effects on dielectrics, New J. Phys. 12, 093035 (2010).
- [8] A. P. VanDevender, Y. Colombe, J. Amini, D. Leibfried, and D. J. Wineland, Efficient fiber optics detection of trapped ion fluorescence, Phys. Rev. Lett. 105, 023001 (2010).
- [9] J. True Merrill, Curtis Volin, David Landgren, Jason M. Amini, Kenneth Wrigth, S. Charles Doret, C-S. Pai, Harley Hayden, Tyler Killian, Daniel Faircloth, Kenneth R. Brown, Alexa W. Harter, and Richart E. Slusher, Demonstration of integrated microscale optics in surface-electrode ion trap, New J. Phys. 13, 103005 (2011).
- [10] D. T. C. Alllcock, T. P. Harty, H. A. Janacek, N. M. Linke, C. J. Ballance, A. M. Steane, D. M. Lucus, R. L. Jarecki, Jr., S. D. Habermehl, M. G. Blain, D. Stick, and D. L. Moehring, Heating rate and electrode charging measurements in a scalable, microfabricated, surface-electrode ion trap, Appl. Phys. B 107, 913 (2012).
- [11] G. R. Brady, A. R. Ellis, D. L. Moehring, D. Stick, C. Highstrete, K. M. Fortier, M. G. Blain, R. A. Haltli, A. A. Cruz-Cabrera, R. D. Briggs, J. R. Wendt, T. R. Carter,

- S. Samora, and S. A. Kemme, Integration of fluorescence collection optics with a microfabricated surface electrode ion trap, Appl. Phys. B **103**, 801 (2011).
- [12] D. A. Hite, Y. Colombe, A. C. Wilson, K. R. Brown, U. Warring, R. Jördens, J. D. Jost, K. S. McKay, D. P. Pappas, D. Leibfried, and D. J. Wineland, 100-fold reduction of electric-field noise in an ion trap cleaned with in situ argonion-beam bombardment, Phys. Rev. Lett. 109, 103001 (2012).
- [13] S. Charles Doret, Jason M. Amini, Kenneth Wright, Curtis Volin, Tyler Killian, Arkadas Ozakin, Douglas Denison, Harley Hayden, C.-S. Pai, Richart E. Slusher, and Alexa W. Harter, Controlling trapping potentials and stray electric fields in a microfabricated ion trap through design and compensation, New J. Phys. 14, 073012 (2012).
- [14] A. Safavi-Naini, E. Kim, P. F. Weck, P. Rabl, and H. R. Sadeghpour, Influence of monolayer contamination on electric-field-noise heating in ion traps, Phys. Rev. A 87, 023421 (2013).
- [15] D. J. Berkeland, J. D. Miller, J. C. Bergquist, W. M. Itano, and D. J. Wineland, Minimization of ion micromotion in a paul trap, J. Appl. Phys. **83**, 5025 (1998).
- [16] Y. Ibaraki, U. Tanaka, and S. Urabe, Detection of parametric resonance of trapped ions for micromotion compensation, Appl. Phys. B 105, 219 (2011).
- [17] S. Narayanan, N. Daniilidis, S. A. Möller, R. Clark, F. Ziesel, K. Singer, F. Schmidt-Kaler, and H. Häffner, Electric field compensation and sensing with a single ion in a planar trap, J. Appl. Phys. 110, 114909 (2011).
- [18] R. J. Epstein, S. Seidelin, D. Leibfried, J. H. Wesenberg, J. J. Bollinger, J. M. Amini, R. B. Blakestad, J. Britton, J. P. Home, W. M. Itano, J. D. Jost, E. Knill, C. Langer, R. Ozeri, N. Shiga, and D. J. Wineland, Simplified motional heating rate measurements of trapped ions, Phys. Rev. A 76, 033411 (2007).
- [19] A. H. Myerson, D. J. Szwer, S. C. Webster, D. T. C. Allcock, M. J. Curtis, G. Imreh, J. A. Sherman, D. N. Stacey, A. M. Steane, and D. M. Lucas, High-fidelity readout of trappedion qubits, Phys. Rev. Lett. 100, 200502 (2008).

# Appendix D

# **Experiment Control Software**

It is difficult to emphasize enough the need for a comprehensive experimental control package, designed with ion trapping and quantum optics in mind. The sequences of actions that take place for most ion manipulation tasks are time sensitive, and can consist of millions of conditional events. The experimental control package enabling the ring trap (Chapter 5) and Diffractive Optics (Appendix C) experiments featured:

- control over instruments: optical and rf power meters, oscilloscopes, function generators, power supplies, and a direct digital synthesizer (DDS);
- control voltage generation (Appendix D.2) via an NI chassis and cards (Sec. 3.4);
- control over rf voltage amplitude and frequency (through DDS or function generator control);
- photon counting through the NI cards (Sec. 3.4);
- turning on and off the PI light and atomic oven through the NI cards (Sec. 3.4);
- ion imaging (Sec. 3.6) via controlling the motors on the Doppler beam and imaging stack, and through camera control (Appendix D.3);

- laser locking (Appendix D.1);
- data collection and data analysis;
- procedural (programmatic) and interactive (GUI-based) control allowing a high level of abstraction and automation.

The paradigm followed when developing the code emphasized procedural automation. "Drivers" (in fact custom Python wrappers for libraries) handled details in instrument or equipment communication. The drivers were used by higher level modules that provided specific functionality (e.g. scan a parameter in one instrument while reading out another, deliver a sequence of control voltages, move the camera, etc.). These higher level modules were used in algorithms to implement an experiment (e.g. load an ion, move it to some location, minimize micromotion there, get another ion if the ion gets lost during the measurements, etc.). Since this procedural approach is not always desirable, the modules were equipped with graphical use interfaces (GUIs) for interactive control. Finally, the GUIs could be lumped (without the need for extensive programming experience) to provide a tailored experimental control application, allowing automation from the GUI. The code, some highlights of which are below, was written from scratch exclusively in Python and PyQt to specifically address rapid development and transparency. The code replaced a proprietary solution (proprietary source) that could not be upgraded with the needed features.

Some of the functionality in the list above and much more is currently handled by a field programmable gate array(FPGA) – Python – PyQt hybrid package (Appendix D.4) under development by Peter Maunz. In this work, the hybrid package was used for secular frequency and heating rate measurements in the ring trap experiment and was the main tool used for the plasma treatment experiment.

#### D.1 Laser Locks

The function of the code, written mostly in C++ (with Qt), was to lock a number of lasers to an atomic reference. To do anything beyond trapping ions, light frequencies must be well known and controlled. For that purpose, a high resolution wavemeter<sup>1</sup> was locked to an available rubidium atomic reference (Sec. A). An optical switch that takes multiple wavelengths, one per switch channel, stepped through the channels and provided the wavemeter input. For each channel, a software feedback loop was implemented. In the loop, a corrective voltage, to be applied to the laser diode grating piezo, was calculated from the difference between the target and measured frequencies. The voltage was output by a multi-channel DAC card in the computer that run the wavemeter software and lock loops. The refresh rate of the loop (implemented as a P-I loop) depended on the number of channels followed and the illumination / optical power per channel. The net result of this locking scheme was that light entering the multiple switch channels was referenced to the atomic reference through the wavemeter. The instantaneous deviation from the absolute target frequency for light fed into the optical switch could be as good as a few MHz, making the lock useful to control light for which an excursion of a few MHz is not an issue (repumpers, PI light).

## D.2 Control Voltages

The low level control over voltage generation (Sec. 3.4) was implemented with Python wrappers around manufacturer provided libraries (NI DAQ). The code

• provided mapping from physical channels to labels meaningful for the user (e.g. "electrode e01");

<sup>&</sup>lt;sup>1</sup>HighFinesse/Ångstrom WSU 10.

- allowed real time scaling of voltages (e.g. to modify the axial potential while imaging an ion);
- provided for real time application of arbitrary voltages without the need for preparation (e.g. to check electrode connectivity by applying a voltage to the electrode while imaging an ion);
- provided for real time scaling of pre-defined named sets (e.g. to increase the electric field in a given direction without the need to handle the electrodes individually).
- provided control over sequences of voltage applications (e.g. for ion shuttling or axial field measurements);
- was synchronized with cooling/imaging (Appendix D.3) to make the motion on a ring intuitive and convenient for a user (e.g. move an ion to a location using the shortest path);
- allowed procedural control over all of the above for algorithm implementation,
   making it an essential tool.

## D.3 Cooling and Imaging

As with voltage control, low level control was implemented with Python wrappers. The code

- controlled image acquisition from a CCD camera<sup>2</sup>;
- controlled the location of the objective of the imaging stack (Appendix 3.6);
- controlled the path of the measurement Doppler beam;

<sup>&</sup>lt;sup>2</sup>Andor Luca R.

• the above was synchronized with voltage control to allow, for example, ion shuttling while efficiently cooling and imaging without user interaction.

Layout features of the trap were used to calibrate the motors and imaging system.

#### D.4 Successor

The control system developed by Peter Maunz followed a different paradigm, favoring user interaction over automation. An essential hardware difference is the inclusion of an FPGA<sup>3</sup> controlling a number of two channel DDS boards, thus eliminating the need to control all but specialized instruments (e.g. power supplies, power meters). The FPGA control is wrapped in PyQt, along with a meta-language to implement FPGA algorithms, data visualization and analysis tools, external instrument control and acquisition interface, voltage control interface, and lately, automation interface. While development continues, even in its current state the package is a superior and indispensable tool for ion trapping/atomic physics experiments.

### D.5 Cost Estimate

Plenty of code, mostly in C++, Python, and Mathematica language, was generated in order to make much of this work possible, amounting to perhaps a calendar year of research time. The final versions of the code exceed the printed volume of this dissertation several times. To quantify the coding effort and put it in perspective, an excerpt from a report with a time and cost estimate follows, based on Source Lines of Code (SLOC) and widely accepted business models, for the Python portion of the code used for control of the ring trap (Chapter 5) and Diffractive Optics

<sup>&</sup>lt;sup>3</sup>Opal Kelly XEM6010.

(Appendix C) experiments. The report, generated using David A. Wheeler's 'SLOC-Count' [157], excludes the currently used software (Appendix D.4) that is exclusively the effort of Peter Maunz, or any code related to device modeling.

. . .

Computing results.

```
SLOC Directory SLOC-by-Language (Sorted)
```

5832	ex_control	python=5832
5447	not_active	python=5447
3254	top_dir	python=3254
218	gui_elements	python=218

Totals grouped by language (dominant language first): python: 14751 (100.00%)

```
Total Physical Source Lines of Code (SLOC) = 14,751

Development Effort Estimate, Person-Years (Person-Months) = 3.38 (40.50)

(Basic COCOMO model, Person-Months = 2.4 * (KSLOC**1.05))

Schedule Estimate, Years (Months) = 0.85 (10.20)

(Basic COCOMO model, Months = 2.5 * (person-months**0.38))

Estimated Average Number of Developers (Effort/Schedule) = 3.97

Total Estimated Cost to Develop = $ 455,936
```

(average salary = \$56,286/year, overhead = 2.40).

. . .

# Appendix E

# Procedures and Algorithms

This research resulted in and adhered to a number of procedures that increased repeatability and allowed easier troubleshooting. The procedures below were taken out of the main text body to improve readability.

## E.1 Preparation of UHV Components

When common new manifold components<sup>1</sup> are acquired, unless specified by the manufacturer to be UHV – rate clean, they are prepared for use as follows:

- 1. Visual inspection for irregularities and any damage to the knife-edge. A scratch along the knife edge or a notch (Fig. E.1) decreases the likelihood of a good seal.
- 2. (Optional) Ultrasonic cleaning in detergent solution to break and release any gross particulate contaminants.
- 3. Ultrasonic/megasonic cleaning in high purity acetone to break oils.

<sup>&</sup>lt;sup>1</sup>Obtainable from Varian, Lesker, MDC, Accu-Glass.



Figure E.1: Knife-edge damage on a custom ordered, unused CF component.

- 4. Ultrasonic/megasonic cleaning in high purity alcohol to break acetone residue. Optionally this step can be subdivided into cleaning with a heavy alcohol (e.g. isopropyl) followed by cleaning with a lighter alcohol (e.g. methyl).
- 5. Drying, preferably in a controlled environment. A dust particle that finds its way into the chamber is a source of outgassing and can be moved by turbulent currents in the initial stage of pumping onto the trapping device, rendering it inoperable.
- 6. Visual inspection immediately preceding assembly.
- 7. (Optional) Bakeout while being pumped on or in air or in an  ${\rm H}_2$  atmosphere.

## E.2 Bakeout of UHV Vessels

The pumpdown/bakeout procedure that was developed is the following:

1. Once the vessel is in the oven, verify that the ion gauge, titanium sublimation pump, and atomic oven filaments are intact by measuring the resistance across

nominally connected pins ( $\sim 1~\Omega$ ). Filaments become brittle with use and may break during chamber transportation. Verify that the ion pump is not shorted by measuring resistance between terminals  $> 500~\mathrm{M}\Omega$  (or whatever is the instrument limit). Collected residue inside the pump may be dislodged during transportation, possibly shorting elements. Connect bakeable cables to the ion gauge and ion pump.

- 2. Verify that the trapping device is likely intact by measuring rf ground resistance<sup>2</sup> > 500 M $\Omega$  and capacitance<sup>3</sup> ~ 15 pF, depending on the specific device.
- 3. Verify that all bolts on joints are tightened.
- 4. If a "particle-free" [158] pump-down is needed, verify that the pumping path through the limiting orifice is chosen.
- 5. Start TMP.
- 6. When in molecular flow regime (expected below 0.1 Torr in this setup), change the pumping path to bypass the limiting orifice, thus increasing the pumping speed.
- 7. When pressure is below 10<sup>-5</sup> Torr, degas the atomic oven by running current through the filament (Sec. 3.5.1). Degassing trades slow outgassing for relatively short burst of pressure increase, and heat and particulate contamination generation. The resulting outgassed material is pumped out over the bake period, rather than occurring at the end and contaminating a low pressure chamber.
- 8. When the pressure is below  $10^{-5}$  Torr, degas the TSP filaments. This increases the pressure substantially at first.

<sup>&</sup>lt;sup>2</sup>Fluke 289 multimeter.

<sup>&</sup>lt;sup>3</sup>GwIntek LCR 819 Meter.

- 9. When the pressure is below 10<sup>-6</sup> Torr, use an RGA with the electron multiplier on and He<sub>2</sub> to test the chamber for leaks. He<sub>2</sub> gas is not present in the atmosphere as it is too light, hence it should not be in the chamber. Because the molecule is also very small and permeable, leaks are found when He<sub>2</sub> is detected by observing an increase in the partial pressure when spraying minute amounts of gas into joints, feedthroughs, and viewports. If leaks are found, it is sometimes possible to repair them without venting the vessel to atmosphere. A vacuum tight chamber is considered one in which He<sub>2</sub> is not detected above the background/instrument noise level, at about 10<sup>-13</sup> to 10<sup>-12</sup> Torr partial pressure. Running the RGA filaments increases the pressure slightly.
- 10. (Optional.) When the pressure is below  $10^{-7}$  Torr, the ion gauge is degassed. This increases the pressure temporarily.
- 11. Ramp up to the target bakeout temperature. A rule of thumb is that the final pressure falls an order of magnitude for each 100 K of bakeout temperature increase. Again, this is limited by the materials in the assembly. For bakeouts above the Curie temperature of the ion pump magnets, they must be removed to avoid demagnetization. An absolute limit for torqued CF flanges is considered  $\sim 450$  °C, beyond which the austenitic steel properties change and knife edge damage results.
- 12. At target temperature, once pumping speed becomes insignificant (e.g. < 10 % decrease in ion pump current or gauge readings per day) or some predetermined fraction of the thermal budget is reached, the bakeable valve on the vessel separating it from the external pumping manifold should be closed hand tight. The vessel ion pump and ion gauge are then turned on.
- 13. Once the pumping speed becomes insignificant or the thermal budget is reached, the oven temperature is ramped down.
- 14. When the vessel is at ambient temperature, the bakeable valve is torqued

- closed. External pumps (e.g. TMP) are stopped. If there is an increase in the vessel pressure, the valve torque is increased.
- 15. Once readings equilibrate and there is no pressure increase in the vessel, the ion gauge is turned off to cool before transporting the chamber to the optical table.

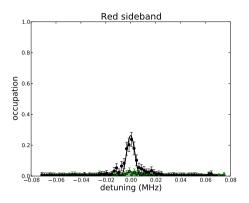
## E.3 Heating Rate Measurement Procedure

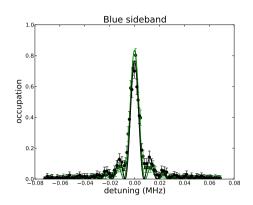
The heating rate measurement procedure relies on the processes described in Sec. 3.6 and Sec. 3.5.2. All measurements are made on the axial motional mode. The specific top level algorithm used is:

- 1. The frequency of the light on the  $4s^2 S_{1/2} \longleftrightarrow 4p^2 P_{1/2}$  transition is scanned at saturation power. The frequency and linewidth at resonance are obtained from a fit.
- 2. The previous step is repeated with optical power well below saturation.
- 3. A parametric resonance scan is performed and fit to extract one radial frequency a means to assess an undesired change in rf coupling strength.
- 4. The frequency of the light on the  $4s^2 S_{1/2}(m_j = +1/2) \longleftrightarrow 3d^2 D_{5/2}(m_j = -3/2)$  transition is scanned and fit to determine the resonance frequency.
- 5. The Rabi time of the  $4s^2 S_{1/2}(m_j = +1/2) \longleftrightarrow 3d^2 D_{5/2}(m_j = -3/2)$  transition is determined. The frequency and Rabi time are used to prepare the ion in the  $4s^2 S_{1/2}(m_j = -1/2)$  state via spin polarization (Sec. 3.6.2).
- 6. The frequency of the light on the  $4s^2 S_{1/2}(m_j = -1/2) \longleftrightarrow 3d^2 D_{5/2}(m_j = -5/2)$  first blue sideband is scanned and fit to determine resonance.

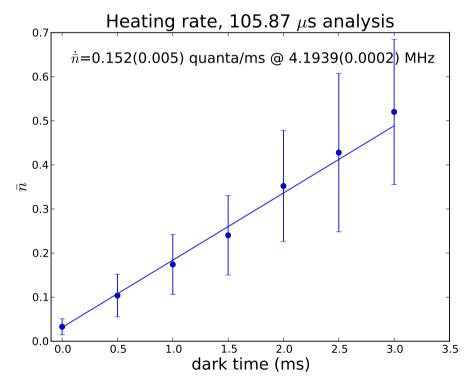
- 7. The time to incur a population inversion in the  $4s^2 S_{1/2}(m_j = -1/2) \longleftrightarrow 3d^2 D_{5/2}(m_j = -5/2)$  first blue sideband is estimated.
- 8. The frequency of the light on the  $4s^2 S_{1/2}(m_j = -1/2) \longleftrightarrow 3d^2 D_{5/2}(m_j = -5/2)$  first red sideband is scanned and fit to determine resonance frequency.
- 9. The time to incur a population inversion in the  $4s^2 S_{1/2}(m_j = -1/2) \longleftrightarrow 3d^2 D_{5/2}(m_j = -5/2)$  first red sideband is estimated.
- 10. The time to incur a population inversion in the  $4s^2 S_{1/2}(m_j = -1/2) \longleftrightarrow 3d^2 D_{5/2}(m_j = -5/2)$  first blue sideband, after sideband cooling close to the ground state, is estimated. This is the analysis time used for measuring the populations in the first sidebands.
- 11. The frequency of the light on the  $4s^2 S_{1/2}(m_j = +1/2) \longleftrightarrow 3d^2 D_{5/2}(m_j = -3/2)$  transition is scanned and fit to determine resonance.
- 12. The frequency of the light on the  $4s^2 S_{1/2}(m_j = -1/2) \longleftrightarrow 3d^2 D_{5/2}(m_j = -5/2)$  first red and blue sidebands is scanned and fit to determine the populations in the sidebands. The populations ratio is used to determine  $\bar{n}$  (Sec. 2.2.2).
- 13. The last two steps are repeated with different embedded delays in the last step between cooling to the ground state and measuring the population in the sidebands, and the resulting (delay time,  $\bar{n}$ ) pairs are fit to extract  $\dot{\bar{n}}$ .

The first 10 calibration steps determine the running parameters without the need to measure the axial secular frequency via rf excitation. 200 to 400 experiments are used per data point, depending on what makes sense for the parameter that needs to be extracted (e.g., the statistical frequency error does not substantially decrease with doubling the number of experiments, however, the experimental time needed doubles, so measurements become susceptible to effects that may not be linear in time and may artificially broaden the features, and as an end result, information





- (a) First red sideband population upon cooling to the ground state (green) and after the maximum delay time shown in (c) (black).
- (b) First blue sideband population upon cooling to the ground state (green) and after the maximum delay time shown in (c) (black).



(c) Heating rate inferred from  $\bar{n}$  after some delay.

Figure E.2: Heating rate calculation. The reason the plot is atypical is that the error bars in fact follow the theoretical model, and the data points are indeed close to the line. Typical data are more scattered.

about the frequency is lost). To account for the drift in the 729 nm light cavity (Appendix B), step 11 is inserted before each population measurement in step 12. The results of a non-typical but instructive run of the outlined algorithm are shown in Fig. E.2. Before addressing the details of the algorithms in selected steps, there is the question of what model is used to fit the data in step 12, and what error to assign each data point. In the literature, in some instances Lorentzians or Gaussians are used to extract the population in a sideband – both of which are models that do not represent the data. The approach taken here reflects a different model:

$$A(x) = a \frac{R \sin^2 \left(\frac{t}{2} \sqrt{R^2 + (2\pi(x-p))^2}\right)}{R^2 + (2\pi(x-p))^2} + b,$$
(E.1)

where b is an offset, a is the amplitude, t is the analysis time, p is the sideband frequency, and R is the "Rabi rate" of the sideband transition. The error in each data point is estimated from the distribution of the values of all (e.g. 400) experiments via a Wilson score interval calculation with continuity correction, after which the error is propagated with calculus of variations rules. Sadly, there is also the question of what software is being used to handle the calculations. Different (but usually within error) results were obtained from manipulating the data with two commercial packages, as well as with open source software. The results quoted here are obtained with the following:

```
Python 2.7.3 (default, Aug 9 2012, 17:23:57)

[GCC 4.7.1 20120720 (Red Hat 4.7.1-5)] on linux2

Type "help", "copyright", "credits" or "license" for more information.

>>> import numpy

>>> numpy.version.version

'1.7.1'
```

All steps scanning a  $4s^2 S_{1/2} \longleftrightarrow 3d^2 D_{5/2}$  transition are based on the following sub-algorithm, executed for each of the experiments in a data point.

- 1. Turn on far red detuned 397 nm light at saturation power along with the repumper beams.
- 2. Check that an ion is trapped by verifying that fluorescence threshold within a pre-determined time window is met. If not, repeat until a prescribed limit is reached and stop.
- 3. If an ion is present, reduce the 397 nm light power well below saturation and change the detuning to  $\sim -\gamma/2$ .
- 4. Wait long enough to leave the ion at  $T_D$ .
- 5. Prepare the ion in the  $4s^2 S_{1/2}(m_j = -1/2)$  state.
- 6. Cool the ion to the motional ground state.
- 7. Insert a delay. All light is off.
- 8. Apply the analysis pulse. Only the 729 nm light is on.
- 9. Detect the state by verifying that the fluorescence threshold within a time window is met. 397 nm light is at saturation power and the repumper beams are on. If the ion is not in the  $4s^2 S_{1/2}$  state, a fluorescence threshold within a time window will not be met.

The sub-sub-algorithms in steps 5 and 6 are explained in Sec. 3.6.2.

# **Bibliography**

- [1] Häffner, H. et al. Physics Reports 469.4 (2008), pp. 155-203. ISSN: 0370-1573. URL: http://www.sciencedirect.com/science/article/pii/ S0370157308003463.
- [2] Deutsch, D. Proceedings of the Royal Society of London A: Mathematical, Physical and Engineering Sciences 425.1868 (1989), pp. 73–90. ISSN: 0080-4630. DOI: 10.1098/rspa.1989.0099.
- [3] Shor, P. "Algorithms for quantum computation: discrete logarithms and factoring". Foundations of Computer Science, 1994 Proceedings., 35th Annual Symposium on. Nov. 1994, pp. 124–134. DOI: 10.1109/SFCS.1994.365700.
- [4] Grover, L. K. "A Fast Quantum Mechanical Algorithm for Database Search". Proceedings of the Twenty-eighth Annual ACM Symposium on Theory of Computing. STOC '96. Philadelphia, Pennsylvania, USA: ACM, 1996, pp. 212–219. ISBN: 0-89791-785-5. URL: http://doi.acm.org/10.1145/237814.237866.
- [5] Deutsch, D. et al. Proceedings of the Royal Society of London A: Mathematical, Physical and Engineering Sciences 439.1907 (1992), pp. 553-558. ISSN: 0962-8444. DOI: 10.1098/rspa.1992.0167.
- [6] Cirac, J. I. et al. Phys. Rev. Lett. 74 (20 May 1995), pp. 4091-4094. URL: http://link.aps.org/doi/10.1103/PhysRevLett.74.4091.

[7] Monroe, C. et al. Phys. Rev. Lett. 75 (25 Dec. 1995), pp. 4714-4717. URL: http://link.aps.org/doi/10.1103/PhysRevLett.75.4714.

- [8] DiVincenzo, D. P. Fortschritte der Physik 48 (2000), pp. 771-783. URL: http://arxiv.org/abs/quant-ph/0002077.
- [9] Roos, C. F. et al. Nature 443 (2006), pp. 316-319. URL: http://dx.doi.org/10.1038/nature05101.
- [10] Harty, T. P. et al. *Phys. Rev. Lett.* 113 (22 Nov. 2014), p. 220501. URL: http://link.aps.org/doi/10.1103/PhysRevLett.113.220501.
- [11] Dehmelt, H. G. Bull. Am. Phys. Soc. 20 (1975), p. 60.
- [12] Benhelm, J. et al. *Phys. Rev. A* 77 (6 June 2008), p. 062306. URL: http://link.aps.org/doi/10.1103/PhysRevA.77.062306.
- [13] Bollinger, J. et al. Instrumentation and Measurement, IEEE Transactions on 40.2 (Apr. 1991), pp. 126–128. ISSN: 0018-9456. DOI: 10.1109/TIM.1990. 1032897.
- [14] Seidelin, S. et al. *Phys. Rev. Lett.* 96 (25 June 2006), p. 253003. URL: http://link.aps.org/doi/10.1103/PhysRevLett.96.253003.
- [15] Kielpinski, D. et al. Nature 417 (2002), pp. 709-711. URL: http://dx.doi. org/10.1038/nature00784.
- [16] Mount, E. et al. arXiv:1504.01440 [quant-ph] (2015). URL: http://arxiv.org/abs/1504.01440.
- [17] Mizrahi, J. et al. "Two Ion Entangling Gate in a Microfabricated Surface Electrode Ion Trap". In preparation. 2015.
- [18] Steane, A. Applied Physics B 64.6 (1997), pp. 623-643. ISSN: 0946-2171. URL: http://dx.doi.org/10.1007/s003400050225.
- [19] Wineland, D. J. *Physica Scripta* 2009.T137 (2009), p. 014007. URL: http://stacks.iop.org/1402-4896/2009/i=T137/a=014007.

[20] Hughes, M. D. et al. Contemporary Physics 52.6 (2011), pp. 505-529. eprint: http://dx.doi.org/10.1080/00107514.2011.601918. URL: http://dx.doi.org/10.1080/00107514.2011.601918.

- [21] Šašura, M. et al. Journal of Modern Optics 49.10 (2002), pp. 1593-1647.
  eprint: http://dx.doi.org/10.1080/09500340110115497. URL: http://dx.doi.org/10.1080/09500340110115497.
- [22] Leibfried, D. et al. Rev. Mod. Phys. 75 (1 Mar. 2003), pp. 281-324. URL: http://link.aps.org/doi/10.1103/RevModPhys.75.281.
- [23] Wineland, D. et al. *J.Res.Natl.Inst.Stand.Tech.* 103 (1998), p. 259. URL: http://tf.nist.gov/general/pdf/1275.pdf.
- [24] Major, F. G. et al. Charged Particle Traps. Springer-Verlag Berlin Heidelberg, 2005.
- [25] Werth, G. et al. *Charged Particle Traps II*. Springer-Verlag Berlin Heidelberg, 2009.
- [26] Paul, W. et al. Zeitschrift für Naturforschung A 8.7 (1953), pp. 448–450. URL: http://www.degruyter.com/view/j/zna.1953.8.issue-7/zna-1953-0710/zna-1953-0710.xml.
- [27] Paul, W. Rev. Mod. Phys. 62 (3 July 1990), pp. 531-540. URL: http://link.aps.org/doi/10.1103/RevModPhys.62.531.
- [28] Prestage, J. D. et al. Journal of Applied Physics 66.3 (1989), pp. 1013-1017.
  URL: http://scitation.aip.org/content/aip/journal/jap/66/3/10.
  1063/1.343486.
- [29] Raizen, M. G. et al. *Phys. Rev. A* 45 (9 May 1992), pp. 6493-6501. URL: http://link.aps.org/doi/10.1103/PhysRevA.45.6493.
- [30] Furukawa, T. et al. Japanese Journal of Applied Physics 44.10R (2005), p. 7619. URL: http://stacks.iop.org/1347-4065/44/i=10R/a=7619.

[31] Leibrandt, D. R. et al. *Phys. Rev. Lett.* 103 (10 Aug. 2009), p. 103001. URL: http://link.aps.org/doi/10.1103/PhysRevLett.103.103001.

- [32] Goeders, J. E. Doctoral Dissertation. Georgia Institute of Technology, 2013. URL: http://hdl.handle.net/1853/49082.
- [33] Drewsen, M. et al. *Phys. Rev. A* 62 (4 Sept. 2000), p. 045401. URL: http://link.aps.org/doi/10.1103/PhysRevA.62.045401.
- [34] Ibaraki, Y. et al. Applied Physics B 105.2 (2011), pp. 219–223. ISSN: 0946-2171. URL: http://dx.doi.org/10.1007/s00340-011-4463-x.
- [35] Noguchi, A. et al. *Nature Communications* 5.4868 (2014). DOI: http://dx.doi.org/10.1038/ncomms4868.
- [36] Schmidt-Kaler, F. et al. *Nature* 422 (2003), 408–411.
- [37] Riebe, M. et al. *Phys. Rev. Lett.* 97 (22 Dec. 2006), p. 220407. URL: http://link.aps.org/doi/10.1103/PhysRevLett.97.220407.
- [38] Benhelm, J. et al. *Nature Physics* 4 (2008), pp. 463-466. URL: http://dx.doi.org/10.1038/nphys961.
- [39] Kirchmair, G. et al. New Journal of Physics 11.2 (2009), p. 023002. URL: http://stacks.iop.org/1367-2630/11/i=2/a=023002.
- [40] Schmidt-Kaler, F. et al. Journal of Modern Optics 47.14-15 (2000), pp. 2573— 2582. eprint: http://www.tandfonline.com/doi/pdf/10.1080/09500340008232182. URL: http://www.tandfonline.com/doi/abs/10.1080/09500340008232182.
- [41] Monz, T. et al. *Phys. Rev. Lett.* 106 (13 Mar. 2011), p. 130506. URL: http://link.aps.org/doi/10.1103/PhysRevLett.106.130506.
- [42] Leibfried, D. et al. Nature 422 (2003), pp. 412-415. URL: http://dx.doi. org/10.1038/nature01492.
- [43] Tan, T. R. et al. *Phys. Rev. Lett.* 110 (26 June 2013), p. 263002. URL: http://link.aps.org/doi/10.1103/PhysRevLett.110.263002.

- [44] Rosenband, T. et al. *Science* 319 (2008), p. 1808.
- [45] Hucul, D. et al. *Nature Physics* 11 (1 Jan. 2015), pp. 37-42. URL: http://dx.doi.org/10.1038/nphys3150.
- [46] Madsen, M. et al. Applied Physics B 78.5 (2004), pp. 639-651. ISSN: 0946-2171. URL: http://dx.doi.org/10.1007/s00340-004-1414-9.
- [47] Stick, D. et al. *Nature Physics* 2 (2006), pp. 36-39. URL: http://dx.doi.org/10.1038/nphys171.
- [48] Chiaverini, J. et al. Quantum Info. Comput. 5.6 (Sept. 2005), pp. 419-439.
  ISSN: 1533-7146. URL: http://dl.acm.org/citation.cfm?id=2011670.
  2011671.
- [49] Dehmelt, H. "Radiofrequency Spectroscopy of Stored Ions I: Storage\*". Ed. by Bates, D. et al. Vol. 3. Advances in Atomic and Molecular Physics. Academic Press, 1968, pp. 53–72. URL: http://www.sciencedirect.com/science/article/pii/S0065219908601700.
- [50] Wineland, D. et al. Bull. Am. Phys. Soc. 20 (1975), p. 637.
- [51] Eschner, J. et al. J. Opt. Soc. Am. B 20.5 (May 2003), pp. 1003-1015. URL: http://josab.osa.org/abstract.cfm?URI=josab-20-5-1003.
- [52] Metcalf, H. J. et al. Laser Cooling and Trapping. Springer New York, 1999.
- [53] Wineland, D. J. et al. Phys. Rev. A 20 (4 Oct. 1979), pp. 1521-1540. URL: http://link.aps.org/doi/10.1103/PhysRevA.20.1521.
- [54] Stenholm, S. Rev. Mod. Phys. 58 (3 July 1986), pp. 699-739. URL: http://link.aps.org/doi/10.1103/RevModPhys.58.699.
- [55] Neuhauser, W. et al. *Phys. Rev. Lett.* 41 (4 July 1978), pp. 233-236. URL: http://link.aps.org/doi/10.1103/PhysRevLett.41.233.
- [56] Wineland, D. J. et al. Phys. Rev. Lett. 40 (25 June 1978), pp. 1639-1642.
  URL: http://link.aps.org/doi/10.1103/PhysRevLett.40.1639.

[57] Diedrich, F. et al. *Phys. Rev. Lett.* 62 (4 Jan. 1989), pp. 403-406. URL: http://link.aps.org/doi/10.1103/PhysRevLett.62.403.

- [58] Monroe, C. et al. Phys. Rev. Lett. 75 (22 Nov. 1995), pp. 4011-4014. URL: http://link.aps.org/doi/10.1103/PhysRevLett.75.4011.
- [59] Turchette, Q. A. et al. *Phys. Rev. A* 61 (6 May 2000), p. 063418. URL: http://link.aps.org/doi/10.1103/PhysRevA.61.063418.
- [60] Poulsen, G. Doctoral Dissertation. University of Aarhus, Denmark, 2011. URL: http://phys.au.dk/fileadmin/site\_files/forskning/iontrap/pdfs/ PhD\_Poulsen\_2012.pdf.
- [61] Major, F. G. et al. Phys. Rev. 170 (1 June 1968), pp. 91-107. URL: http://link.aps.org/doi/10.1103/PhysRev.170.91.
- [62] Gaboriaud, M. et al. International Journal of Mass Spectrometry and Ion Physics 41.1-2 (1981), pp. 109-123. ISSN: 0020-7381. URL: http://www.sciencedirect.com/science/article/pii/002073818185022X.
- [63] Madej, A. A. et al. Phys. Rev. A 41 (5 Mar. 1990), pp. 2621-2630. URL: http://link.aps.org/doi/10.1103/PhysRevA.41.2621.
- [64] Kreuter, A. Doctoral Dissertation. Innsbruck, Austria: Leopold Franzens Universitat Innsbruck, 2004. URL: http://www.quantumoptics.at/images/publications/dissertation/kreuter\_diss.pdf.
- [65] Manning, T. A. Doctoral Dissertation. College Park, MD, USA: University of Maryland, 2014. URL: http://iontrap.umd.edu/wp-content/uploads/2014/03/ManningThesis.pdf.
- [66] Berkeland, D. J. et al. Journal of Applied Physics 83.10 (1998), pp. 5025-5033. URL: http://scitation.aip.org/content/aip/journal/jap/83/10/10.1063/1.367318.
- [67] Tanaka, U. et al. Applied Physics B 107.4 (2012), pp. 907–912. ISSN: 0946-2171. URL: http://dx.doi.org/10.1007/s00340-011-4762-2.

[68] Britton, J. et al. arXiv:quant-ph/0605170v1 (2006). URL: http://arxiv.org/abs/quant-ph/0605170.

- [69] Stick, D. et al. ArXiv e-prints (Aug. 2010). arXiv: 1008.0990 [physics.ins-det].
- [70] Allcock, D. T. C. et al. New Journal of Physics 12.5 (2010), p. 053026. URL: http://stacks.iop.org/1367-2630/12/i=5/a=053026.
- [71] Daniilidis, N. et al. New Journal of Physics 13.1 (2011), p. 013032. URL: http://stacks.iop.org/1367-2630/13/i=1/a=013032.
- [72] Amini, J. M. et al. New Journal of Physics 12.3 (2010), p. 033031. URL: http://stacks.iop.org/1367-2630/12/i=3/a=033031.
- [73] Doret, S. C. et al. New Journal of Physics 14.7 (2012), p. 073012. URL: http://stacks.iop.org/1367-2630/14/i=7/a=073012.
- [74] Mount, E. et al. New Journal of Physics 15.9 (2013), p. 093018. URL: http://stacks.iop.org/1367-2630/15/i=9/a=093018.
- [75] Moehring, D. L. et al. New Journal of Physics 13.7 (2011), p. 075018. URL: http://stacks.iop.org/1367-2630/13/i=7/a=075018.
- [76] Tabakov, B. et al. arXiv:1501.06554 [quant-ph] (Jan. 2015). URL: http://arxiv.org/abs/1501.06554.
- [77] Moehring, D. L. et al. *Ion-Photon Quantum Interface: Entanglement Engineering*. Sandia Report SAND2012-6138. P.O. Box 5800, Albuquerque, NM., 87185: Sandia National Laboratories, Sept. 2012. URL: http://prod.sandia.gov/techlib/access-control.cgi/2012/126138.pdf.
- [78] Clark, C. R. et al. *Phys. Rev. Applied* 1 (2 Mar. 2014), p. 024004. URL: http://link.aps.org/doi/10.1103/PhysRevApplied.1.024004.
- [79] O'Hanlon, J. F. A User's Guide to Vacuum Technology. Wiley, 2003.
- [80] Zverev, A. et al. Component Parts, IRE Transactions on 8.3 (Sept. 1961), pp. 99–110. ISSN: 0096-2422. DOI: 10.1109/TCP.1961.1136604.

[81] O'Meara, T. et al. Component Parts, IRE Transactions on 9.4 (Dec. 1962), pp. 213–214. ISSN: 0096-2422. DOI: 10.1109/TCP.1962.1136766.

- [82] Spencer, N. Electronic and Radio Engineers, Journal of the Institution of 57.5 (Sept. 1987), pp. 213–220. ISSN: 0267-1689. DOI: 10.1049/jiere.1987.0072.
- [83] Gandolfi, D. Final Thesis. Universita degli Studi di Trento and Universitat Innsbruck, 2011. URL: http://www.quantumoptics.at/images/publications/diploma/diplom\_gandolfi.pdf.
- [84] Siverns, J. et al. Applied Physics B 107.4 (2012), pp. 921–934. ISSN: 0946-2171.
  URL: http://dx.doi.org/10.1007/s00340-011-4837-0.
- [85] Kyaw, P. A. Honors Thesis. Amherst College, 2014. URL: https://www.amherst.edu/system/files/Phyo%20Kyaw.pdf.
- [86] Pearson, C. E. et al. *Phys. Rev. A* 73 (3 Mar. 2006), p. 032307. URL: http://link.aps.org/doi/10.1103/PhysRevA.73.032307.
- [87] Brown, K. R. et al. *Phys. Rev. A* 75 (1 Jan. 2007), p. 015401. URL: http://link.aps.org/doi/10.1103/PhysRevA.75.015401.
- [88] Laeter John R., de et al. Pure and Applied Chemistry (2009).
- [89] Ramm, M. et al. *Phys. Rev. Lett.* 111 (2 July 2013), p. 023004. URL: http://link.aps.org/doi/10.1103/PhysRevLett.111.023004.
- [90] Kreuter, A. et al. *Phys. Rev. A* 71 (3 Mar. 2005), p. 032504. URL: http://link.aps.org/doi/10.1103/PhysRevA.71.032504.
- [91] Berkeland, D. J. et al. *Phys. Rev. A* 65 (3 Feb. 2002), p. 033413. URL: http://link.aps.org/doi/10.1103/PhysRevA.65.033413.
- [92] Lisowski, C. et al. Applied Physics B 81.1 (2005), pp. 5–12. ISSN: 0946-2171. URL: http://dx.doi.org/10.1007/s00340-005-1867-5.

[93] Roos, C. F. Doctoral Dissertation. Innsbruck, Austria: Leopold Franzens Universitat Innsbruck, 2000. URL: http://www.quantumoptics.at/images/publications/dissertation/roos\_diss.pdf.

- [94] Gulde, S. et al. Applied Physics B 73.8 (2001), pp. 861-863. ISSN: 0946-2171.URL: http://dx.doi.org/10.1007/s003400100749.
- [95] Kjaergaard, N. et al. Applied Physics B 71.2 (2000), pp. 207–210. ISSN: 0946-2171. URL: http://dx.doi.org/10.1007/s003400000296.
- [96] Armstrong, J. A. et al. *Phys. Rev. A* 15 (1 Jan. 1977), pp. 180-196. URL: http://link.aps.org/doi/10.1103/PhysRevA.15.180.
- [97] Wendt, K. et al. Fresenius' Journal of Analytical Chemistry 359.4-5 (1997),
   pp. 361–363. ISSN: 0937-0633. URL: http://dx.doi.org/10.1007/s002160050587.
- [98] Schuck, C. et al. Applied Physics B 100.4 (2010), pp. 765-771. ISSN: 0946-2171. URL: http://dx.doi.org/10.1007/s00340-010-4086-7.
- [99] Kim, K. et al. Nature 465.7298 (June 3, 2010), pp. 590-593. ISSN: 0028-0836.
  URL: http://dx.doi.org/10.1038/nature09071.
- [100] Horstmann, B. et al. *Phys. Rev. Lett.* 104 (25 June 2010), p. 250403. URL: http://link.aps.org/doi/10.1103/PhysRevLett.104.250403.
- [101] Fishman, S. et al. *Phys. Rev. B* 77 (6 Feb. 2008), p. 064111. URL: http://link.aps.org/doi/10.1103/PhysRevB.77.064111.
- [102] Morigi, G. et al. Journal of Physics B: Atomic, Molecular and Optical Physics 39.10 (2006), S221. URL: http://stacks.iop.org/0953-4075/39/i=10/a=S21.
- [103] Shimshoni, E. et al. *Phys. Rev. Lett.* 106 (1 Jan. 2011), p. 010401. URL: http://link.aps.org/doi/10.1103/PhysRevLett.106.010401.
- [104] Shimshoni, E. et al. *Phys. Rev. A* 83 (3 Mar. 2011), p. 032308. URL: http://link.aps.org/doi/10.1103/PhysRevA.83.032308.

[105] Campo, A. del et al. *Phys. Rev. Lett.* 105 (7 Aug. 2010), p. 075701. URL: http://link.aps.org/doi/10.1103/PhysRevLett.105.075701.

- [106] Landa, H. et al. *Phys. Rev. Lett.* 113 (5 July 2014), p. 053001. URL: http://link.aps.org/doi/10.1103/PhysRevLett.113.053001.
- [107] Landa, H. et al. *Phys. Rev. Lett.* 104 (4 Jan. 2010), p. 043004. URL: http://link.aps.org/doi/10.1103/PhysRevLett.104.043004.
- [108] Li, T. et al. *Phys. Rev. Lett.* 109 (16 Oct. 2012), p. 163001. URL: http://link.aps.org/doi/10.1103/PhysRevLett.109.163001.
- [109] Kim, T. H. et al. *Phys. Rev. A* 82 (4 Oct. 2010), p. 043412. URL: http://link.aps.org/doi/10.1103/PhysRevA.82.043412.
- [110] Champenois, C. et al. *Phys. Rev. A* 81 (4 Apr. 2010), p. 043410. URL: http://link.aps.org/doi/10.1103/PhysRevA.81.043410.
- [111] Marciante, M. et al. Applied Physics B 107.4 (2012), pp. 1117–1123. ISSN: 0946-2171. URL: http://dx.doi.org/10.1007/s00340-012-4883-2.
- [112] Cartarius, F. et al. *Phys. Rev. A* 87 (1 Jan. 2013), p. 013425. URL: http://link.aps.org/doi/10.1103/PhysRevA.87.013425.
- [113] Clark, R. Applied Physics B 113.2 (2013), pp. 171–178. ISSN: 0946-2171. URL: http://dx.doi.org/10.1007/s00340-013-5451-0.
- [114] Birkl, G. et al. *Nature* 357.6376 (1992), pp. 310-313. URL: http://dx.doi.org/10.1038/357310a0.
- [115] Bliek, F. et al. *Hyperfine Interactions* 99.1 (1996), pp. 193–200. ISSN: 0304-3843. URL: http://dx.doi.org/10.1007/BF02274922.
- [116] Church, D. A. Journal of Applied Physics 40.8 (1969), pp. 3127-3134. URL: http://scitation.aip.org/content/aip/journal/jap/40/8/10.1063/ 1.1658153.

[117] Schuch, R. *Physica Scripta* 1995.T59 (1995), p. 77. URL: http://stacks.iop.org/1402-4896/1995/i=T59/a=010.

- [118] Schätz, T. et al. *Hyperfine Interactions* 115.1-4 (1998), pp. 29–36. ISSN: 0304-3843. URL: http://dx.doi.org/10.1023/A:1012624000341.
- [119] Schätz, T. et al. *Nature* 412.6848 (2001), pp. 717–720. ISSN: 0028-0836. URL: http://dx.doi.org/10.1038/35089045.
- [120] Schramm, U. et al. *Phys. Rev. E* 66 (3 Sept. 2002), p. 036501. URL: http://link.aps.org/doi/10.1103/PhysRevE.66.036501.
- [121] Schramm, U. et al. *Phys. Rev. Lett.* 87 (18 Oct. 2001), p. 184801. URL: http://link.aps.org/doi/10.1103/PhysRevLett.87.184801.
- [122] Ji, Q. et al. Journal of the American Society for Mass Spectrometry 7.10 (1996), pp. 1009-1017. ISSN: 1044-0305. URL: http://dx.doi.org/10.1016/ 1044-0305(96)00044-X.
- [123] Lammert, S. A. et al. International Journal of Mass Spectrometry 212.1-3 (2001), pp. 25-40. ISSN: 1387-3806. URL: http://www.sciencedirect.com/science/article/pii/S1387380601005073.
- [124] Lammert, S. A. et al. Journal of the American Society for Mass Spectrometry 17.7 (2006), pp. 916-922. ISSN: 1044-0305. URL: http://www.sciencedirect.com/science/article/pii/S1044030506001255.
- [125] Waki, I. et al. *Phys. Rev. Lett.* 68 (13 Mar. 1992), pp. 2007–2010. URL: http://link.aps.org/doi/10.1103/PhysRevLett.68.2007.
- [126] Kajita, M. et al. Applied Physics B 58.4 (1994), pp. 295–301. ISSN: 0946-2171.
  URL: http://dx.doi.org/10.1007/BF01082624.
- [127] Feng, X. et al. *Hyperfine Interactions* 100.1 (1996), pp. 91–101. ISSN: 0304-3843. URL: http://dx.doi.org/10.1007/BF02059935.

[128] Ramirez, E. M. et al. Nuclear Instruments and Methods in Physics Research Section B: Beam Interactions with Materials and Atoms 266.19–20 (2008). Proceedings of the {XVth} International Conference on Electromagnetic Isotope Separators and Techniques Related to their Applications, pp. 4460–4465. ISSN: 0168-583X. URL: http://www.sciencedirect.com/science/article/pii/S0168583X08007568.

- [129] Dubin, D. H. E. *Phys. Rev. E* 55 (4 Apr. 1997), pp. 4017-4028. URL: http://link.aps.org/doi/10.1103/PhysRevE.55.4017.
- [130] Narayanan, S. et al. Journal of Applied Physics 110.11, 114909 (2011), pages. URL: http://scitation.aip.org/content/aip/journal/jap/110/11/10. 1063/1.3665647.
- [131] Lin, G.-D. et al. *EPL* (Europhysics Letters) 86.6 (2009), p. 60004. URL: http://stacks.iop.org/0295-5075/86/i=6/a=60004.
- [132] Optical Lattice Emulator Program. http://www.quantum.gatech.edu/ole.shtml. Accessed: 2015-04-21.
- [133] Harlander, M. et al. New Journal of Physics 12.9 (2010), p. 093035. URL: http://stacks.iop.org/1367-2630/12/i=9/a=093035.
- [134] Jackson, J. D. Classical electrodynamics. 3rd ed. New York: Wiley, 1998.
- [135] Oliveira, M. H. et al. European Journal of Physics 22.1 (2001), p. 31. URL: http://stacks.iop.org/0143-0807/22/i=1/a=304.
- [136] House, M. G. *Phys. Rev. A* 78 (3 Sept. 2008), p. 033402. URL: http://link.aps.org/doi/10.1103/PhysRevA.78.033402.
- [137] Wesenberg, J. H. *Phys. Rev. A* 78 (6 Dec. 2008), p. 063410. URL: http://link.aps.org/doi/10.1103/PhysRevA.78.063410.
- [138] Schmied, R. et al. *Phys. Rev. Lett.* 102 (23 June 2009), p. 233002. URL: http://link.aps.org/doi/10.1103/PhysRevLett.102.233002.

[139] Schmied, R. New Journal of Physics 12.2 (2010), p. 023038. URL: http://stacks.iop.org/1367-2630/12/i=2/a=023038.

- [140] Clemson Vehicular Electronics Laboratory Electromagnetic Modeling. http://www.cvel.clemson.edu/modeling/. Accessed: 2015-04-13.
- [141] Singer, K. et al. Rev. Mod. Phys. 82 (3 Sept. 2010), pp. 2609-2632. URL: http://link.aps.org/doi/10.1103/RevModPhys.82.2609.
- [142] Singer, K. Essential Numerical Tools Packages. http://www.uni-ulm.de/~ksinger/ent/. Accessed: 2015-04-13.
- [143] Graham, R. D. et al. AIP Advances 4.5, 057124 (2014), pages. URL: http://scitation.aip.org/content/aip/journal/adva/4/5/10.1063/1. 4879817.
- [144] Akerman, N. et al. *Phys. Rev. A* 82 (6 Dec. 2010), p. 061402. URL: http://link.aps.org/doi/10.1103/PhysRevA.82.061402.
- [145] Haltli, R. A. Masters Thesis. The University of New Mexico, 2015.
- [146] Brownnutt, M. et al. arXiv:1409.6572 [quant-ph] (Sept. 2014). URL: http://arxiv.org/abs/1409.6572.
- [147] Deslauriers, L. et al. Phys. Rev. Lett. 97 (10 Sept. 2006), p. 103007. URL: http://link.aps.org/doi/10.1103/PhysRevLett.97.103007.
- [148] Allcock, D. T. C. et al. New Journal of Physics 13.12 (2011), p. 123023. URL: http://stacks.iop.org/1367-2630/13/i=12/a=123023.
- [149] Hite, D. A. et al. *Phys. Rev. Lett.* 109 (10 Sept. 2012), p. 103001. URL: http://link.aps.org/doi/10.1103/PhysRevLett.109.103001.
- [150] McConnell, R. et al. arXiv:1505.03844 [physics.atom-ph] (May 2015). URL: http://arxiv.org/abs/1505.03844.

[151] Wang, S. X. et al. Journal of Applied Physics 110.10, 104901 (2011), pages. URL: http://scitation.aip.org/content/aip/journal/jap/110/10. 1063/1.3662118.

- [152] Lieberman, M. A. et al. *Principles of Plasma Discharges and Materials Processing*. Wiley, 2005.
- [153] Shu, G. et al. *Phys. Rev. A* 89 (6 June 2014), p. 062308. URL: http://link.aps.org/doi/10.1103/PhysRevA.89.062308.
- [154] Hopwood, J. Plasma Sources Science and Technology 1.2 (1992), p. 109. URL: http://stacks.iop.org/0963-0252/1/i=2/a=006.
- [155] Alnis, J. et al. Phys. Rev. A 77 (5 May 2008), p. 053809. URL: http://link. aps.org/doi/10.1103/PhysRevA.77.053809.
- [156] Toyoda, K. et al. Japanese Journal of Applied Physics 42.3R (2003), p. 1268. URL: http://stacks.iop.org/1347-4065/42/i=3R/a=1268.
- [157] Wheeler, D. A. Counting Source Lines of Code (SLOC). http://www.dwheeler.com/sloc/. Accessed: 2015-06-12.
- [158] Böhnert, M. et al. Proceedings of the 14th International Workshop on RF Superconductivity (2009), p. 883. URL: http://accelconf.web.cern.ch/AccelConf/srf2009/papers/thppo104.pdf.